ION CYCLOTRON INSTABILITIES DRIVEN BY THE NEARLY PERPENDICULAR NEUTRAL BEAM INJECTION IN THE WENDELSTEIN VII-A STELLARATOR

H. Maaßberg and M.A. Hellberg

IPP 2/282 August 1986

MAX-PLANCK-INSTITUT FÜR PLASMAPHYSIK

8046 GARCHING BEI MÜNCHEN

MAX-PLANCK-INSTITUT FÜR PLASMAPHYSIK

GARCHING BEI MÜNCHEN

ION CYCLOTRON INSTABILITIES DRIVEN BY THE NEARLY PERPENDICULAR NEUTRAL BEAM INJECTION IN THE WENDELSTEIN VII-A STELLARATOR

H. Maaßberg and M.A. Hellberg

IPP 2/282 August 1986

Die nachstehende Arbeit wurde im Rahmen des Vertrages zwischen dem Max-Planck-Institut für Plasmaphysik und der Europäischen Atomgemeinschaft über die Zusammenarbeit auf dem Gebiete der Plasmaphysik durchgeführt.

ION CYCLOTRON INSTABILITIES DRIVEN BY THE NEARLY PERPENDICULAR NEUTRAL BEAM INJECTION IN THE WENDELSTEIN VII-A STELLARATOR

H. Maaßberg and M.A. Hellberg*

Max-Planck-Institut für Plasmaphysik
Association EURATOM-IPP
Garching bei München
Federal Republic of Germany

* Permanent address:
Plasma Physics Research Institute
Department of Physics
University of Natal, Durban
South Africa

Abstract

The problem of ion cyclotron instabilities driven by the high power neutral beam injection is investigated for the conditions of the W VII-A stellarator by means of linear stability analysis. On the basis of only collisional (*classical*) slowing down, beam ion distribution functions are calculated by means of Monte Carlo simulation. In this report, various cases are considered: transient beam ion distributions (i) immediately after switch on the neutral beam injection and (ii) after half of an average slowing down time; stationary beam ion distributions (iii) for confinement properties strongly improved by radial electric fields, transport and fast orbit losses are neglected for these situations, and (iv) for worse confinement properties for which the average beam ion confinement time is of the order of the average slowing down time. Furthermore, the distribution functions of the ions originating from the neutral beam injection are estimated for the early phase of the discharges with low temperatures and for the later phase with maximum ion temperatures.

The contribution of the beam ion distributions to the dielectric tensor is estimated by means of a $\underline{v}$-space convolution formalism which allows the accurate treatment of arbitrary distribution functions. Then, the dispersion relation with all dielectric tensor elements included is solved numerically by means of a Cauchy rootfinder routine which was developed to make sure to find all modes of interest. The analysis is carried out for the various ranges of ion cyclotron harmonics also above the lower hybrid frequency.

We found the ion Bernstein mode being unstable with sufficiently small growth distances even for low ion cyclotron harmonics in case of the transient beam ion distributions after switch on the injection. The stationary distributions can drive the ion Bernstein mode unstable only for the higher harmonics, strong loss cone effects significantly increase the instability. Above the lower hybrid frequency, all beam ion distributions investigated lead to very strong lower hybrid instability. However, sharp resonances in $k_\perp$ appear which are related to those domains in $\underline{v}$-space with $\partial f_b / \partial v_\perp > 0$; only for these values of $k_\perp$, instability was found. At high ion cyclotron harmonis, the instabilities will smooth the beam ion distributions only close to to the injection energies. Then, the average slowing down is expected to be mainly determined by collisional interactions in case of the stationary distribution functions. For low ion cyclotron harmonics, however, the transient distribution functions will be strongly affected by this *anomalous* slowing down, but will remain unstable. The ion Bernstein modes at low harmonics are mainly damped by the thermal ions, consequently, preferential ion heating must be expected immediately after switch on the injection.

Finally, results of experiments are discussed which had been carried out to clarify the slowing down mechanism of the neutral beam injection in W VII-A. These results lead to the conclusion of mainly collisional slowing down for stationary conditions as well as after switch off the injection. However, preferential ion heating and increased low harmonic ion cyclotron emission were measured shortly after switch on the neutral beam injection.

Contents

I. Introduction

For high power neutral beam injection nearly perpendicular to the magnetic field, it is important to understand the heating mechanism which may be dominated by micro-instabilities in the ion cyclotron frequency range driven by the high energetic ion component. If the slowing down of the fast ions originating from the neutral beam is dominated by Coulomb interactions with the thermal plasma components (collisional or, as some times called, *classical* slowing down), a relative strong anisotropy of the ion distribution functions must be expected due to the long slowing down times. On the other hand, the slowing down distribution of the beam particles may have domains with positive gradients in $\underline{v}$-space which can drive micro-instabilities. These instabilities sufficiently growthed may be related to much faster slowing down of the fast ions which represent free energy for driving the instabilities and, consequently, leading to strong deformation of the beam particle distribution function (quasi-linear effects), this may saturate the unstable modes. As the heating efficiency of both thermal ions and electrons depends on the slowing down mechanism, some theoretical as well as experimental effort has been done to clarify the question of micro-instabilities driven by the neutral beam injection.

In the beginning phase of plasma heating by high power neutral beams, Cordey and Houghton /1/ expected the appearance of micro-instabilities for the stationary phase as well as after switch in the neutral beam injection; they proposed that the injection should be as parallel to the magnetic field as feasible. Most of the neutral beam heated experiments used nearly parallel injection, however, the main reasons for doing this were the signifficantly reduced shine through of fast neutrals and the better confinement properties of fast ions with velocities mainly parallel to the magnetic field. With the increased plasma radius, the perpendicular injection is more favourable in order to deposite the beam power closer to the plasma center. Furthermore, also for mainly parallel neutral beam injection, micro-instabilities may appear: Mai and Horton /2/ have shown that ion cyclotron modes, namely at the ion Landau resonance, $\omega \simeq k_{\|} v_{\|}$, and at the backward ion cyclotron resonance, $\omega + \omega_{cb} \simeq k_{\|} v_{\|}$, become unstable at sufficiently high power injection; the fundamental ion cyclotron resonance, $\omega - \omega_{cb} \simeq k_{\|} v_{\|}$, however, was found to be more stable for parallel injection. Most of the theoretical investigations of beam plasma systems have concentrated on cases where the beam is nearly parallel to the magnetic field.

The neutral beam injection nearly perpendicular to the magnetic field and the slowing down mechanism had been investigated experimentally in the TFR tokamak /3/. Both charge exchange fluxes of high energetic neutrals and neutron fluxes for D^0 injection into a D^+ target plasma had been measured and compared with Monte Carlo simulations based on the assumption of only collisional slowing down of the fast beam ions, satisfactory aggreement was found. However, the phase immediately after switch on the high power neutral beam injection was disregarded; thus, the conclusion of classical slowing down is restricted to the stationary phase as well as after switch off the injection. Sbitnikova and Chudoleev /4/ reported that at the L-2 stellarator anomalous fast slowing down of ions originating from a diagnostic neutral beam, much faster than it could be explained by

means of collisional interactions, was observed. However, no correlation to ion cyclotron activities were reported.

In the beginning of high power neutral beam injection nearly perpendicular to the magnetic field (84^o) at the W VII-A stellarator with a plasma radius of only less than 10 cm, the slowing down mechanism of the fast ions was an important point for understanding both the heating efficiencies and the power balances for ions and electrons. For the typical conditions of strongly neutral beam heated discharges in W VII-A, Monte Carlo simulations with the assumption of only collisional slowing down of the fast ions indicate that most of the heating power is transfered to the electrons. Furthermore, without radial electric fields improving the confinement of the high energetic ions, the gloabal heating efficiency is found to be very low and fast orbit losses to play a major role. However, for these discharges the ion temperature significantly exceeds the electron temperature. From these findings the question of the slowing down mechanism eventually related to preferential ion heating arised /5/. This question was the starting point for the stability analysis of the high power neutral beam injection under the specific conditions of the W VII-A stellarator; we reported preliminary results in /6/.

In the recent years /7, 8/, the heating efficiency as well as the ion energy balance could be clarified for the W VII-A conditions. The high power neutral beam injection is connected with fast orbit losses leading to a strong radial electric field which significantly improves the confinement of both the fast ions originating from the injection as well as the thermal ions. The poloidal plasma rotation ($\underline{E} \times \underline{B}$-drift) deduced from the Doppler shift measurements of impurity lines was found to be up to $4 \cdot 10^4\ m/s$ leading to electric fields up to $-500\ V/cm$. Consequently, the global heating efficiency is significantly improved and the thermal ion heat conduction is strongly reduced by these electric fields /9/. Then, the ion as well as the electron energy balance could be understood even for $T_i > T_e$ by means of collisional slowing down. Nevertheless, special experiments were carried out in W VII-A in order to investigate the heating mechanism of the neutral beam injection. From highly time resolved measurements of the charge exchange flux as well as the neutron flux in case of D^0 injection into a D^+ target plasma /10/, the slowing down mechanism was proved to be collisional after switch off one or all neutral beam lines; we describe shortly these experiments in Chapter VII.

The problem of an ion beam allmost perpendicular to the magnetic field was theoretically investigated by means of simplified models, the development of low harmonic ion Bernstein instabilities /11/ as well as of lower hybrid instabilities /12/ has been predicted. These modes may be driven unstable by the domains of the beam ion distribution function with $\partial f_b / \partial v_\perp > 0$ and propagate nearly in the perpendicular direction with respect to the magnetic field lines. Non-linear saturation effects of unstable modes as well as quasi-linear deformation of the driving beam particle distribution has been investigated by Lee and Birdsall /13/; these effects were found to occur on a much faster time scale (of about few ion cyclotron periods) than collisional slowing down. However, these investigations are based on beam models at high energy, but with low temperature.

The situation for the stationary phase of high power neutral beam injection almost perpendicular to the magnetic field is quite different as the beam ion distribution may be determined by the collisional slowing down spectrum which becomes broader in $v_{||}$ due to ion pitch angle scattering and is mainly decreasing for $v_{\perp}$ increasing; only close to the injection energies, peaks in f_b driving instabilities may be expected. As the unstable modes may sensitively depend on the shape of the beam ion distribution function, simplified analytical models should only be used for special investigations (see e.g. /14/). A quasi-linear theory of ion cyclotron instabilities for two energy component systems was developed by Berk et al. /15/ and used by Brecht et al. /16/ to investigate the neutral beam injection for the conditions of the TFTR and TFR tokamaks. Basis of this quasi-linear theory is the assumption, that the behaviour of the unstable modes is nearly unaffected by the beam distribution function, then, the influence of the fast beam particles on the dispersion relation is neglected. However, this assumption may be violated for high beam densities as we must expect for collisional slowing down in case of high power injection the W VII-A stellarator. Then, the dispersion relation for ion cyclotron modes may be strongly affected by the form of the beam particle distribution function. In our calculations, we found both plasma modes being strongly modified by the beam ion distributions as well as modes only existing due to the beam ions for higher densities.

In this report, we carry out the linear stability analysis based on the solution of the dispersion relation containing the thermal plasma and the beam ion contributions for the various ranges of ion cyclotron harmonics. We are only interested to analyze the stability of various beam ion distribution functions and find all unstable modes, the estimation of quasi-linear effects deformating the beam ion distribution is not the aim of this report. We assume the magnetic field being constant, but restrict our analysis to sufficient large $\underline{k}$-values corresponding to the requirement of very small wave lengths compared to the typical size of magnetic field and plasma variations. Consequently, this requirement prohibits the simplifying approach $k_{||} \rightarrow 0$. Furthermore, we solve numerically the dispersion relation with all dielectric tensor elements included. However, we take only the major contributions of the beam ions to the dielectric tensor into account. This proceeding is tested by means of analytical beam models for which we calculated nearly all dielectric tensor elements.

We calculated the beam ion distribution functions for the injection conditions of the W VII-A stellarator by means of Monte Carlo simulation based on the assumption of only collisional interaction with both the thermal electrons and ions (described in Appendix B). This linearisation in the Fokker-Planck collision term is justified for the beam densities found to be less than 20% (see Ref. /17/). However, we included both the energy as well as the pitch angle diffusion in the Monte Carlo simulation. So, we expect the beam ion distributions used to be fairly accurate for the W VII-A injection conditions if the slowing down mechanism is determined by Coulomb scattering. We calculated the beam ion distribution functions for different conditions described in Chapter III: in the transient phase immediately after switch on the neutral beam injection, for stationary conditions with both very good confinement as well as for worse confinement of the fast ions. In case of the good confinement due to strong radial electric fields, we neglect the fast ion losses.

The worse confinement properties are modeled by the loss of fast ions corresponding to the ∇B-drift within a small loss cone, we estimated these cases for the fast ion confinement time being of the order of the average slowing down time; these very strong loss orbit effects have significant influence on the shape of the beam ion distribution functions, especially on those domains which may drive the instabilities. Furthermore, we estimated the beam ion distributions for the early phase of W VII-A discharges with low plasma temperature as well as for the later phase with the high ion temperature.

We estimate the beam ion contribution to the dielectric tensor elements by means of a convolution formalism (described in Appendix A) based on a δ-δ distribution function for which the contributions to the dielectric tensor are estimated analytically; this is slightly different to the procedure proposed by Callen /18/. The $\underline{v}$-space convolution is carried out numerically where we handle the resonant $v_{\|}$ integrations accurately as a complex valued Hilbert integral transform to get the dielectric tensor full analytic in the complex ω-plane; we assume $\underline{k}$ being real. The numerical procdure was tested using a δ-*Maxwellian* distribution function for which we estimated the dielectric tensor elements analytically (see Appendix E). Within the numerical accuracy, the convolution formalism applied to the δ-*Maxwellian* distribution function given numerically leads to the same results as the analytical calculations. As the dispersion relation in the full form we use (see Chapter II), has an infinite number of roots, we developed a numerical Cauchy rootfinder routine to find only the unstable or weakly damped modes. This Cauchy rootfinder, described in Appendix G, calculates all roots of a complex function within a specified domain also in case of strong derivatives the complex function where gradient methods fail.

We analyze the beam ion distribution functions given in Chapter III for various ranges of ion cyclotron harmonics (Chapters IV to VI). The ion cyclotron instabilities found, especially the ion Bernstein mode instability and the lower hybrid instability at very high harmonics, will lead to quasi-linear deformations of the beam ion distribution functions, this is discussed in Chapter VII for the beam ion distributions investigated. Then, we draw theoretical conclusions and compare our findings with the results of experiments which were done in order to clarifiy the slowing down mechanism of the nearly perpendicular high power neutral beam injection in the W VII-A stellarator.

II. Basic Equations

As we are interested in the stability analysis of distribution functions of the slowed down ion of the neutral beam injection, which are to be treated most accurate in velocity space, we strongly simplify the configuration space dependence. We assume the magnetic field to be homogeneous and neglect curvature and helical ripple effects. Furthermore, we assume the plasma parameter as well as the beam particle distribution function being constant. Consequently, this approach is only valid for the central part of the plasma column with flat profiles. The WVII-A stellarator has a large aspect ratio ($A = 20$) and very small helical field ripple ($< 2\%$); however, as a consequence of the real inhomogeneity of the magnetic field, we are restricted in $\underline{k}$-space for the stability analysis of the nearly perpendicular neutral beam injection: (i) $k_{\|} \cdot R/m \gg 1$ (R being the major radius and m the periodic number) and (ii) $k_{\perp}\, \rho_i > 1$ (ρ_i being the ion gyroradius). The first restriction prohibits the strongly simplifying approach $k_{\|} \to 0$, thus, we carry out the stability analysis depending on $k_{\|}$. The second restriction is completed by the condition of sufficiently small growth distance of instabilities ($\Im\mathrm{m}\{\omega\} > 0$): $\partial\omega/\partial k_{\perp} \ll \Im\mathrm{m}\{\omega\} \cdot r_a$ (r_a being the plasma radius). Only if this condition is valid, the instable modes can sufficiently grow within the plasma.

We define the $\underline{k}$-space being real and the angular frequency ω being complex. Negative imaginary parts of ω correspond to damped modes, positive imaginary parts to unstable modes. Modes are defined by the roots of the dielectric function (dispersion relation):

$$D(\omega, k_{\|}, k_{\perp}) = 0\,. \tag{1}$$

We use the definition of the dielectric function based on the dielectric tensor elements, ε_{ij} (see e.g. Akhiezer /19/):

$$\begin{aligned}
D &= A + \frac{B}{N^2} + \frac{C}{N^4} \qquad \text{with} \qquad N = \frac{ck}{\omega} \\
A &= (\frac{k_{\perp}}{k})^2 \varepsilon_{11} + 2\frac{k_{\|}\, k_{\perp}}{k^2}\varepsilon_{13} + (\frac{k_{\|}}{k})^2 \varepsilon_{33} \\
B &= -(\varepsilon_{11} + (\frac{k_{\|}}{k})^2 \varepsilon_{22})\,\varepsilon_{33} + \varepsilon_{13}{}^2 - (\frac{k_{\|}}{k})^2 \varepsilon_{23}{}^2 \\
&\quad - (\frac{k_{\perp}}{k})^2 (\varepsilon_{11}\varepsilon_{22} + \varepsilon_{12}{}^2) + 2\frac{k_{\|}\, k_{\perp}}{k^2}(\varepsilon_{12}\varepsilon_{23} - \varepsilon_{13}\varepsilon_{22}) \\
C &= (\varepsilon_{11}\varepsilon_{22} + \varepsilon_{12}{}^2)\,\varepsilon_{33} + \varepsilon_{11}\varepsilon_{23}{}^2 + 2\,\varepsilon_{12}\varepsilon_{13}\varepsilon_{23} - \varepsilon_{22}\varepsilon_{13}{}^2\,.
\end{aligned} \tag{2}$$

We take three components of the plasma into consideration: thermal electrons, thermal ions and the beam ion distribution. The dielectric tensor elements consist of two parts: $\varepsilon_{ij} = \varepsilon_{ij}^{p} + \varepsilon_{ij}^{b}$. The plasma contributions, ε_{ij}^{p}, are based on isotropic Maxwellians for the electrons as well as for the thermal ions. For Maxwellian distribution functions, the ε_{ij}

elements are well kown; in the following, we make some simplifications. We carry out the stability analysis in the frequency range of the ion cyclotron harmonics up to the lower hybrid frequency: $\omega \ll \omega_{ce}$. The wave lengths are typically of the order of the ion gyro radius, then, the conditions are valid: $k_{\|} v_e \ll \omega_{ce}$ and $k_{\perp} v_e \ll \omega_{ce}$. With these relations, we expand in the electron contribution to the dielectric tensor elements the modified Bessel sums as well as the plasma dispersion function, Z, (here, only the Landau damping term in the ε_{33} element remains unexpanded) with respect to their arguments. Furthermore, we assume the parallel wave lengths being large compared to the ion gyro radius: $k_{\|} v_i \ll \omega_{ci}$. Then, we use the asymptotic expansion of the plasma dispersion function, Z, in the ion contributions for the nonresonant terms ($\omega - l_i \omega_{ci} \not\approx 0$) in the Bessel sums.

For the most ion cyclotron modes, the frequency is close to a harmonic of the ion cyclotron frequency: $\omega - l_i \omega_{ci} \approx 0$; terms in the dielectric tensor elements related to this harmonic describe the resonant ion cyclotron damping, which is important for the stability analysis. With all these simplifications, the dielectric tensor, ε^p_{ij}, for a Maxwellian plasma can be written in the following form (with the usual notations):

$$
\begin{aligned}
\varepsilon^p_{11} &= 1 + \Big(\frac{\omega_{pe}}{\omega_{ce}}\Big)^2 + \Big(\frac{\omega_{pi}}{\omega_{ci}}\Big)^2 \frac{1}{b}\Big[S_1 + l_i^2 e^{-b} I_{l_i}(b)\big(x_0^i Z(x_l^i) - \frac{1}{2}\big) \cdot \frac{1}{\Omega^2}\Big] \\
\varepsilon^p_{22} &= \varepsilon^p_{11} + 2\Big(\frac{\omega_{pi}}{\omega_{ci}}\Big)^2 b\,\Big[S_2' + e^{-b}\big(I_{l_i}(b) - I_{l_i}'(b)\big)\,\big(x_0^i Z(x_l^i) - \frac{1}{2}\big) \cdot \frac{1}{\Omega^2}\Big] \\
\varepsilon^p_{33} &= 1 - \Big(\frac{\omega_{pe}}{k_{\|} v_e}\Big)^2 Z'(x_0^e) \; - \Big(\frac{\omega_{pi}}{\omega_{ci}}\Big)^2\Big[\frac{1}{l_i^2} S_2 + e^{-b} I_{l_i}(b)\,\big(\,x_0^i x_l^i Z'(x_l^i) + \frac{1}{2}\,\big) \cdot \frac{1}{\Omega^2}\Big] \\
\varepsilon^p_{12} &= \; -i\frac{\omega_{pe}^2}{\omega_{ci}\omega_{ce}}\frac{1}{\Omega} + i\Big(\frac{\omega_{pi}}{\omega_{ci}}\Big)^2 l_i\Big[\,S_1' - e^{-b}\big(I_{l_i}(b) - I_{l_i}'(b)\big)\,\big(x_0^i Z(x_l^i) + \frac{1}{2}\big)\,\Big] \cdot \frac{1}{\Omega^2} \\
\varepsilon^p_{13} &= \; -\Big(\frac{\omega_{pi}}{\omega_{ci}}\Big)^2 \frac{l_i}{\sqrt{2b}}\, e^{-b} I_{l_i}(b)\; x_0^i Z'(x_l^i) \cdot \frac{1}{\Omega^2} \\
\varepsilon^p_{23} &= i\Big(\frac{\omega_{pi}}{\omega_{ci}}\Big)^2 \sqrt{2b}\, e^{-b}\,\big(I_{l_i}(b) - I_{l_i}'(b)\big)\, x_0^i\,\big(x_l^i Z'(x_l^i) + 1\big) \cdot \frac{1}{\Omega^2} \\
\varepsilon_{21} &= \; -\varepsilon_{12} \qquad\qquad \varepsilon_{31} = \varepsilon_{13} \qquad\qquad \varepsilon_{32} = \; -\varepsilon_{23}
\end{aligned}
\tag{3}
$$

with the abbreviations:

$$
\Omega = \frac{\omega}{\omega_{ci}}; \qquad b = \frac{1}{2}\Big(\frac{k_{\perp} v_i}{\omega_{ci}}\Big)^2; \qquad x_0^e = \frac{\omega}{k_{\|} v_e}; \qquad x_l^i = \frac{\omega - l_i \omega_{ci}}{k_{\|} v_i}; \qquad v_{i,e}^2 = \frac{2T_{i,e}}{m_{i,e}}
$$

$$
S_1(b) = 2 \sum_{n=1,\neq l_i}^{\infty} \frac{n^2 e^{-b} I_n(b)}{n^2 - l_i^2}
$$

$$
\begin{aligned}
S_2(b) &= e^{-b} I_0(b) - 2\, l_i^2 \sum_{n=1,\neq l_i}^{\infty} \frac{e^{-b} I_n(b)}{n^2 - l_i^2} \\
&= 1 - e^{-b} I_{l_i}(b) - S_1(b)\,.
\end{aligned}
$$

The contribution of the slowing down distribution function of the beam particles to the dielectric tensor, ε_{ij}^{b}, can only be given in an analytical form for some simple models of distribution functions, e.g. for δ-δ and δ-*Maxwellian* distribution functions. The δ-δ distribution function,

$$f_{\delta\delta}(v_{\parallel}, v_{\perp}) = \frac{n_b}{2\pi v_{\perp}} \cdot \delta(v_{\perp} - u_{\perp}) \cdot \delta(v_{\parallel} - u_{\parallel}), \tag{4}$$

is the basis of the convolution formalism we use to calculate the contribution of the slowing down distribution functions estimated numerically by Monte Carlo simulation (see Chapter III and Appendix B). In the convolution formalism, which is outlined in Appendix A in more detail, the contribution of a δ-δ function to the dielectric tensor elements with a weight corresponding to the beam particle distribution at the specific $v_{\parallel}, v_{\perp}$ value is integrated over the velocity space and yields the beam particle contribution. However, this procedure is not straight foreward since the particle resonance effects ($\omega - l_b\omega_{cb} - k_{\parallel}v_{\parallel} \approx 0$) must be handled with care, the $v_{\parallel}$ integration of these resonant terms must be interpreted as a complex-valued Hilbert integral transform which has to be analytic in ω.

As we also use the δ-δ distribution function to compare the modes driven by the neutral beam injection depending on the form of the beam particle distributions, we have calculated the contributions, $\varepsilon_{ij}^{\delta\delta}$, to the dielectic tensor (only the $\varepsilon_{23}^{\delta\delta}$ element was disregarded); here, the harmonic number l_b is defined by $\omega - l_b\omega_{cb} \approx 0$:

$$\begin{aligned}
\varepsilon_{11}^{\delta\delta} = & -\left(\frac{\omega_{pb}}{\omega}\right)^2 \left\{ \frac{1}{a}\left[-l_b^2 R_1' + 4l_b^4 J_{l_b}(a) J_{l_b}'(a) Y_{l_b} \right] \right. \\
& \left. + \left(\frac{k_{\parallel}}{k_{\perp}}\right)^2 \left[2 \sum_{m=1,\neq l_b}^{\infty} \frac{m^2(m^2+l_b^2)}{(m^2-l_b^2)^2} J_m^2(a) + 4l_b^4 J_{l_b}^2(a) Y_{l_b}^2 \right] \right\} \\
\varepsilon_{22}^{\delta\delta} = & \left(\frac{\omega_{pb}}{\omega}\right)^2 \left\{ -1 + 4 \sum_{m=1,\neq l_b}^{\infty} \frac{m^2}{m^2-l_b^2} \left[a J_m'(a) J_m''(a) + {J_m'}^2(a) \right] \right. \\
& - 4l_b^2 \left[a J_{l_b}'(a) J_{l_b}''(a) + {J_{l_b}'}^2(a) \right] Y_{l_b} \\
& \left. - \left(\frac{k_{\parallel}}{k_{\perp}}\right)^2 a^2 \left[\frac{1}{l_b^2} {J_0'}^2(a) + 2 \sum_{m=1,\neq l_b}^{\infty} \frac{m^2+l_b^2}{(m^2-l_b^2)^2} {J_m'}^2(a) + 4l_b^2 {J_{l_b}'}^2(a) Y_{l_b}^2 \right] \right\} \\
\varepsilon_{33}^{\delta\delta} = & -\left(\frac{\omega_{pb}}{\omega}\right)^2 \left\{ 1 + 2\frac{k_{\parallel}u_{\parallel}}{l_b\omega_{cb}} \left[1 - R_1 - 2J_{l_b}^2(a) + l_b^2\left(1 + 2l_b \frac{k_{\parallel}u_{\parallel}}{\omega_{cb}} Y_{l_b}\right) J_{l_b}^2(a) Y_{l_b} \right] \right\} \\
\varepsilon_{12}^{\delta\delta} = & \, i \left(\frac{\omega_{pb}}{\omega}\right)^2 \left\{ 2l_b \sum_{m=1,\neq l_b}^{\infty} \frac{m^2}{m^2-l_b^2} \left[J_m'(a) \left(J_m'(a) + \frac{1}{a} J_m(a) \right) + J_m(a) J_m''(a) \right] \right. \\
& - 2l_b^3 \left[J_{l_b}'(a) \left(J_{l_b}'(a) + \frac{1}{a} J_{l_b}(a) \right) + J_{l_b}(a) J_{l_b}''(a) \right] Y_{l_b} \\
& \left. - 4l_b \left(\frac{k_{\parallel}}{k_{\perp}}\right)^2 a \left[\sum_{m=1,\neq l_b}^{\infty} \frac{m^2}{(m^2-l_b^2)^2} J_m(a) J_m'(a) + l_b^2 J_{l_b}(a) J_{l_b}'(a) Y_{l_b}^2 \right] \right\}
\end{aligned}$$

$$\varepsilon_{13}^{\delta\delta} = \left(\frac{\omega_{pb}}{\omega}\right)^2 \left\{ l_b \frac{u_\parallel}{u_\perp} \left[R_1' - 4 l_b^2 \, J_{l_b}(a) \, J_{l_b}'(a) \, Y_{l_b} \right] \right.$$
$$\left. + \frac{k_\parallel}{k_\perp} \left[R_1 - 4 l_b \frac{k_\parallel u_\parallel}{\omega_{cb}} \sum_{m=1,\neq l_b}^{\infty} \frac{m^2 \, J_m^2(a)}{(m^2 - l_b^2)^2} - 2 l_b^2 J_{l_b}^2(a) \left(1 + 2 l_b \frac{k_\parallel u_\parallel}{\omega_{cb}} Y_{l_b}\right) Y_{l_b} \right] \right\} \tag{5}$$

with the abbreviations

$$a = \frac{k_\perp u_\perp}{\omega_{cb}}; \qquad Y_{l_b} = \frac{{\omega_{cb}}^2}{(\omega - k_\parallel u_\parallel)^2 - l_b^2 {\omega_{cb}}^2}; \qquad R_1 = 2 \sum_{m=1,\neq l_b}^{\infty} \frac{m^2}{m^2 - l_b^2} \, J_m^2(a) \, .$$

The tensor elements, $\varepsilon_{ij}^{\delta M}$, based on a *δ-Maxwellian* distribution function, which are given in Appendix E, can be reduced to the $\varepsilon_{ij}^{\delta\delta}$ elements by means of the limit $\Delta u_\parallel \to 0$. With the tensor elements $\varepsilon_{ij}^{\delta\delta}$, we can check the order of magnitude of the terms in the dispersion relation (1) for the different ion cyclotron modes. From this procedure we found, that the ε_{11}^b tensor element is the most important one for the stability analysis of the neutral beam injection within the whole range of ion cyclotron harmonics investigated in this report. As the ε_{33} element is dominated by electron Landau damping (see below), we treated only the diagonal elements, ε_{11}^b and ε_{22}^b, of the beam particle contribution within the numerical convolution formalism, all other terms were found to be neglectable with respect to the instabilities driven by the neutral beam injection. However, the convolution formalism can be easily extended to the other tensor elements.

In the numerical calculations, we take all terms into account which are given explicitely in this report. However, the dielectric function (eq. 2) can be strongly simplified for analytical approximations. This is necessary in order to characterize the ion cyclotron modes for the different harmonics and to find the regions of instability in $\underline{k}$-space. The ε_{33} dielectric tensor element is dominated by electron Landau damping, ion Landau damping as well as beam particle contributions are neglectable. The ε_{33} element (eq. 3) can be written in the form:

$$\varepsilon_{33} \approx -\left(\frac{\omega_{pe}}{\omega} \, x_0^e\right)^2 \cdot Z'(x_0^e) \quad \overset{k_\parallel \to 0}{\longrightarrow} \quad -\left(\frac{\omega_{pe}}{\omega}\right)^2 \qquad \text{with} \quad x_0^e = \frac{\omega}{k_\parallel v_e} \, . \tag{6}$$

The ε_{33} element is the leading term in the dielectric function (eq. 2). For the ion cyclotron modes of interest, N is very large and we can neglect the C term in the dielectric function. With $k_\parallel \ll k_\perp$, we can neglect the ε_{13} term in A and get with $B \approx -\varepsilon_{11}\varepsilon_{33}$ the simplified dispersion relation

$$D \approx \varepsilon_{11} \cdot \left(1 - \frac{\omega^2}{c^2 k^2} \varepsilon_{33}\right) + \frac{k_\parallel^2}{k^2} \varepsilon_{33} = 0 \, . \tag{7}$$

III. Beam Particle Distribution Functions $f_b(v_\parallel, v_\perp)$

In this section, we describe slowing down distribution functions of the beam ions calculated by means of Monte Carlo simulation which are used for the linear stability analysis in $\underline{k}$-space for the different ion cyclotron harmonics. These distributions based only on Coulomb interaction are a model for the nearly perpendicular neutral beam injection in the WVII-A stellarator; the simulation technique and the injection model are described in Appendix B in more detail. In Appendix F we compare the instabilities driven by these distribution functions with simplified analytical models (based on δ-δ and δ-*Maxwellian* distribution functions). We assume the thermal plasma components being isotropic Maxwellians with given temperatures. Furthermore, we assume hydrogen injection in a deuterium target plasma for all calculations of this report and neglect hydrogen in the thermal component.

Since we neglect the configuration space dependence, we use only central values for the plasma parameters. Monte Carlo simulations of the neutral beam injection heating based only on Coulomb friction (ODIN code, see /20/) show the influence of radial electric fields on the confinement of the fast particles: the orbit losses can be significantly decreased leading to an improved heating efficiency. For these situations, we neglect the transport effects during the slowing down of the beam particles. This type of beam particle distribution functions models the central region of the plasma column for very good confinement properties. On the other hand, we model worse confinement properties by introducing a loss cone in the velocity space describing the fast loss of particles being trapped in the helical magnetic field ripple. This effect can have great influence on the distribution functions for the nearly perpendicular injection although the helical field ripple is very small in the WVII-A stellarator. As the field ripple increases with the plasma radius, we use an average value being smaller than the maximum value of 2% at the edge; the average value is defined by the central region with nearly constant density and temperature ($< 5\ cm$ in radius). In the simulations with loss cone effects included, we assume an average loss rate linear related to the particle energy simulating the ∇B-drift of helically trapped particles. The trapping in the loss cone is defined by the pitch of the particles: $p^2 < B_h/B_0$ where B_h is the helical magnetic field ripple and p is the pitch, $v_\parallel/v$. In this context, we analyze only strong loss cone effects on the slowing down distribution functions.

As the transient slowing down distributions after switching in the neutral beam injection are expected to be more unstable than the stationary distributions, we use two models for the stability analysis of the transient distribution functions: at $t = \tau_{SD}/8$ (data sets DMCT08 in Fig. 1 and DMCT08A in Fig. 2) and at $t = \tau_{SD}/2$ (data sets DMCT02 in Fig. 3 and DMCT02A in Fig. 4) after switching in the neutral beam injection where τ_{SD} is the average slowing down time. In these transient distribution functions, the peaks close to the injection energies are much more pronounced than in the stationary distribution function without loss cone effects (data sets DMC327 in Fig. 5 and DMC327A in Fig. 6); especially the regions in the velocity space with $\partial f_b \,/\, \partial v_\perp$ dominate which can drive ion cyclotron instabilities. For these slowing down distribution functions of the beam particles,

two values of central plasma temperatures are considered: the start phase of the neutral beam injection which is mainly characterized by low temperatures ($T_e \simeq T_i \simeq 400\ eV$ in the data sets DMCT08A, DCMT02A and DMC327A) and the phase of maximum energy content with high ion temperature ($T_e \simeq 600\ eV < T_i \simeq 1\ keV$ in all other cases). In the case of the high ion temperature, the slowing down distributions are broader in $v_{\|}$ than in the first case due to stronger pitch angle scattering which increases with the ion temperature.

Finally, two distribution functions with loss cone effects are analyzed: with a beam particle confinement time of the order of magnitude of the average slowing down time (data set DMCLC1 in Fig. 7) and with a confinement time further reduced (data set DMCLC2 in Fig. 8). The pitch of the loss cone in the first case corresponds to an average helical field ripple, B_h/B_0, of about 0.5%, in the second case to a value of 1%. In both cases, the distributions are strongly modified by the loss cone, especially the regions with $\partial f_b \,/\, \partial v_\perp$ are much more pronounced than in the case without losses (compare with the data set DMC327 in Fig. 5).

In the following, we estimate the beam ion density, n_b, by use of the neutral beam heating power absorbed in the plasma which is estimated experimentally. For the neutral beam heating power absorbed by the plasma, we assume a typical value of about 100 kW per beam line (compare to the total power of about 250 kW per beam line). Then, both the shine through and the fast orbit losses are already taken into account. With 3 beam lines, we get a central heating power density of about 3 W/cm^3. With an average energy of 14.2 keV per injected particle, the neutral beam density source strength, $\dot{n}_b$, is about $1.3 \cdot 10^{15}\ cm^{-3}\, s^{-1}$. For the transient distributions, the beam particle density is given by $n_b = t \cdot \dot{n}_b$ where t is the time after switch on the injection. In the case of stationary conditions without loss cone, the beam particle density is $n_b = \tau_{SD} \cdot \dot{n}_b$; this density is reduced for the distributions with loss cone effects by a factor of $\tau_C \,/\, (\tau_C + \tau_{SD})$ with τ_C being the average confinement time of the beam particles. With the value of the plasma density, $n_e = 5 \cdot 10^{13}\ cm^{-3}$, used for the calculations, we get a maximum beam contribution of about 15% for the stationary conditions (see /17/).

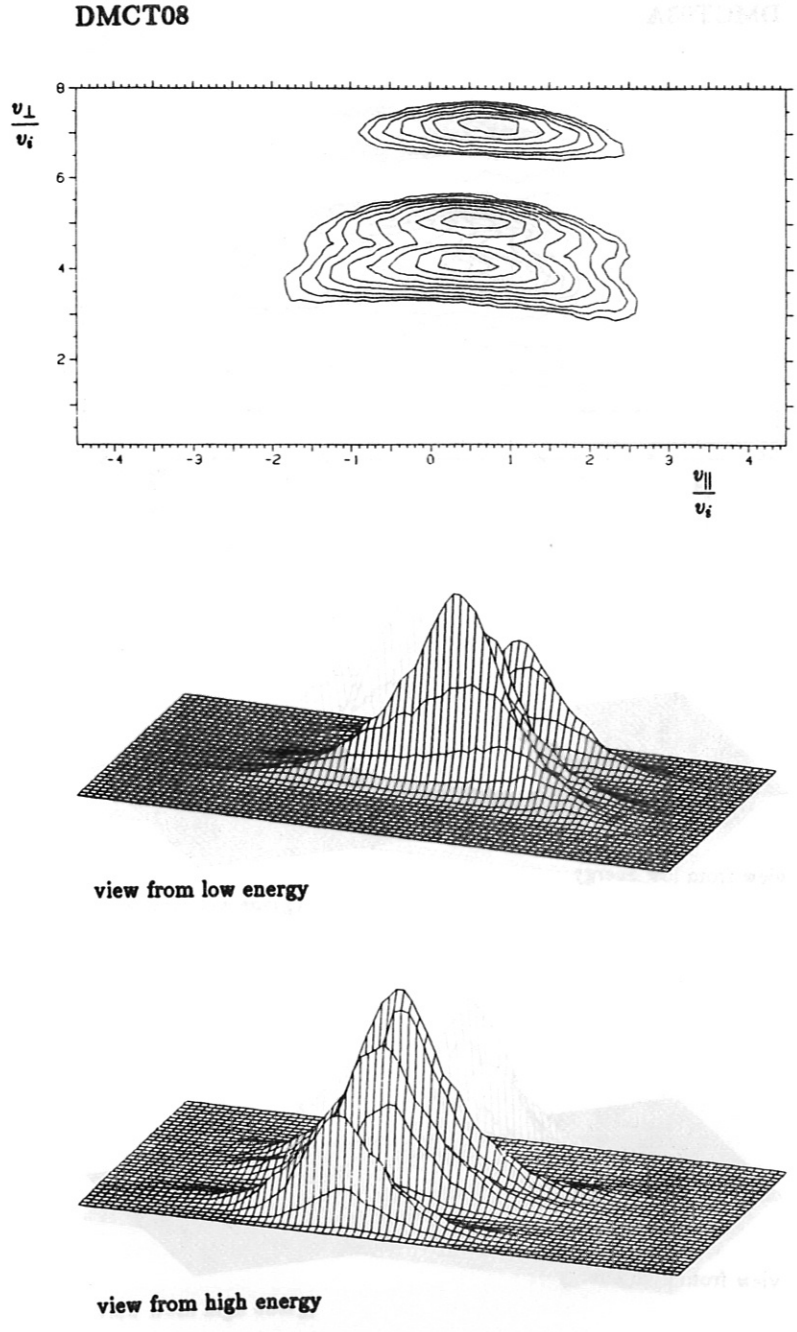

Fig. 1 *Transient slowing down distribution function* DMCT08: *isolines and perspective plots of* $v_\perp \cdot f_b(v_\parallel, v_\perp)$ *in velocity space calculated by Monte Carlo simulation. A maximum number of 50,000 simulation particles was used for these calculations. Time after switching on the beam lines:* $\tau_{SD}/8$ ($\simeq 0.63\ ms$). *Plasma parameter:* $T_e = 0.6\ keV$, $T_i = 1.0\ keV$, $n_e = 5 \cdot 10^{13}\ cm^{-3}$.

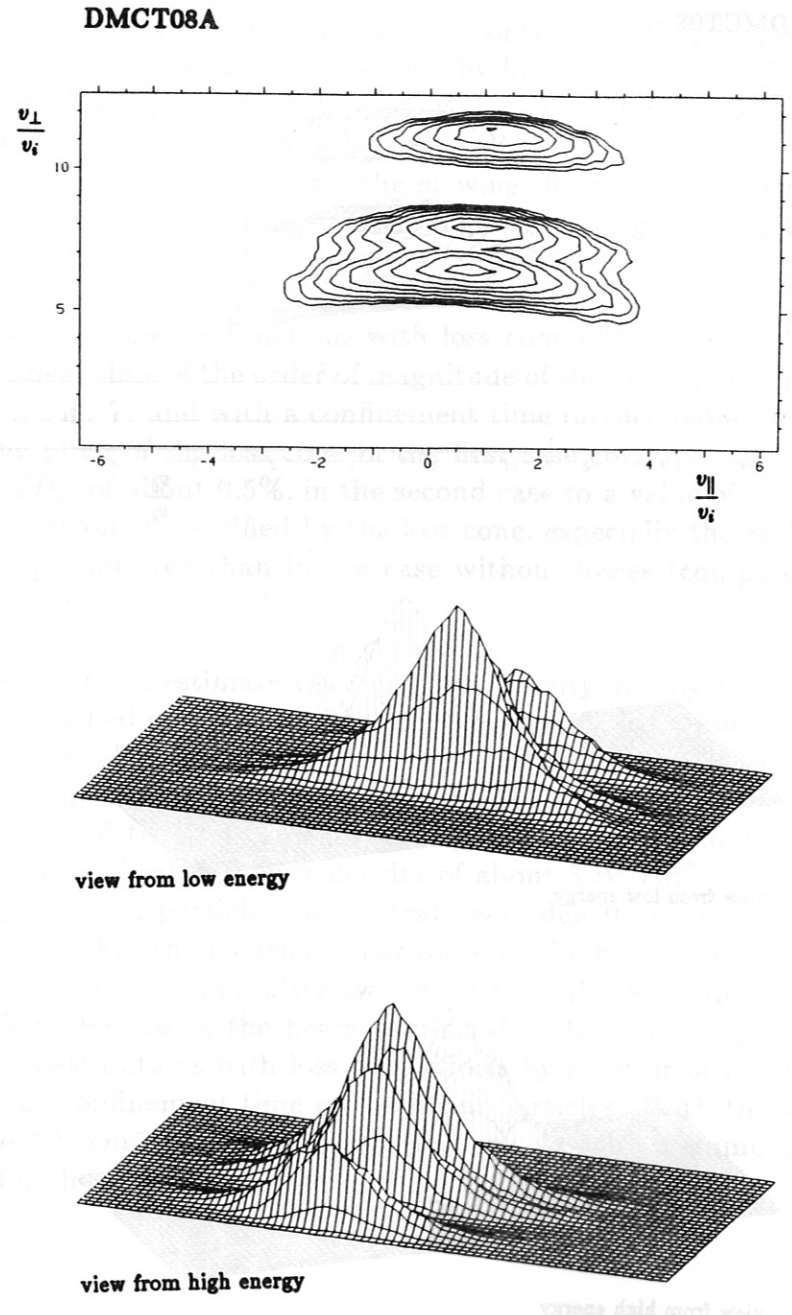

Fig. 2 *Transient slowing down distribution function* DMCT08A: *isolines and perspective plots of* $v_\perp \cdot f_b(v_\parallel, v_\perp)$ *in velocity space calculated by Monte Carlo simulation. A maximum number of 50,000 simulation particles was used for these calculations. Time after switching on the beam lines:* $\tau_{SD}/8$ ($\simeq 0.54\ ms$). *Plasma parameter:* $T_e = 0.4\ keV$, $T_i = 0.4\ keV$, $n_e = 5 \cdot 10^{13}\ cm^{-3}$.

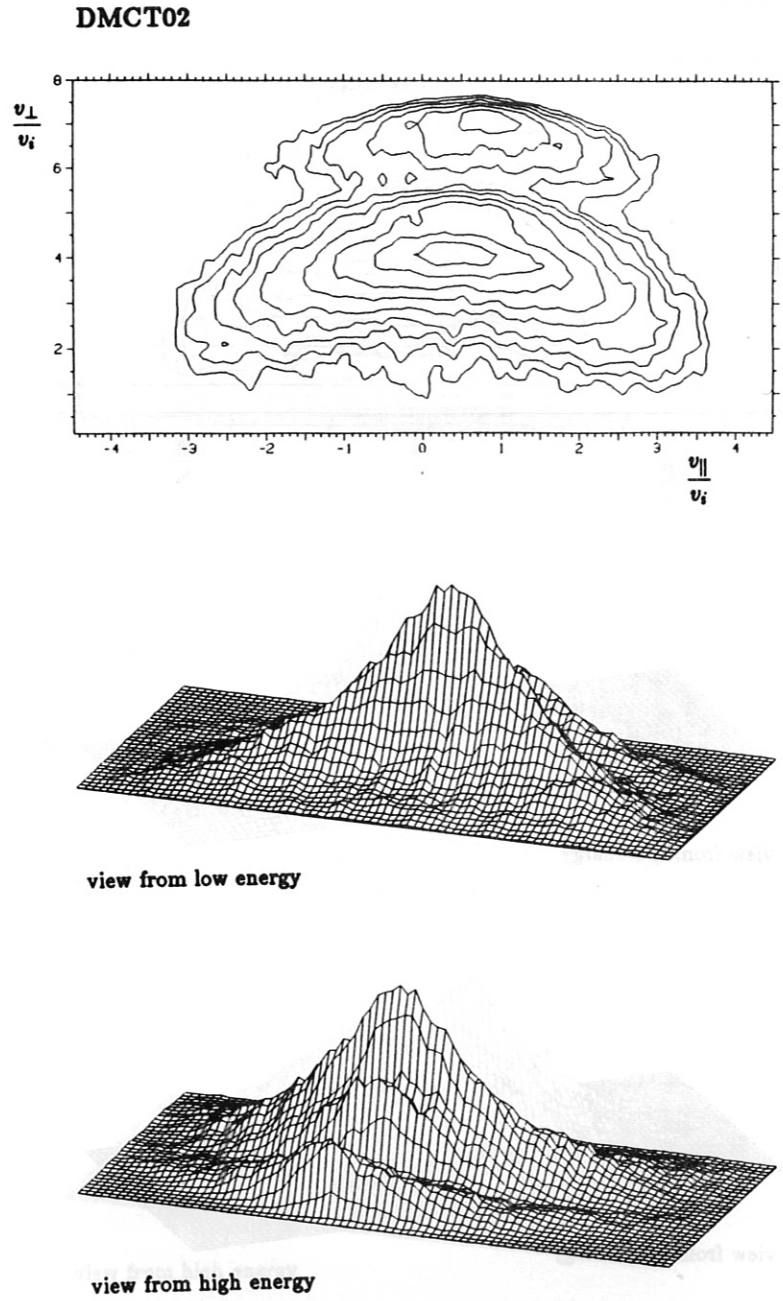

Fig. 3 *Transient slowing down distribution function* DMCT02: *isolines and perspective plots of* $v_\perp \cdot f_b(v_\parallel, v_\perp)$ *in velocity space calculated by Monte Carlo simulation. A maximum number of 50,000 simulation particles was used for these calculations. Time after switching on the beam lines:* $\tau_{SD}/2$ ($\simeq 2.5\ ms$). *Plasma parameter:* $T_e = 0.6\ keV$, $T_i = 1.0\ keV$, $n_e = 5 \cdot 10^{13}\ cm^{-3}$.

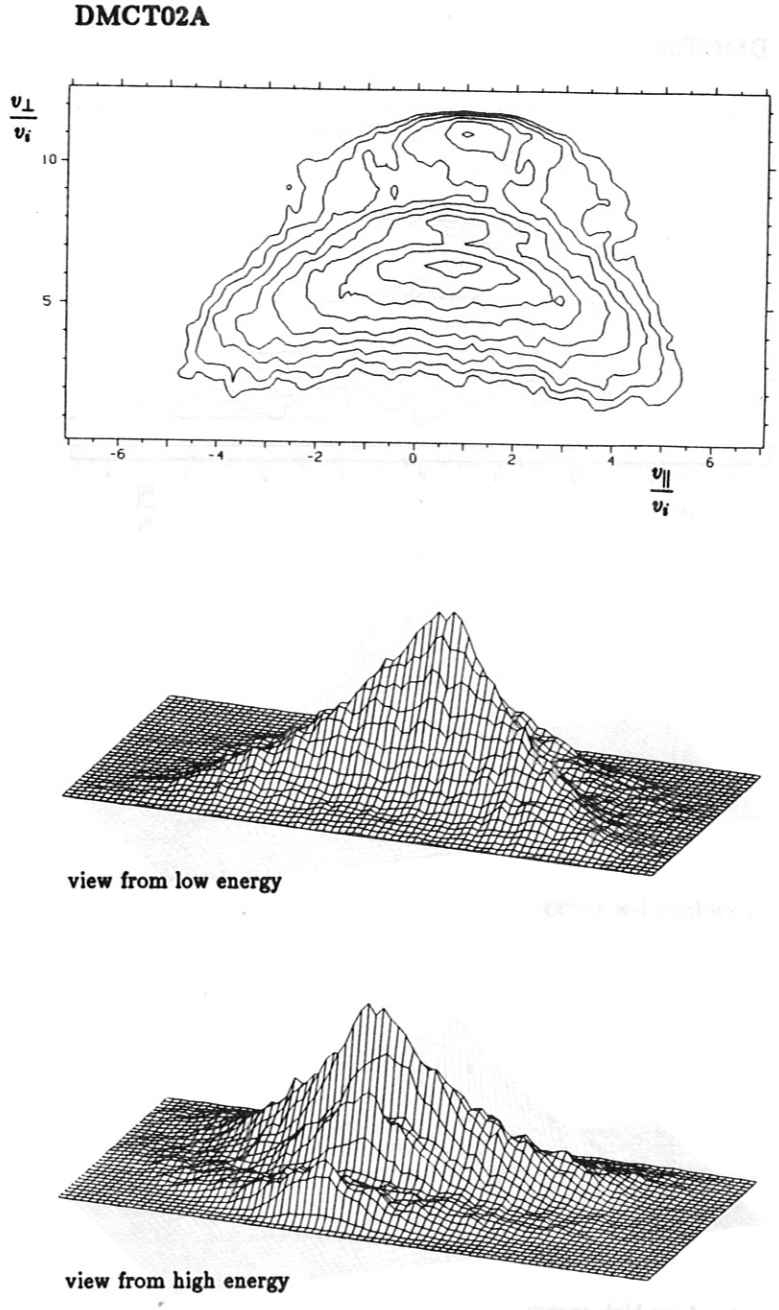

Fig. 4 *Transient slowing down distribution function* DMCT02A: *isolines and perspective plots of* $v_\perp \cdot f_b(v_\parallel, v_\perp)$ *in velocity space calculated by Monte Carlo simulation. A maximum number of 50,000 simulation particles was used for these calculations. Time after switching on the beam lines:* $\tau_{SD}/2$ ($\simeq 2.2\ ms$). *Plasma parameter:* $T_e = 0.4\ keV$, $T_i = 0.4\ keV$, $n_e = 5 \cdot 10^{13}\ cm^{-3}$.

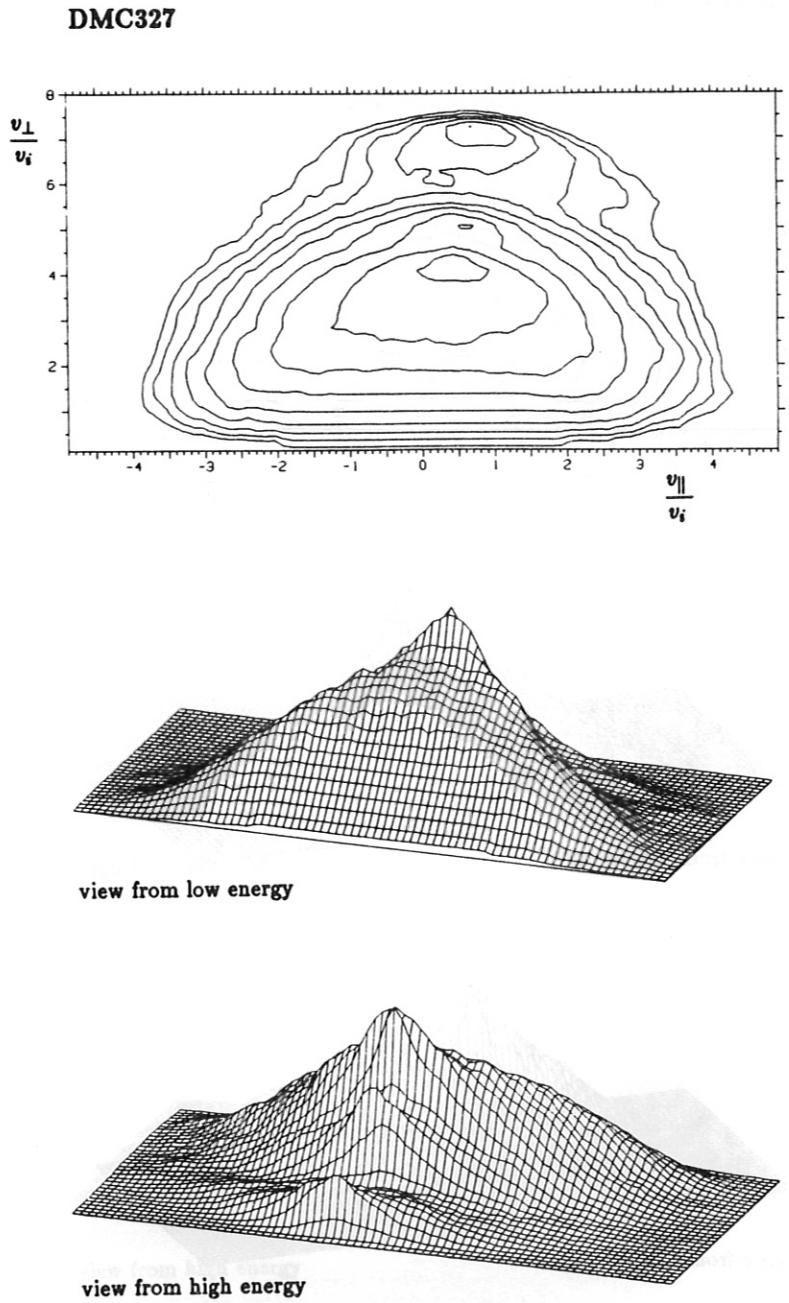

Fig. 5 *Stationary slowing down distribution function* DMC327: *isolines and perspective plots of* $v_\perp \cdot f_b(v_\parallel, v_\perp)$ *in velocity space calculated by Monte Carlo simulation. The distribution function is estimated from 2,000 simulation particles by means of time averaging. Average slowing down time (from the simulation):* $\tau_{SD} \simeq 5.8\ ms$. *Plasma parameter:* $T_e = 0.6\ keV$, $T_i = 1.0\ keV$, $n_e = 5 \cdot 10^{13}\ cm^{-3}$.

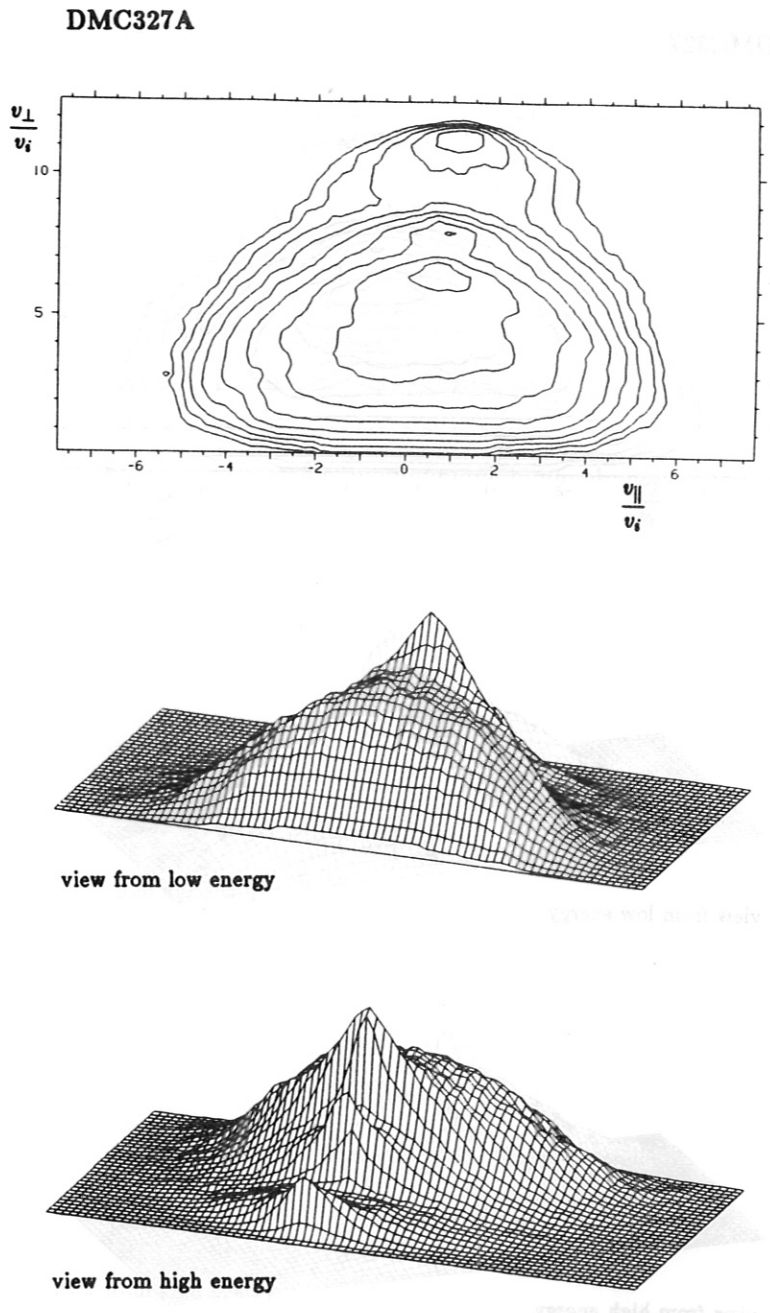

Fig. 6 *Stationary slowing down distribution function* DMC327A: *isolines and perspective plots of* $v_\perp \cdot f_b(v_\parallel, v_\perp)$ *in velocity space calculated by Monte Carlo simulation. The distribution function is estimated from 2,000 simulation particles by means of time averaging. Average slowing down time (from the simulation):* $\tau_{SD} \simeq 4.4\ ms$. *Plasma parameter:* $T_e = 0.4\ keV$, $T_i = 0.4\ keV$, $n_e = 5 \cdot 10^{13}\ cm^{-3}$.

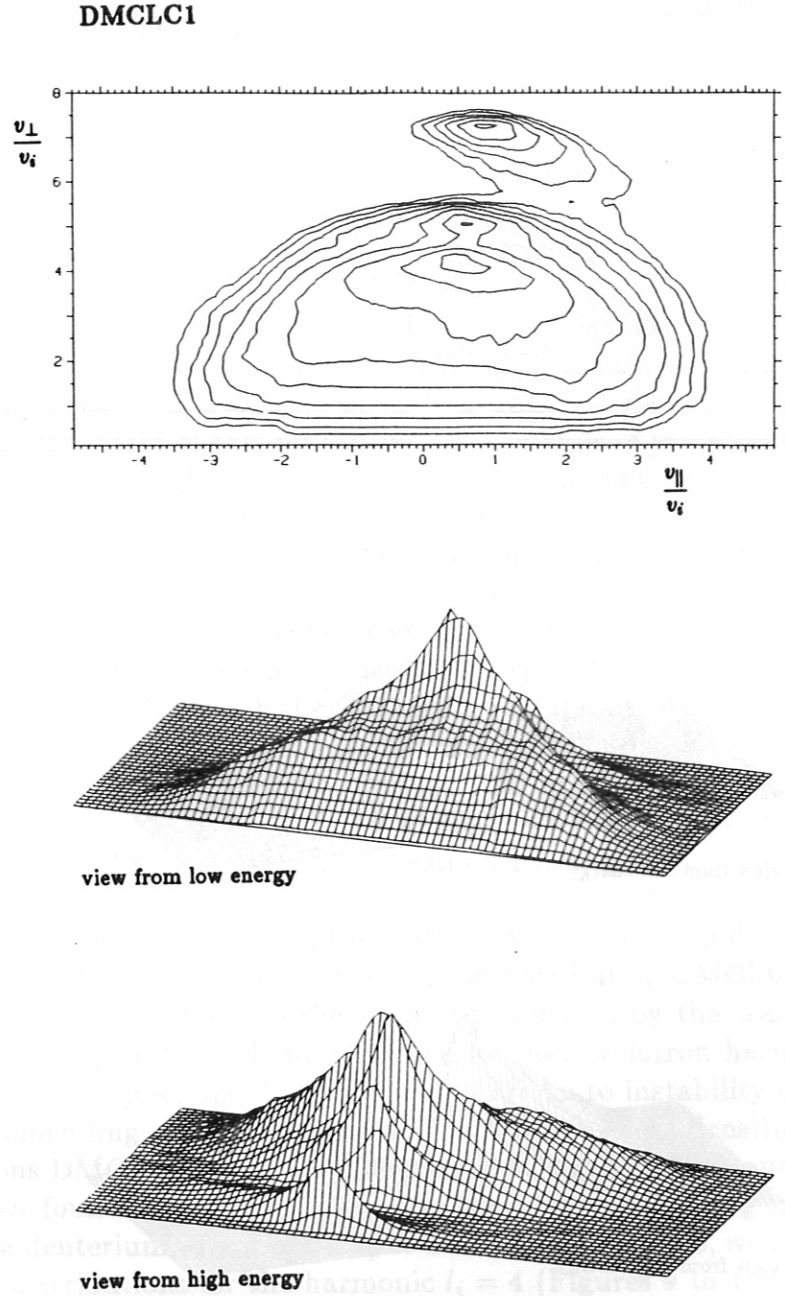

Fig. 7 *Stationary slowing down distribution function with loss cone effects* DMCLC1: *isolines and perspective plots of* $v_\perp \cdot f_b(v_\parallel, v_\perp)$ *in velocity space calculated by Monte Carlo simulation. The distribution function is estimated from 1,000 simulation particles by means of time averaging. The loss cone is defined by a pitch value,* $v_\parallel / v$, *of 0.064; the average confinement time of the beam particles in the simulation is* 5.0 *ms. Average slowing down time (from the simulation):* $\tau_{SD} \simeq 5.8$ *ms.*
Plasma parameter: $T_e = 0.6$ *keV*, $T_i = 1.0$ *keV*, $n_e = 5 \cdot 10^{13}$ cm^{-3}.

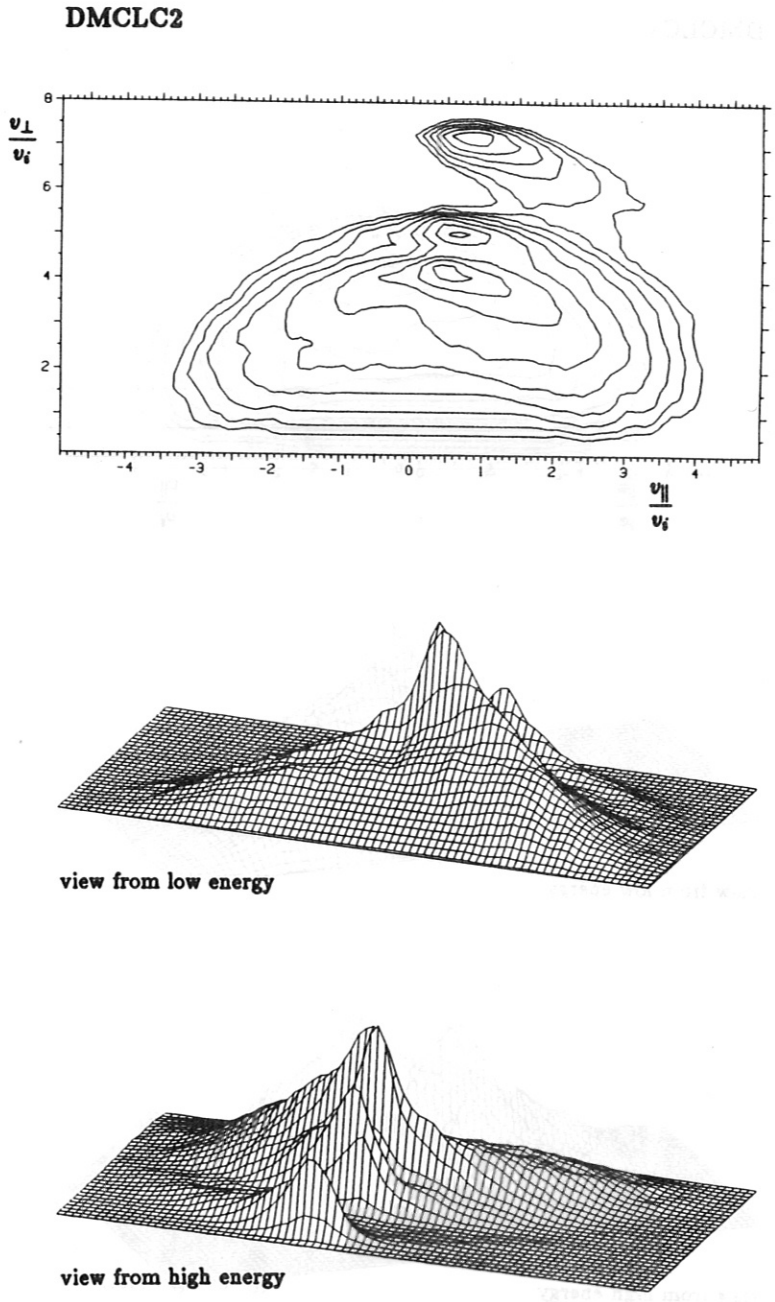

Fig. 8 *Stationary slowing down distribution function with loss cone effects* DMCLC2: *isolines and perspective plots of* $v_\perp \cdot f_b(v_\parallel, v_\perp)$ *in velocity space calculated by Monte Carlo simulation. The distribution function is estimated from 1,000 simulation particles by means of time averaging. The loss cone is defined by a pitch value,* $v_\parallel/v$, *of 0.09; the average confinement time of the beam particles in the simulation is 2.8 ms. Average slowing down time (from the simulation):* $\tau_{SD} \simeq 5.8\ ms$.
Plasma parameter: $T_e = 0.6\ keV$, $T_i = 1.0\ keV$, $n_e = 5 \cdot 10^{13}\ cm^{-3}$.

IV. Instabilities in the Low Harmonic Range

From now on, we summarize the results of the linear stability analysis based on the different beam ion distribution functions described in Chapter III. First, we make some remarks on the numerical calculations the results of which are outlined in the following Chapters for the different ranges of ion cyclotron harmonics.

For each harmonic, l_i, we start the stability analysis with an investigation of the $k_\perp$-range for which unstable ($\Im\mathrm{m}\{\omega\} > 0$) ion cyclotron modes driven by the beam particle distribution may exist; the procedure of finding these $k_\perp$-ranges is outlined in Appendix C. The fundamental point of this procedure is the analyis of the resonant terms in the ε^b_{11} tensor element which is the most important term in the dielectric function (comp. eq. 7). Then, with specified values of $k_\parallel$ and $k_\perp$, we find the roots of the dielectric function by use of the Cauchy rootfinder routine corresponding to unstable or weakly damped modes. Since the convolution formalism to calculate ε^b_{ij}, which is in main parts independent on $k_\parallel$ (see Appendix A), is numerically time expensive, we follow the modes of interest for fixed $k_\perp$ only in $k_\parallel$ solving the dispersion relation (eq. 1) with a simple gradient method. This is done for all $k_\perp$ values for which the modes are unstable. In most of the following figures, we use 1-dim. representations: the results for the maximum normalized growth rates, $\gamma = \Im\mathrm{m}\{\omega\}/\omega_{ci}$, with respect to $k_\parallel$ ($\partial\gamma/\partial k_\parallel = 0$) are plotted versus $k_\perp$. Furthermore, group velocities, $\underline{v}^G = \underline{\nabla}_k\omega$, electric fields and the absorption by the thermal ions and electrons (by means of Ohm's law) can be estimated.

For the low harmonics ($l_i \leq 10$), the stationary slowing down distribution functions of the beam ions were found to be stable (except the distribution DMCLC2, which is marginal unstable). Therefore, we describe the instabilities driven by the transient beam particle distribution functions in this Chapter. In the low ion cyclotron harmonic range, the ion Bernstein mode (see Appendix D and F) can by driven to instability by the beam particle distributions depending on the density n_b. For realistic beam densities ($n_b/n_e \simeq 0.02$ for the distributions DMCT08 and DMCT08A and 0.07 for DMCT02 and DMCT02A, comp. Chapter III), we found the fundamental mode ($l_b = 1$ corresponding to $l_i = 2$ for hydrogen injection into a deuterium target plasma) to be stable. Therefore, we compare the different beam particle distributions for the harmonic $l_i = 4$ (Figures 9 to 12).

The results of the distribution DMCT08A for the range in $\kappa_\perp = k_\perp\rho_i$ ($\rho_i = v_i/\omega_{ci}$ being the ion gyro radius) where the ion Bernstein mode is unstable are shown in Figure 9 for the growth rates, γ, being maximum with respect to $k_\parallel$. This $k_\perp$-range with $\gamma > 0$ (s. Fig. 9b) is related to the domains in the distribution function with $\partial f_b/\partial v_\perp > 0$; for $l_i = 4$, the instabilities are mainly related to the peak of the 9 keV beam particles. Here, we investigate the case of counter wave propagation with respect to the neutral beam injection ($k_\parallel u_\parallel < 0$) since the growth rates are much larger than in the case $k_\parallel u_\parallel > 0$ (comp. Figs. 9e and 9f); the frequency shift, $\delta\omega$, however, is similar for both cases. The frequency shift, $\delta\omega$, of the ion Bernstein mode depends strongly on $k_\perp$ (Fig. 9a) as well as

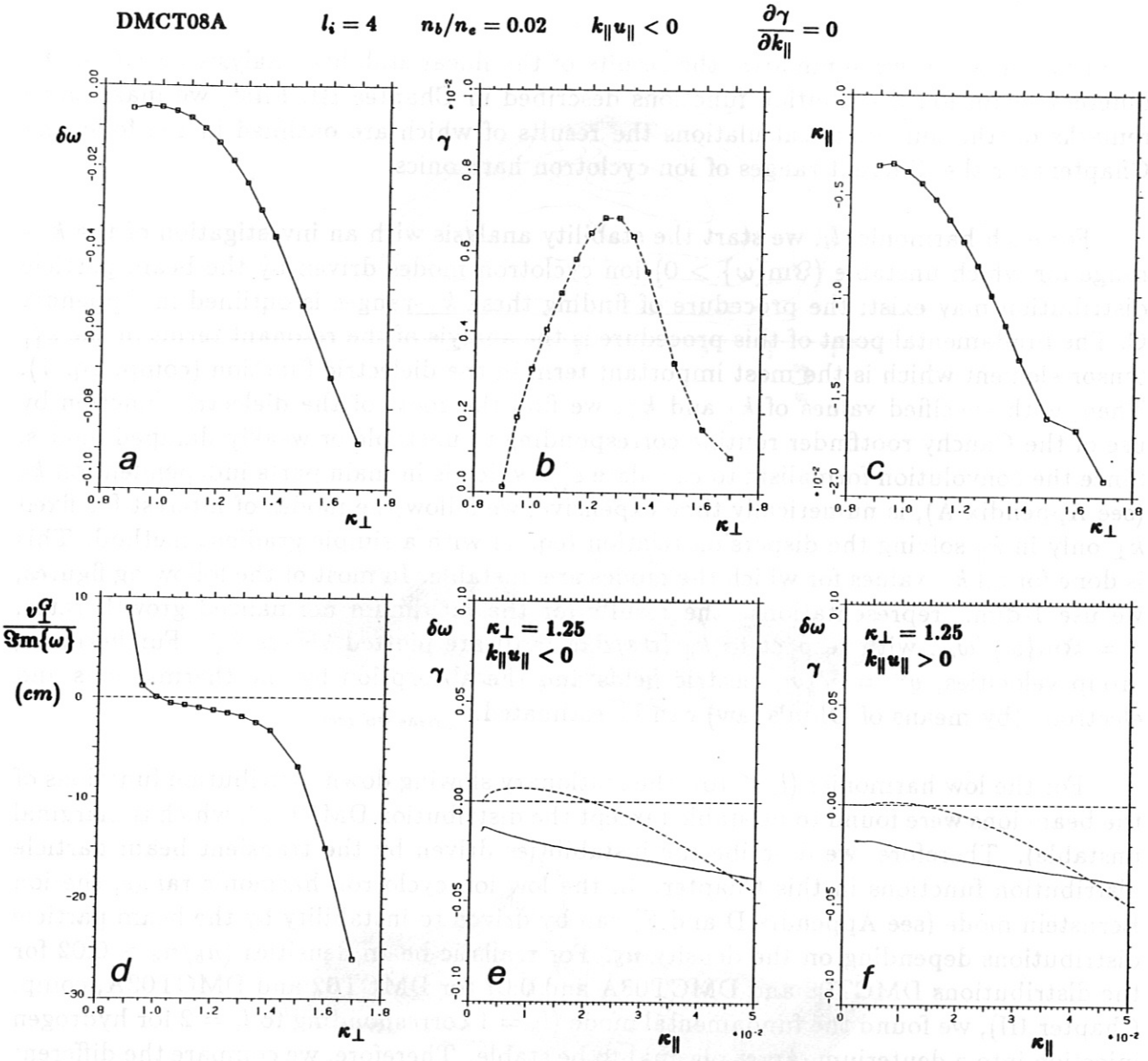

Fig. 9 *Ion cyclotron instability (harmonic $l_i = 4$) driven by the transient distribution* DMCT08A: *normalized frequency shift, $\delta\omega = \Re e\{\omega\}/\omega_{ci} - l_i$, and normalized growth rate, $\gamma = \Im m\{\omega\}/\omega_{ci}$, (Fig. 9a and 9b) versus normalized perpendicular wave length, $\kappa_\perp = k_\perp \rho_i$, for γ being maximum with respect to $\kappa_\parallel$ (these values in Fig. 9c). In Figure 9d, the mode increase distance, $v_\perp^G/\Im m\{\omega\}$, is plotted. Figures 9e and 9f show $\delta\omega$ (solid lines) and γ (broken lines) versus $\kappa_\parallel$ for fixed $k_\perp$ for counter ($k_\parallel u_\parallel < 0$) and for co ($k_\parallel u_\parallel > 0$) wave propagation with respect to the neutral beam injection.*
Plasma parameter: $B_0 = 3.2\ T$, $T_e = 400\ eV$, $T_i = 400\ eV$, $n_e = 5 \cdot 10^{13}\ cm^{-3}$

on the $k_{||}$-value of the maximum growth rate (Fig. 9c). This effect also appears in the case of pure Maxwellian plasma (comp. Figs. D1 and D2). For $\kappa_\perp \simeq 1$, the group velocity $\underline{v}^G = \underline{\nabla}_k \omega$ is very small resulting in a small perpendicular growth distance $v_\perp^G / \Im\mathrm{m}\{\omega\}$ (see Fig. 9d). The energy of the unstable mode remains localized in the plasma so that the beam particle distribution function is strongly affected by the electric fields connected with the instability. For larger values of $\kappa_\perp$ (> 1.5), γ is comparable, however, the electric fields remain much smaller as the group velocity $v_\perp^G$ is increased.

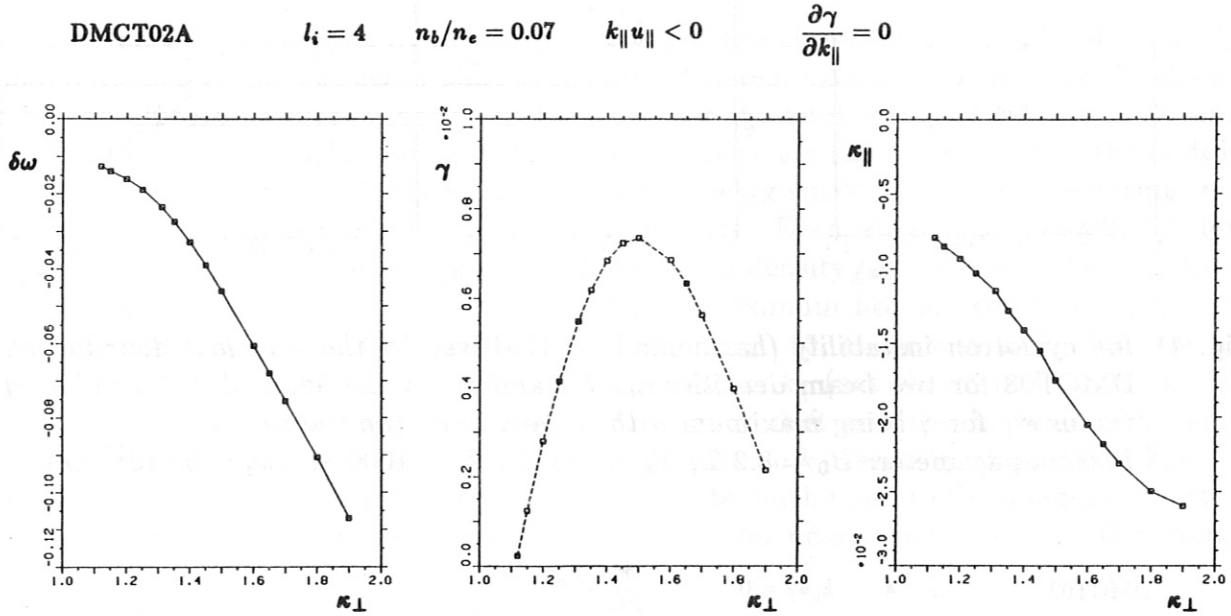

Fig. 10 *Ion cyclotron instability (harmonic $l_i = 4$) driven by the transient distribution* DMCT02A: *$\delta\omega$ and γ (on the left and in the middle) versus $\kappa_\perp$ for γ being maximum with respect to $\kappa_{||}$ (on the right).*
Plasma parameter: $B_0 = 3.2\ T$, $T_e = 400\ eV$, $T_i = 400\ eV$, $n_e = 5 \cdot 10^{13}\ cm^{-3}$

The ion cyclotron instability driven by the distribution function DMCT02A (Fig. 10) is very similar as for the distribution DMCT08A. However, we assumed a higher beam density to get analogous growth rates, γ. The frequency shift, $\delta\omega$, of the ion Bernstein mode is also nearly the same. The domain in the distribution function with $\partial f_b / \partial v_\perp > 0$ is decreased in energy within the slowing down (and the gradient is smaller), therefore, the $k_\perp$-range related to this region in $v_\perp$ (energy below the 9 keV-peak) is shifted up. Also the mode increase distances are similar as for the distribution DMCT08A, however, no change in the sign of $v_\perp^G$ exists in this $k_\perp$-range.

The beam particle distributions at the starting phase of the neutral beam injection, where the plasma temperature is low (DMCT08A and DMCT02A), are more unstable than the distributions DMCT08 and DMCT02 (see Figs. 11 and 12) in the high temperature case; for these distributions, we used also higher values of the beam density. The above

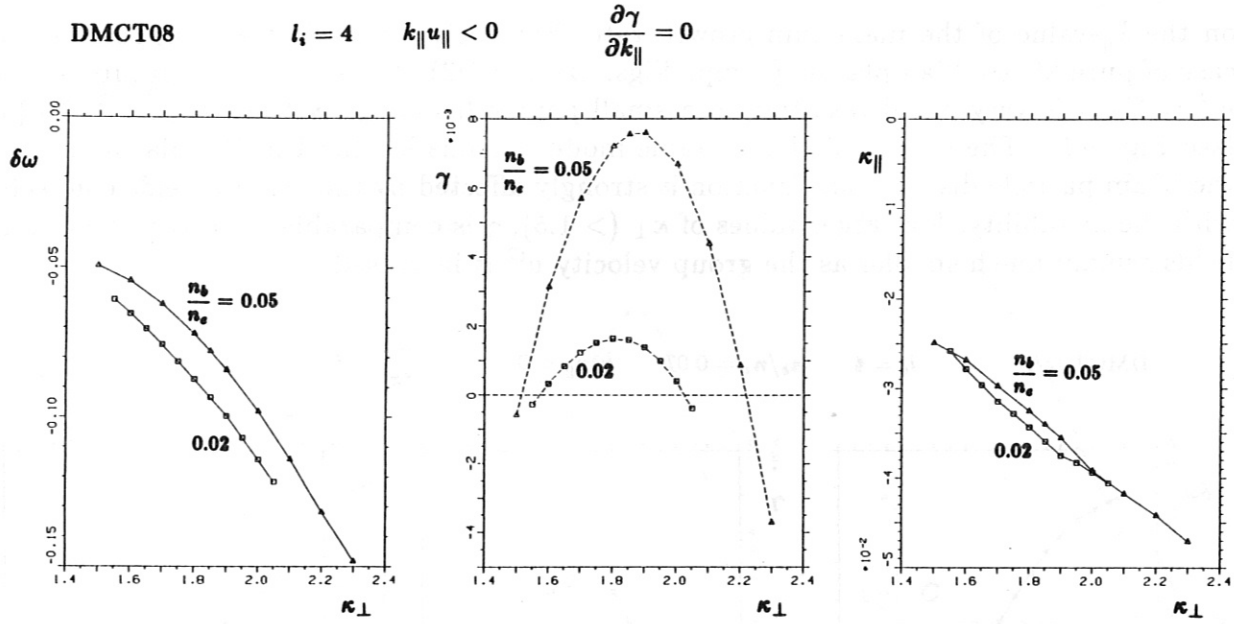

Fig. 11 *Ion cyclotron instability (harmonic $l_i = 4$) driven by the transient distribution* DMCT08 *for two beam densities n_b: $\delta\omega$ and γ (on the left and in the middle) versus $\kappa_\perp$ for γ being maximum with respect to $\kappa_\parallel$ (on the right).*
Plasma parameter: $B_0 = 3.2\ T$, $T_e = 600\ eV$, $T_i = 1000\ eV$, $n_e = 5 \cdot 10^{13}\ cm^{-3}$

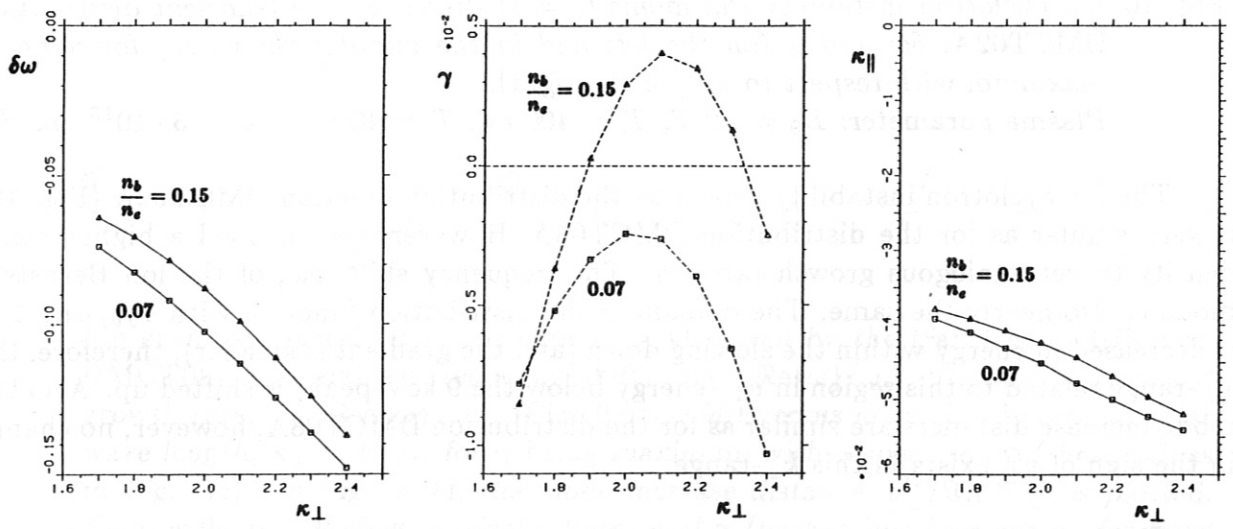

Fig. 12 *Ion cyclotron instability (harmonic $l_i = 4$) driven by the transient distribution* DMCT02 *for two beam densities n_b: $\delta\omega$ and γ (on the left and in the middle) versus $\kappa_\perp$ for γ being maximum with respect to $\kappa_\parallel$ (on the right).*
Plasma parameter: $B_0 = 3.2\ T$, $T_e = 600\ eV$, $T_i = 1000\ eV$, $n_e = 5 \cdot 10^{13}\ cm^{-3}$

mentioned effect of the upshift of the $k_\perp$-range with $\gamma > 0$ also appears. In comparison to the lower temperature distributions, the $k_\perp$-ranges are more narrow (notice the scaling faktor of ~ 1.6 due to ρ_i); the frequency shift, $\delta\omega$, as well as the $k_{||}$-values of γ being maximum have weaker dependence on $k_\perp$ and are but slightly influenced by the beam density, n_b. However, for both distributions DMCT08 and DMCT02, the normalized growth rates, γ, of the ion Bernstein mode are strongly increased with the beam density; the distribution DMCT02 becomes only unstable for the higher beam density case (Fig. 12).

For very low harmonics l_i, the density, n_b, of the beam particle distribution has only small influence on the frequency shift of the ion Bernstein mode, but may drive this mode to be unstable. This effect is shown in Figure 13 for the most unstable beam distribution DMCT08A. Here, the maximum growth rates in $\underline{k}$-space are calculated (plot in the middle of Fig. 13) dependent on the beam density; for n_b being small, the maximum normalized growth rate, γ, is linear related to the beam density. Even for $n_b/n_e = 0.002$, the ion Bernstein mode is unstable, no threshold in the beam density can be seen. The frequency shift as well as the $k_{||}$ and $k_\perp$ values of γ being maximum become constant with very small beam densities. For the whole range of n_b of Fig. 13, $\delta\omega$ as well as $k_\perp$ for γ being maximum are but slightly affected and the variation in $k_{||}$ (not shown in Fig. 13) is less than 10%. For fixed n_b, however, both the frequency shift and the $k_{||}$ value of γ being maximum with respect to $k_{||}$ show a strong dependence on $k_\perp$ (see Fig. 9a and 9c). For not too high n_b, the beam particle distribution contribute much more to the imaginary part of the ε_{11} dielectric tensor element, which is very small for nearly undamped ion Bernstein

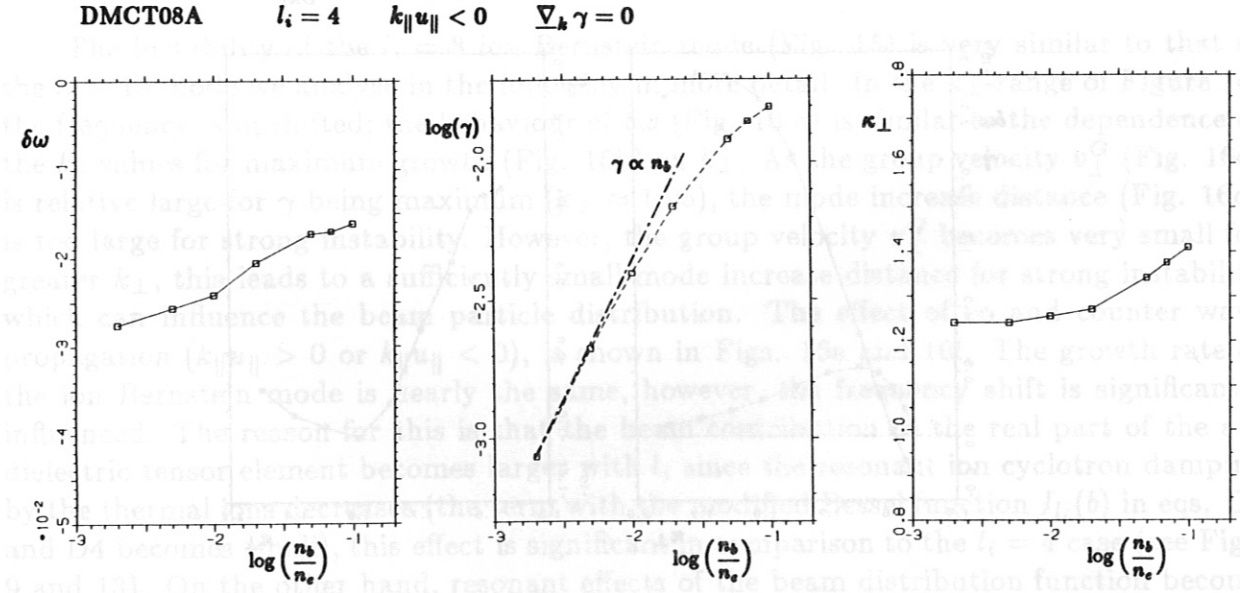

Fig. 13 *Ion cyclotron instability (harmonic $l_i = 4$) driven by the transient distribution* DMCT08A: *$\delta\omega$ and $\log(\gamma)$ (on the left and in the middle) versus $\log(n_b/n_e)$ for γ being maximum with respect to both $\kappa_\perp$ (on the right) and $\kappa_{||}$ (~ -0.01). Plasma parameter: $B_0 = 3.2\ T$, $T_e = 400\ eV$, $T_i = 400\ eV$, $n_e = 5 \cdot 10^{13}\ cm^{-3}$*

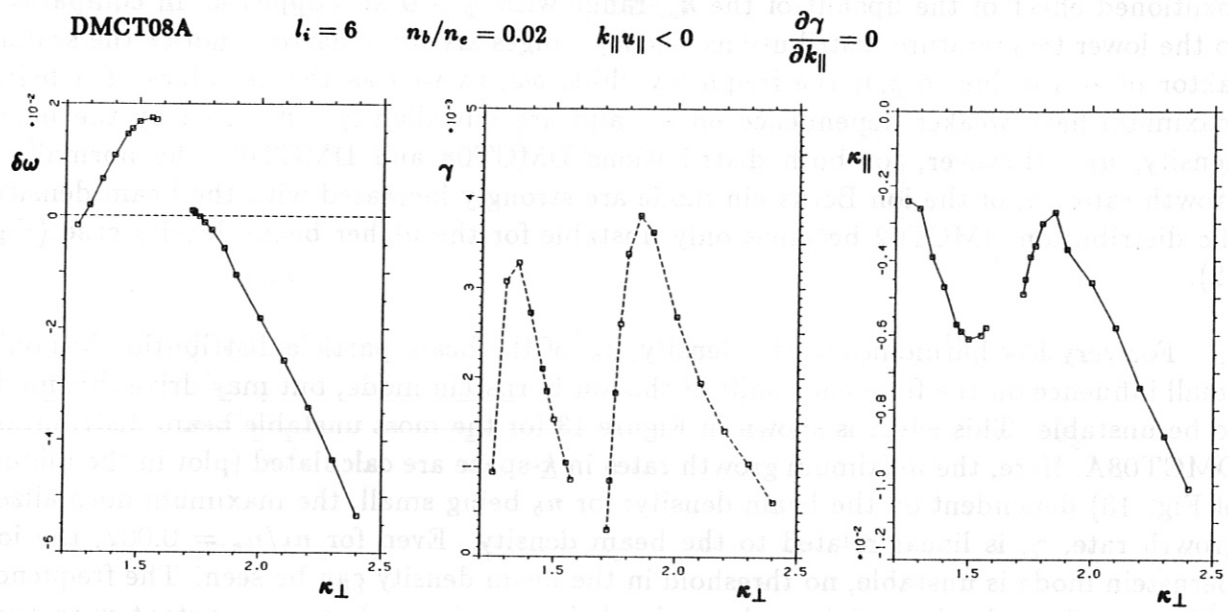

Fig. 14 *Ion cyclotron instability (harmonic $l_i = 6$) driven by the transient distribution* DMCT08A: *$\delta\omega$ and γ (on the left and in the middle) versus $\kappa_\perp$ for γ being maximum with respect to $\kappa_\parallel$ (on the right).*
Plasma parameter: $B_0 = 3.2\ T$, $T_e = 400\ eV$, $T_i = 400\ eV$, $n_e = 5 \cdot 10^{13}\ cm^{-3}$

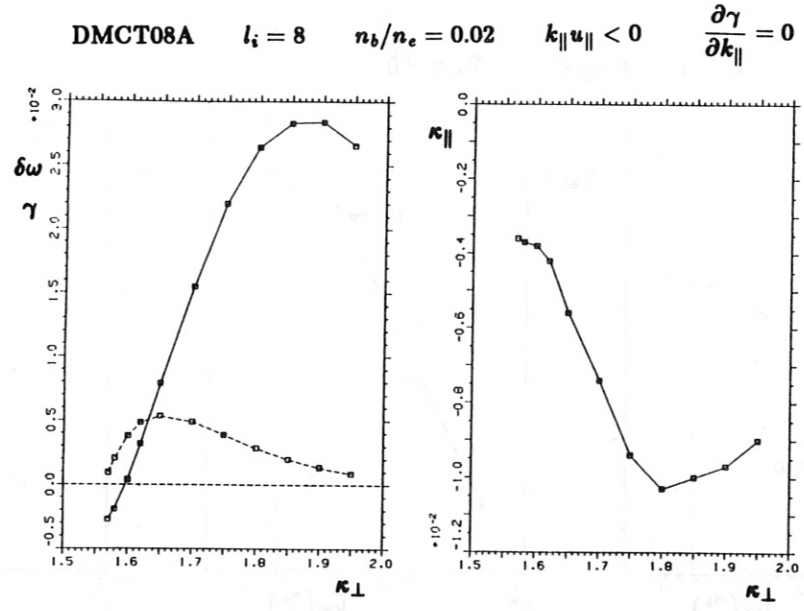

Fig. 15 *Ion cyclotron instability (harmonic $l_i = 8$) driven by the transient distribution* DMCT08A: *$\delta\omega$ (on the left, solid line) and γ (broken line) versus $\kappa_\perp$ for γ being maximum with respect to $\kappa_\parallel$ (on the right).*
Plasma parameter: $B_0 = 3.2\ T$, $T_e = 400\ eV$, $T_i = 400\ eV$, $n_e = 5 \cdot 10^{13}\ cm^{-3}$

modes in a pure Maxwellian plasma, than to the the real part of ε_{11} that mainly determines the frequency shift depending on $k_{\|}$ and $k_{\perp}$ (see Appendix D). For higher harmonics l_i, however, the plasma ion contribution to the real part of the resonant terms in ε_{11} become small and the frequency shift is stronger influenced by the beam particle distribution.

In the following, we compare the instabilities of the distribution DMCT08A for the different ion cyclotron harmonics (Figs. 9, 14, 15 and 16). Both the dispersion relation of the ion Bernstein modes and the $k_{\perp}$-resonance with the domains in the distributions with $\partial f_b/\partial v_{\perp} > 0$ depend on the harmonic number l_i. These effects may be demonstated in Figure 14 for the harmonic $l_i = 6$. For small $k_{\perp}$ in Fig. 14 related to the first maximum in γ, the frequency shift of the ion Bernstein mode is positive, the instability is mainly driven by the peak in the distribution function close to the 27 keV injection energy. For larger $k_{\perp}$ related to the second maximum, $\delta\omega$ becomes negative and the 9 keV peak mainly drives the instability. Within this range, however, the peaks are not in resonance and result in the relative small growth rate. The range with larger $k_{\perp}$ corresponds to the $l_i = 4$ case (Fig. 9), the range with smaller $k_{\perp}$ to the cases with $l_i = 8$ (Fig. 15) and $l_i = 10$ (Fig. 16) where the $k_{\perp}$-ranges are much smaller than for $l_i = 6$. For the low harmonics, however, the $k_{\perp}$-resonances related to the domains of the distribution functions which drive the instability, are not very sharp. The condition for this resonance is connected with the convolution of the Bessel function product $J_{l_b}(a) \cdot J'_{l_b}(a)$ with $a = k_{\perp}u_{\perp}/\omega_{ci}$ (see eqs. C3 and C4). Since $k_{\perp}$ increase with the order, l_b, and the periodicity of the Bessel functions is nearly constant, the resolution in $u_{\perp}$ is increased leading to smaller domains in $u_{\perp}$ being resonant. Consequently, the gradient region of the distribution functions can drive instability more effective for higher harmonic numbers (see Chapter IV).

The instability of the $l_i = 8$ ion Bernstein mode (Fig. 15) is very similar to that of the $l_i = 10$ mode we analyse in the following in more detail. In the $k_{\perp}$-range of Figure 16, the frequency is upshifted; the behaviour of $\delta\omega$ (Fig. 16 a) is similar to the dependence of the $k_{\|}$ values for maximum growth (Fig. 16b) on $k_{\perp}$. As the group velocity $v_{\perp}^{G}$ (Fig. 16c) is relative large for γ being maximum ($\kappa_{\perp} \approx 1.95$), the mode increase distance (Fig. 16d) is too large for strong instability. However, the group velocity $v_{\perp}^{G}$ becomes very small for greater $k_{\perp}$, this leads to a sufficiently small mode increase distance for strong instability which can influence the beam particle distribution. The effect of co and counter wave propagation ($k_{\|}u_{\|} > 0$ or $k_{\|}u_{\|} < 0$), is shown in Figs. 16e and 16f. The growth rate of the ion Bernstein mode is nearly the same, however, the frequency shift is significantly influenced. The reason for this is that the beam contribution to the real part of the ε_{11} dielectric tensor element becomes larger with l_i since the resonant ion cyclotron damping by the thermal ions decreases (the term with the modified Bessel function $I_{l_i}(b)$ in eqs. D2 and D4 becomes small), this effect is significant in comparison to the $l_i = 4$ case (see Figs. 9 and 13). On the other hand, resonant effects of the beam distribution function become more important for the damping. The stationary slowing down distribution functions of the beam particles are much broader in velocity space; the damping can overcome the driving of instabilities related to the domains close to the injection peaks for the low harmonics.

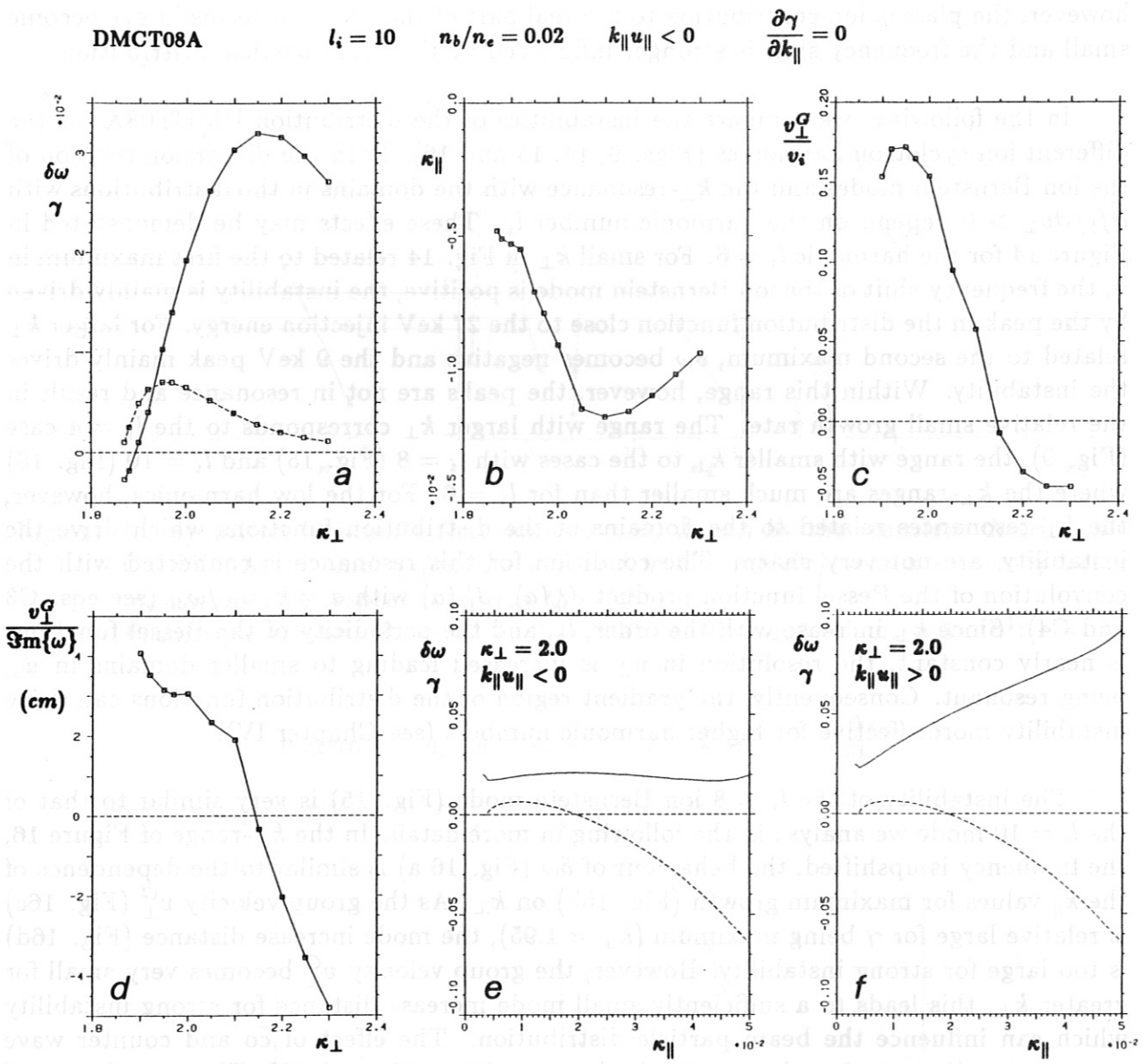

Fig. 16 *Ion cyclotron instability (harmonic $l_i = 10$) driven by the transient distribution* DMCT08A: *$\delta\omega$ (solid line) and γ (broken line in Fig. 16a) versus $\kappa_\perp$ for γ being maximum with respect to $\kappa_\parallel$ (Fig. 16b). In Figs. 16c and 16d, the normalized group velocity v_i^G/v_i and the mode increase distance, $v_\perp^G/\Im m\{\omega\}$, are plotted. Figures 16e and 16f show $\delta\omega$ (solid lines) and γ (broken lines) versus $\kappa_\parallel$ for fixed $k_\perp$ for counter ($k_\parallel u_\parallel < 0$) and for co ($k_\parallel u_\parallel > 0$) wave propagation with respect to the neutral beam injection.*
Plasma parameter: $B_0 = 3.2\ T$, $T_e = 400\ eV$, $T_i = 400\ eV$, $n_e = 5 \cdot 10^{13}\ cm^{-3}$

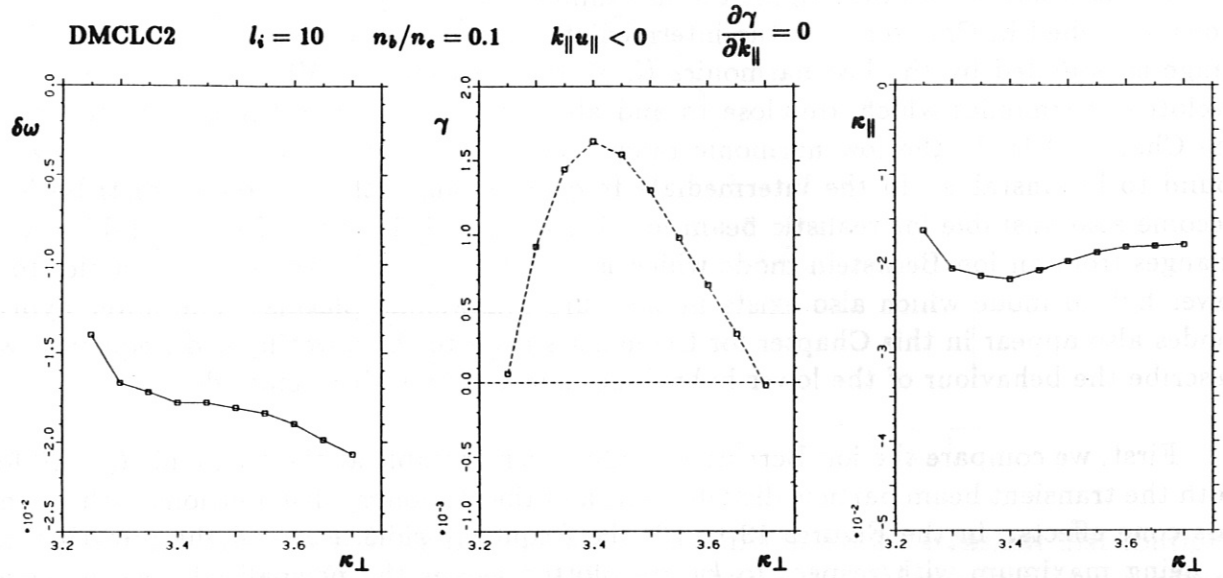

Fig. 17 *Ion cyclotron instability (harmonic $l_i = 10$) driven by the stationary distribution with loss cone* DMCLC2: *$\delta\omega$ (on the left, solid line) and γ (broken line) versus $\kappa_\perp$ for γ being maximum with respect to $\kappa_\parallel$ (on the right).*
Plasma parameter: $B_0 = 3.2\ T$, $T_e = 600\ eV$, $T_i = 1000\ eV$, $n_e = 5 \cdot 10^{13}\ cm^{-3}$

For the harmonic $l_i = 10$, the stationary beam particle distribution DMCLC2 with very strong loss cone effects becomes unstable (see Fig 17), the growth rates for realistic beam densities ($n_b/n_e \simeq 0.1$), however, are much smaller than in the case of the transient beam particle distributions. For lower harmonics as well as for co wave propagation, the distribution DMCLC2 is stable. Furthermore, the distribution DMCLC1 with less pronounced loss cone is also stable for co and counter wave propagation at the harmonic $l_i = 10$. The $k_\perp$ range in Fig. 17 with γ being maximum with respect to $k_\parallel$ corresponds to the range of Fig. 16, the behaviour of the ion Bernstein mode is different for both beam particle distributions. The resonant terms of ε_{11}^b are related to anlogous domains in the distributions with $\partial f_b/\partial v_\perp > 0$. In the nonresonant terms, however, the influence of the rest of the distribution function on the frequency shift and on the $k_\parallel$ dependence (comp. Fig. 16a and 16b) is quite different. In both cases, the contribution of the thermal ions to the ε_{11} element is of less importance and the ion Bernstein mode is mainly driven by the beam particle distribution.

V. Instabilities in the Intermediate Harmonic Range

In this Chapter, we investigate the instabilities driven by the beam particle distributions described in Chapter II in the intermediate range of ion cyclotron harmonics. This range is bounded by the low harmonics ($l_i \leq 10$, see Chapter IV) and by the high ion cyclotron harmonics which are close to and above the lower hybrid frequency ($l_i \geq 40$, see Chapter VI). In the low harmonic range, the transient beam ion distributions were found to be unstable. In the intermediate frequency range, the stationary distributions become also unstable for realistic beam ion densities, and the type of the unstable mode changes from an ion Bernstein mode which is mainly defined by the beam particles to a lower hybrid mode which also exists in the pure Maxwellian plasma. The lower hybrid modes also appear in this Chapter for frequencies close to the lower hybrid frequency; we describe the behaviour of the lower hybrid mode in Chapter VI in more detail.

First, we compare the ion Bernstein mode being unstable at the harmonic $l_i = 20$ for both the transient beam particle distributions and the stationary distributions with strong loss cone effects. In the Figures 18 to 22, the frequency shift, $\delta\omega$, and the growth rate, γ, being maximum with respect to $k_\parallel$ are plotted versus the normalized perpendicular wave number, $\kappa_\perp$. Contrary to the low harmonic case ($l_i = 4$, Figures 9 to 12), the form of the beam particle distribution function determines the behaviour of the unstable ion Bernstein mode, the temperatures of the thermal plasma component are of minor importance. The beam particle distributions at $t = \tau_{SD}/8$ after switch on the neutral beam injection (DMCT08A and DMCT08) as well as the distributions at $t = \tau_{SD}/2$ (DMCT02A and DMCT02) result in ion Bernstein modes which are very similar, respectively; especially the growth rates, γ, are nearly independent on the temperatures of the thermal plasma component (note the scaling factor of ~ 1.6 in $\kappa_\perp$ due to ρ_i).

In the following, we discuss shortly the $k_\perp$ dependence of the instabilities with a resonant character for l_i being fixed. The domains of the beam particle distribution function with $\partial f_b/\partial v_\perp > 0$ drive the ion cyclotron instability. In the $\underline{v}$-space convolution with the $\delta\delta$-function (eqs. 4 and 5), the perpendicular derivative of f_b leads to the derivative $J_{l_b}(a)\, J'_{l_b}(a)$ in the ε^b_{11} element of the dielectric tensor (comp. Appendix C, eqs. C3 and C4). For l_b sufficiently high, the argument $a = k_\perp u_\perp/\omega_{cb}$ is related to the different peaks in the distribution function, f_b, close to the injection energies. Since the minima of the expression $J_{l_b}(a)\, J'_{l_b}(a)$ result in maximum instability, the domains $v_\perp$ close to the peaks with $\partial f_b/\partial v_\perp > 0$ are related to ranges in $k_\perp$ for which maximum instabilty is found. As the Bessel functions $J_{l_b}(a)$ are periodic with respect to a, we may define harmonics in $k_\perp$ for fixed $v_\perp$ related to the single peaks in the beam particle distribution function. The broadness of these resonant ranges in $k_\perp$ depends on both the harmonic number l_b and the broadness of the domains in $v_\perp$ with $\partial f_b/\partial v_\perp > 0$. For the intermediate and high ion cyclotron harmonics, we can separate the low $k_\perp$-harmonics for the single peaks. However, the peak with half injection energy (13.5 keV) is less pronounced and close to the 9 keV peak; instabilities related only to this peak are overlapped by the higher harmonics of the 27 keV peak.

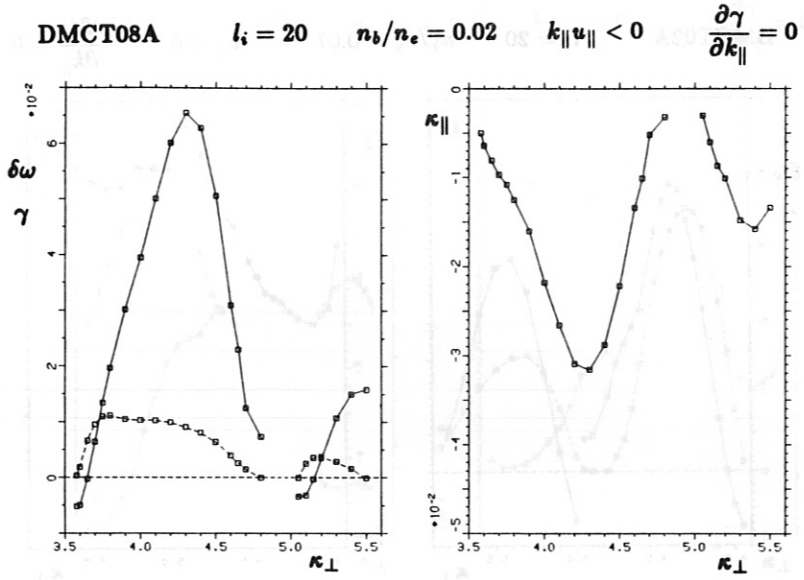

Fig. 18 *Ion cyclotron instability (harmonic $l_i = 20$) driven by the transient distribution* DMCT08A: *$\delta\omega$ (solid line) and γ (broken line on the left) versus $\kappa_\perp$ for γ being maximum with respect to $\kappa_\parallel$ (on the right).*
Plasma parameter: $B_0 = 3.2\ T$, $T_e = 400\ eV$, $T_i = 400\ eV$, $n_e = 5 \cdot 10^{13}\ cm^{-3}$

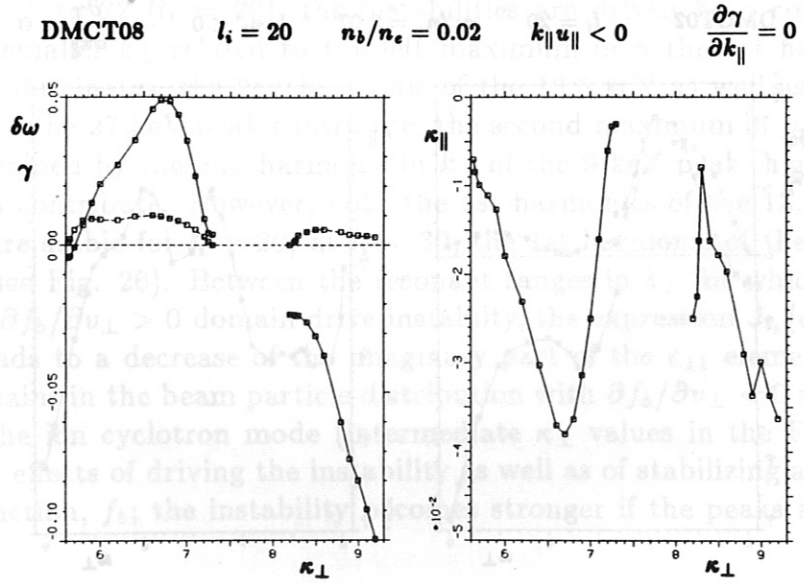

Fig. 19 *Ion cyclotron instability (harmonic $l_i = 20$) driven by the transient distribution* DMCT08: *$\delta\omega$ (solid line) and γ (broken line on the left) versus $\kappa_\perp$ for γ being maximum with respect to $\kappa_\parallel$ (on the right).*
Plasma parameter: $B_0 = 3.2\ T$, $T_e = 600\ eV$, $T_i = 1000\ eV$, $n_e = 5 \cdot 10^{13}\ cm^{-3}$

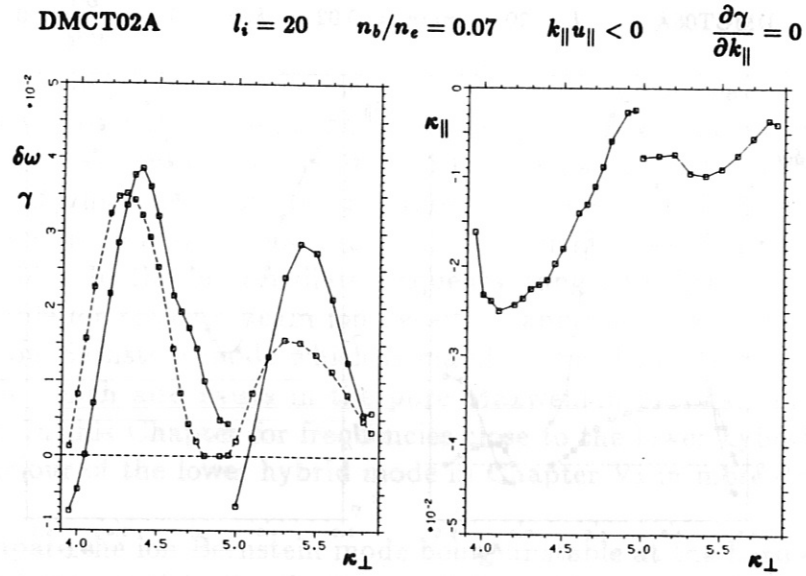

Fig. 20 *Ion cyclotron instability (harmonic $l_i = 20$) driven by the transient distribution* DMCT02A: *$\delta\omega$ (solid line) and γ (broken line on the left) versus $\kappa_\perp$ for γ being maximum with respect to $\kappa_\parallel$ (on the right).*
Plasma parameter: $B_0 = 3.2\ T$, $T_e = 400\ eV$, $T_i = 400\ eV$, $n_e = 5 \cdot 10^{13}\ cm^{-3}$

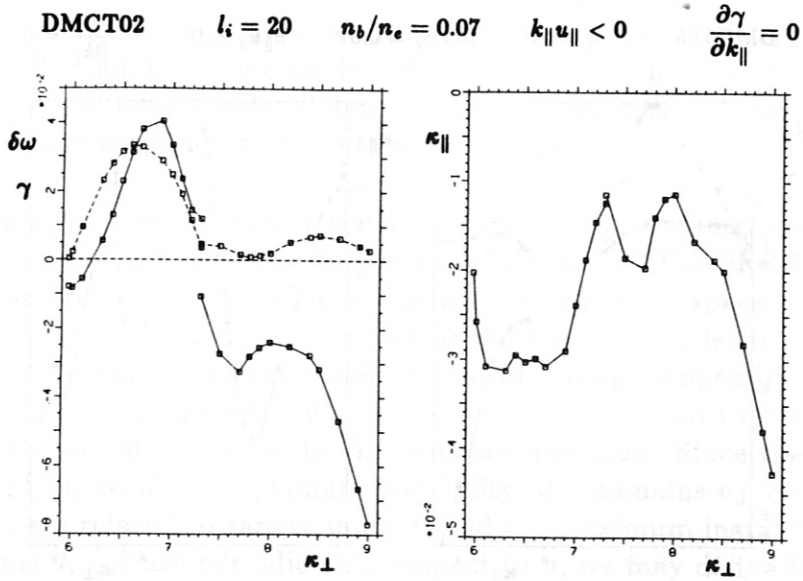

Fig. 21 *Ion cyclotron instability (harmonic $l_i = 20$) driven by the transient distribution* DMCT02: *$\delta\omega$ (solid line) and γ (broken line on the left) versus $\kappa_\perp$ for γ being maximum with respect to $\kappa_\parallel$ (on the right).*
Plasma parameter: $B_0 = 3.2\ T$, $T_e = 600\ eV$, $T_i = 1000\ eV$, $n_e = 5 \cdot 10^{13}\ cm^{-3}$

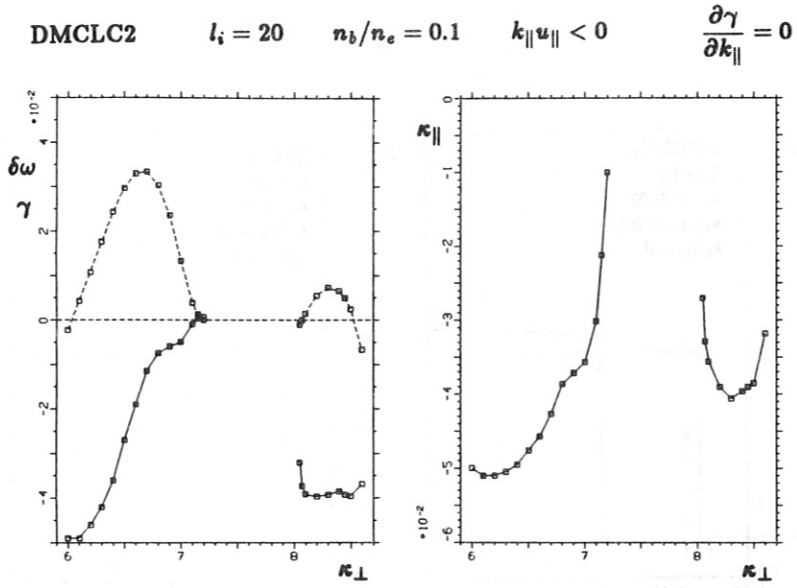

Fig. 22 *Ion cyclotron instability (harmonic $l_i = 20$) driven by the stationary distribution with loss cone* DMCLC2: *$\delta\omega$ (solid line) and γ (broken line on the left) versus $\kappa_\perp$ for γ being maximum with respect to $\kappa_\parallel$ (on the right).*
Plasma parameter: $B_0 = 3.2\ T$, $T_e = 600\ eV$, $T_i = 1000\ eV$, $n_e = 5 \cdot 10^{13}\ cm^{-3}$

In Figures 18 to 22 ($l_i = 20$), the instabilities are driven by a combination of the peaks: for the smaller $k_\perp$ related to the left maximum in γ the 1st harmonic in $k_\perp$ of the 9 keV peak dominates, the 2nd harmonic of the 13.5 keV as well as the 3rd and the 4th harmonics of the 27 keV peak contribute; the second maximum in γ at the higher $k_\perp$ is mainly determined by the 2nd harmonic in $k_\perp$ of the 9 keV peak, higher harmonics of the other peaks contribute. However, both the 1st harmonics of the 13.5 keV and of the 27 keV peaks are stable for $l_i = 20$; at $l_i = 30$, the 1st harmonic of the 27 keV peaks is also unstable (see Fig. 26). Between the resonant ranges in $k_\perp$ for which beam particles with $v_\perp$ of the $\partial f_b/\partial v_\perp > 0$ domain drive instabilty, the expression $J_{l_b}(a)\, J'_{l_b}(a)$ becomes positive and leads to a decrease of the imaginary part of the ε_{11} element. For these $k_\perp$ values, the domains in the beam particle distribution with $\partial f_b/\partial v_\perp < 0$ are dominant and may stabilize the ion cyclotron mode (intermediate $\kappa_\perp$ values in the Figures 18 to 22). Generally, both effects of driving the instability as well as of stabilizing appear for the full distribution function, f_b; the instability becomes stronger if the peaks are in phase with respect to $k_\perp$.

The 5 beam particle distribution functions in Figures 18 to 22 (DMCT08A, DMCT08, DMCT02A, DMCT02 and DMCLC2) drive strong instabilty at the harmonic $l_i = 20$. In all cases, $\kappa_\perp$ values exist for which the perpendicular group velocity, $v_\perp^G$, and the mode increase distance are sufficiently small to result in strong electric fields of the mode being unstable; the domains in $\underline{k}$-space, however, are relatively small. Consequently, these beam particle distributions will be strongly affected by the instabilities in this frequency range.

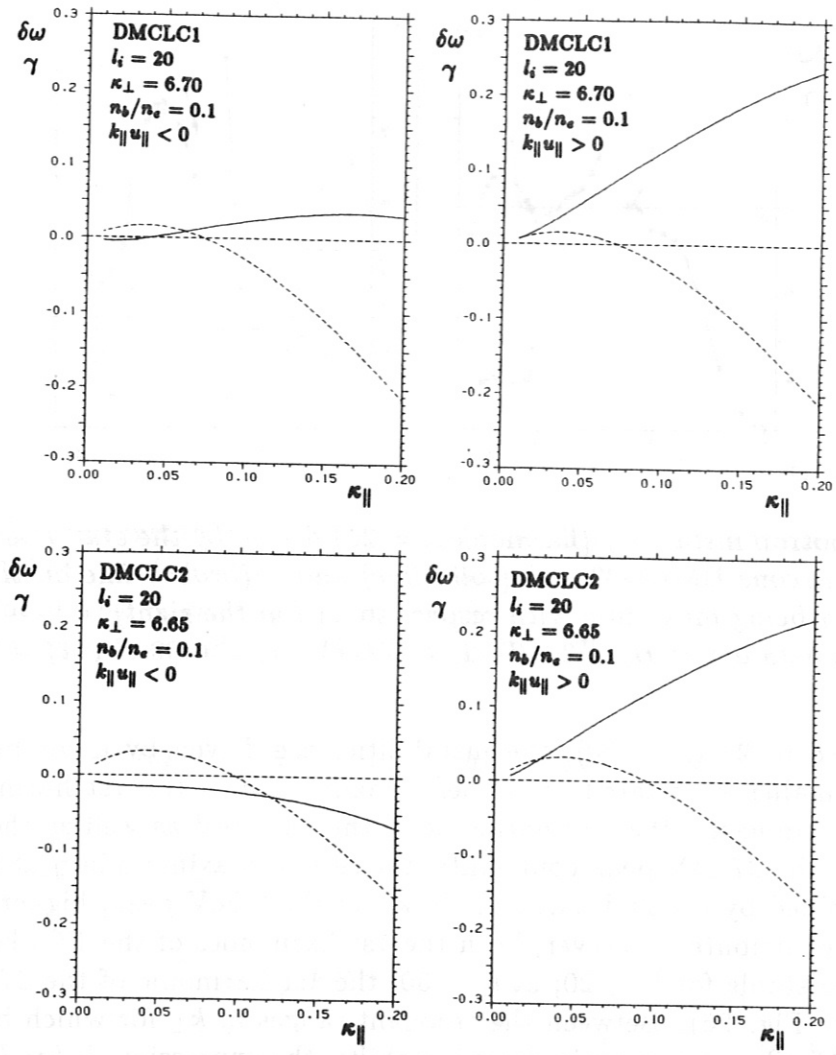

Fig. 23 *Comparison of ion cyclotron instabilities (harmonic $l_i = 20$) driven by the stationary distributions with loss cone* DMCLC1 *(upper plots) and* DMCLC2 *(lower plots): $\delta\omega$ (solid line) and γ (broken line) versus $\kappa_\parallel$ for counter (on the left) and co wave propagation (on the right). The $k_\perp$ values are estimated to get a maximum growth rate, γ, the difference in $k_\perp$, however, is relative small (comp. Fig. 22).*

Plasma parameter: $B_0 = 3.2\ T,\ T_e = 600\ eV,\ T_i = 1000\ eV,\ n_e = 5 \cdot 10^{13}\ cm^{-3}$

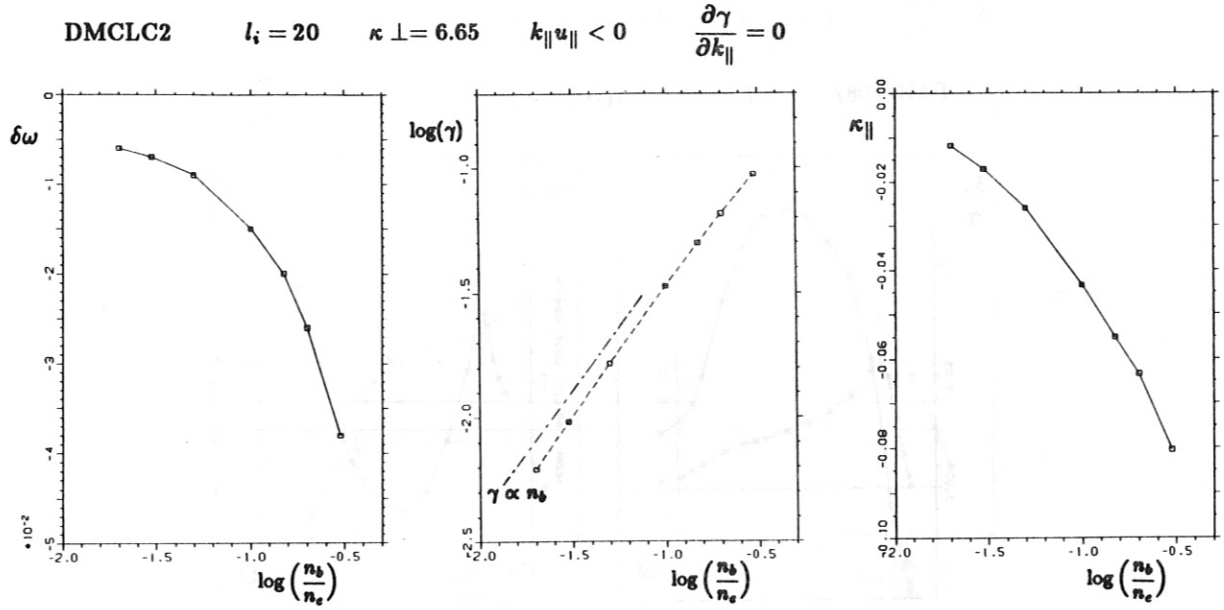

Fig. 24 *Ion cyclotron instability (harmonic $l_i = 20$) driven by the stationary distribution with loss cone* DMCLC2: *$\delta\omega$ (on the left) and $\log(\gamma)$ (in the middle) versus $\log(n_b/n_e)$ with $\kappa_\perp$ fixed for γ being maximum with respect to $\kappa_\parallel$ (on the right). Plasma parameter: $B_0 = 3.2\ T$, $T_e = 600\ eV$, $T_i = 1000\ eV$, $n_e = 5 \cdot 10^{13}\ cm^{-3}$*

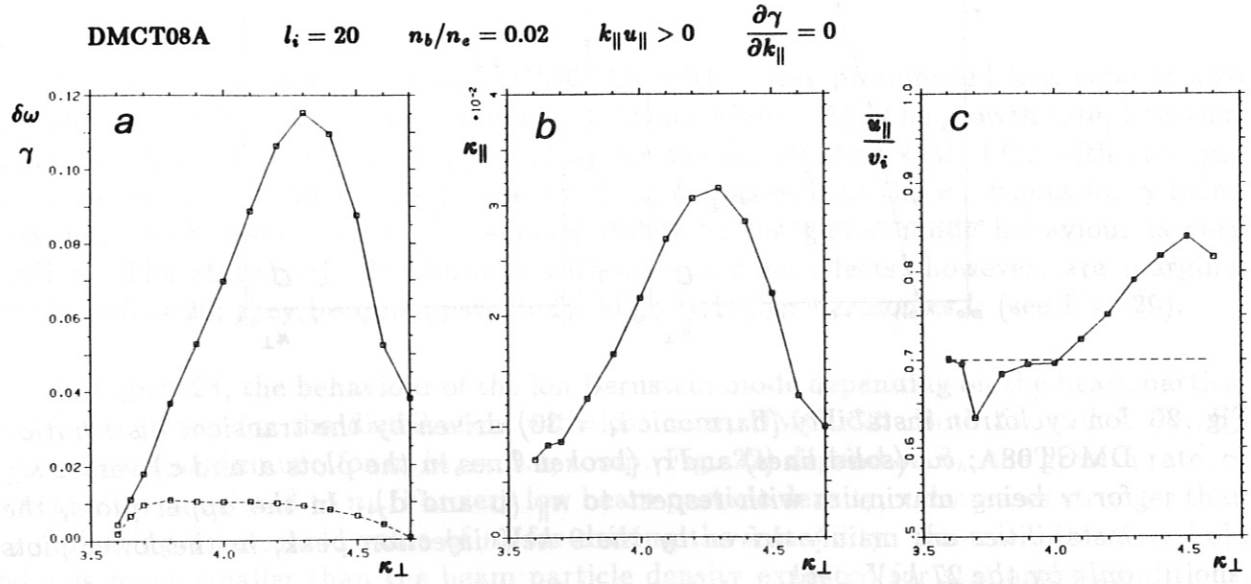

Fig. 25 *Ion cyclotron instability (harmonic $l_i = 20$) driven by the transient distribution* DMCT08A *for co wave propagation, $k_\parallel u_\parallel > 0$: $\delta\omega$ (solid line) and γ (broken line in* a*) versus $\kappa_\perp$ for γ being maximum with respect to $\kappa_\parallel$ (*b*). $\bar{u}_\parallel/v_i$ (*c*) is estimated from the frequency shift, $\delta\omega^{\pm}$, for co and counter wave propagation (solid line, see text), the broken line corresponds to the average parallel injection velocity, $u_\parallel$, of the 9 keV ions.*
Plasma parameter: $B_0 = 3.2\ T$, $T_e = 400\ eV$, $T_i = 400\ eV$, $n_e = 5 \cdot 10^{13}\ cm^{-3}$

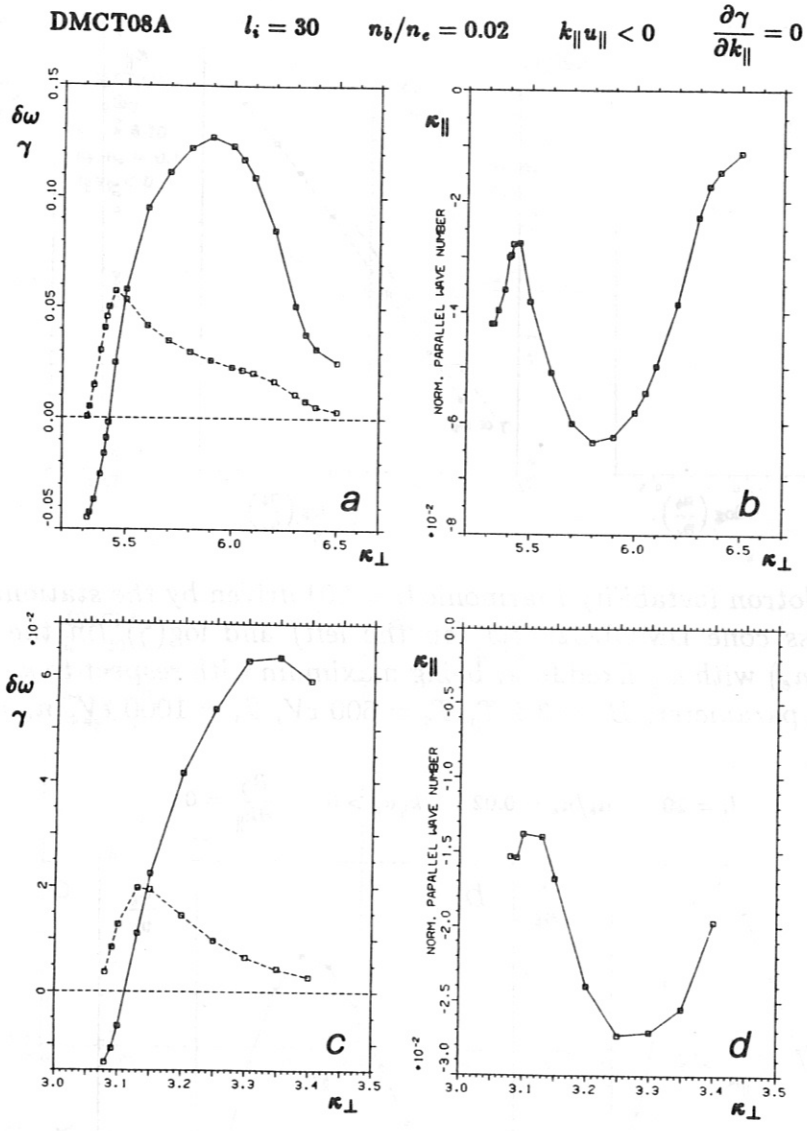

Fig. 26 *Ion cyclotron instability (harmonic $l_i = 30$) driven by the transient distribution* DMCT08A: *$\delta\omega$ (solid lines) and γ (broken lines in the plots* **a** *and* **c**) *versus $\kappa_\perp$ for γ being maximum with respect to $\kappa_\parallel$ (***b** *and* **d**). *In the upper plots, the instabilities are mainly driven by the 9 keV injection peak, in the lower plots only by the 27 keV peak.*
Plasma parameter: $B_0 = 3.2\ T$, $T_e = 400\ eV$, $T_i = 400\ eV$, $n_e = 5 \cdot 10^{13}\ cm^{-3}$

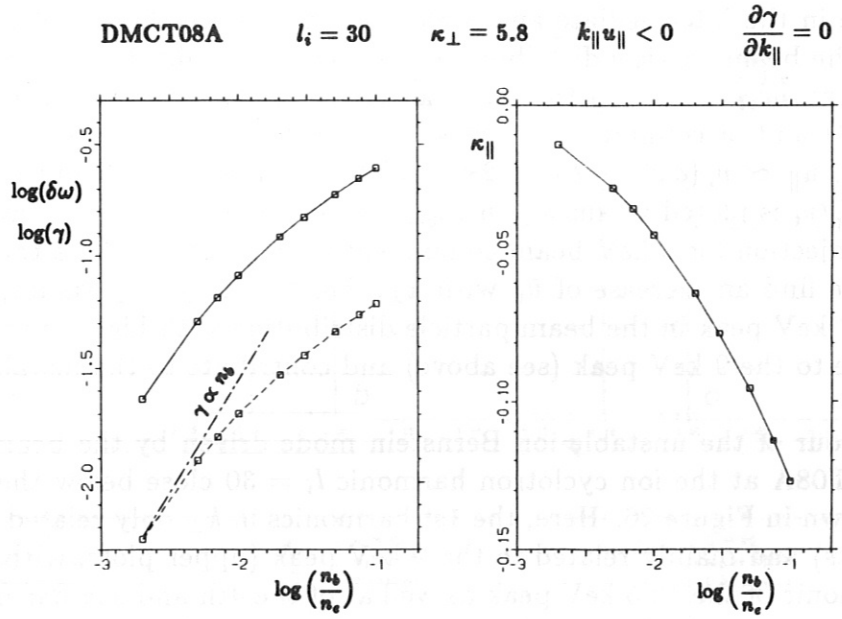

Fig. 27 *Ion cyclotron instability (harmonic $l_i = 30$) driven by the transient distribution* DMCT08A: $\log(\delta\omega)$ *(solid line) and* $\log(\gamma)$ *(broken line on the left) versus* $\log(n_b/n_e)$ *with* $\kappa_\perp$ *fixed (corresponding to the 9 keV peak) for* γ *being maximum with respect to* $\kappa_\|$ *(on the right).*
Plasma parameter: $B_0 = 3.2\ T$, $T_e = 400\ eV$, $T_i = 400\ eV$, $n_e = 5 \cdot 10^{13}\ cm^{-3}$

The beam particle distribution DMCLC1 with a less pronounced loss cone is also unstable for the ion cyclotron harmonic $l_i = 20$ (see Figure 23). The growth rate, however, is smaller than the corresponding γ values for the distribution DMCLC2 with stronger loss cone effects. Although the frequency shift, $\delta\omega$, as well as the $k_\perp$ values for γ being maximum with respect to $k_\|$ are slightly different, the global mode behaviour is very similar. The stationary distributions without loss cone effects, however, are marginal stable at $l_i = 20$; they become unstable for slightly higher harmonics l_i (see Fig. 29).

In Figure 24, the behaviour of the ion Bernstein mode depending on the beam particle density is shown for the distribution with loss cone, DMCLC2. Both $\delta\omega$ and $k_\|$ for $k_\perp$ being fixed (maximum γ for $n_b/n_e = 0.1$, comp. Fig. 22) depend on n_b; the growth rate, γ, is nearly linear related to n_b. For very low beam particle density, γ decreases stronger than n_b indicating a threshold value of n_b for driving the instability. However, this threshold value is much smaller than the beam particle density expected for stationary conditions. Furthermore, in connection to the experimental conditions, the threshold value of n_b related to the mode increase distance being sufficiently small is of much more importance.

In Figure 25, the instabilities at $l_i = 20$ driven by the distribution DMCT08A for co wave propagation, $k_\| u_\| > 0$, are shown. In comparison to the case of counter wave propagation (see Fig. 18), the frequency shift, $\delta\omega$, is significantly increased, the growth rate, γ, is unchanged. Furthermore, the absolute $k_\|$ values for which γ is maximum are nearly

the same. Since in the intermediate and high frequency range the ε_{11} element is mainly determined by the beam particle distribution, the frequency shift depends significantly on the condition $\omega \approx l_b\omega_{cb} + k_{||}u_{||}$ in the resonant terms of ε_{11}^b. By means of the frequency shift of co ($\delta\omega^+$) and of counter ($\delta\omega^-$) wave propagation, we can estimate the average parallel velocity, $\overline{u}_{||} \simeq v_i\,(\delta\omega^+ - \delta\omega^-)/2\kappa_{||}$ which is related to γ being maximum with respect to $k_{||}$; $\overline{u}_{||}/v_i$ is ploted versus $\kappa_\perp$ in Fig. 25c. In comparison to the average parallel velocity of the injection for 9 keV beam component which mainly drives the instability in this example, we find an increase of $\overline{u}_{||}$ with $k_\perp$. For the larger $k_\perp$ values, the 13.5 keV as well as the 27 keV peak in the beam particle distribution with higher parallel velocities become in phase to the 9 keV peak (see above) and contribute to the instability.

The behaviour of the unstable ion Bernstein mode driven by the beam particle distribution DMCT08A at the ion cyclotron harmonic $l_i = 30$ close below the lower hybrid frequency is shown in Figure 26. Here, the 1st harmonics in $k_\perp$ only related to the 27 keV peak (lower plots) and mainly related to the 9 keV peak (upper plots, with contributions of the 2nd harmonic of the 13.5 keV peak as well as of the 4th and 5th harmonic of the 27 keV peak) are strongly unstable. For both cases, the growth distances can be sufficiently small depending on $k_{||}$ and $k_\perp$. The behaviour of this unstable ion Bernstein mode is quite similar to the $l_i = 20$ harmonic case (Fig. 18) described above. The dependence on the beam particle density is shown in Figure 27 for $k_\perp$ being fixed; the dependence of γ on n_b is similar to the cases of lower harmonics ($l_i = 4$ in Fig. 13 and $l_i = 20$ in Fig. 24). Also the frequency shift as well as the $k_{||}$ values for γ being maximum are strongly influenced by the beam particle density.

Finally, we discuss the instabilities driven by the stationary beam particle distribution without loss cone, DMC327, in the vicinity of the lower hybrid frequency ($l_i \sim 35$ for this case). In Figure 28, the frequency shift, $\delta\omega$, and the growth rate, γ, are ploted versus the normalized parallel wave number, $\kappa_{||}$, for different harmonics l_i with $k_\perp$ estimated for γ being maximum. In the plots **a** to **f**, the instability is mainly driven by the 9 keV peak, in the plots **g** to **i** only by the 27 keV peak in the beam particle distribution. For $l_i \leq 32$, no instability driven by the 27 keV peak was found (see Fig. 29); for $l_i \geq 40$, we find very strong instability connected with the lower hybrid mode. The maximum growth rates with respect to both $k_{||}$ and $k_\perp$ in Figure 29 depend on $k_{||}$ much stronger close and above the lower hybrid frequency than for the lower harmonics l_i with the ion Bernstein mode being unstable. The lower hybrid mode has strong growth rates in a $k_{||}$ range which becomes more narrow if the beam density is decreased. The dependence of the lower hybrid mode ($l_i = 40$ in Figure 30) on the beam particle density is quite different to the case of the ion Bernstein mode ($l_i = 34$) which indicates a threshold in the beam particle density for driving the instability. The unstable ion Bernstein mode driven by the stationary distribution DMC327 is similar to those driven by the transient beam particle distributions as well as by the stationary distributions with strong loss cone; the main difference is the much smaller growth rate for realistic beam particle density ($n_b/n_e = 0.1$ in the Figs. 28 and 30). In Chapter VI, we will discuss the lower hybrid mode in more detail; therefore, we will return to the mode behaviour close to the lower hybrid frequency.

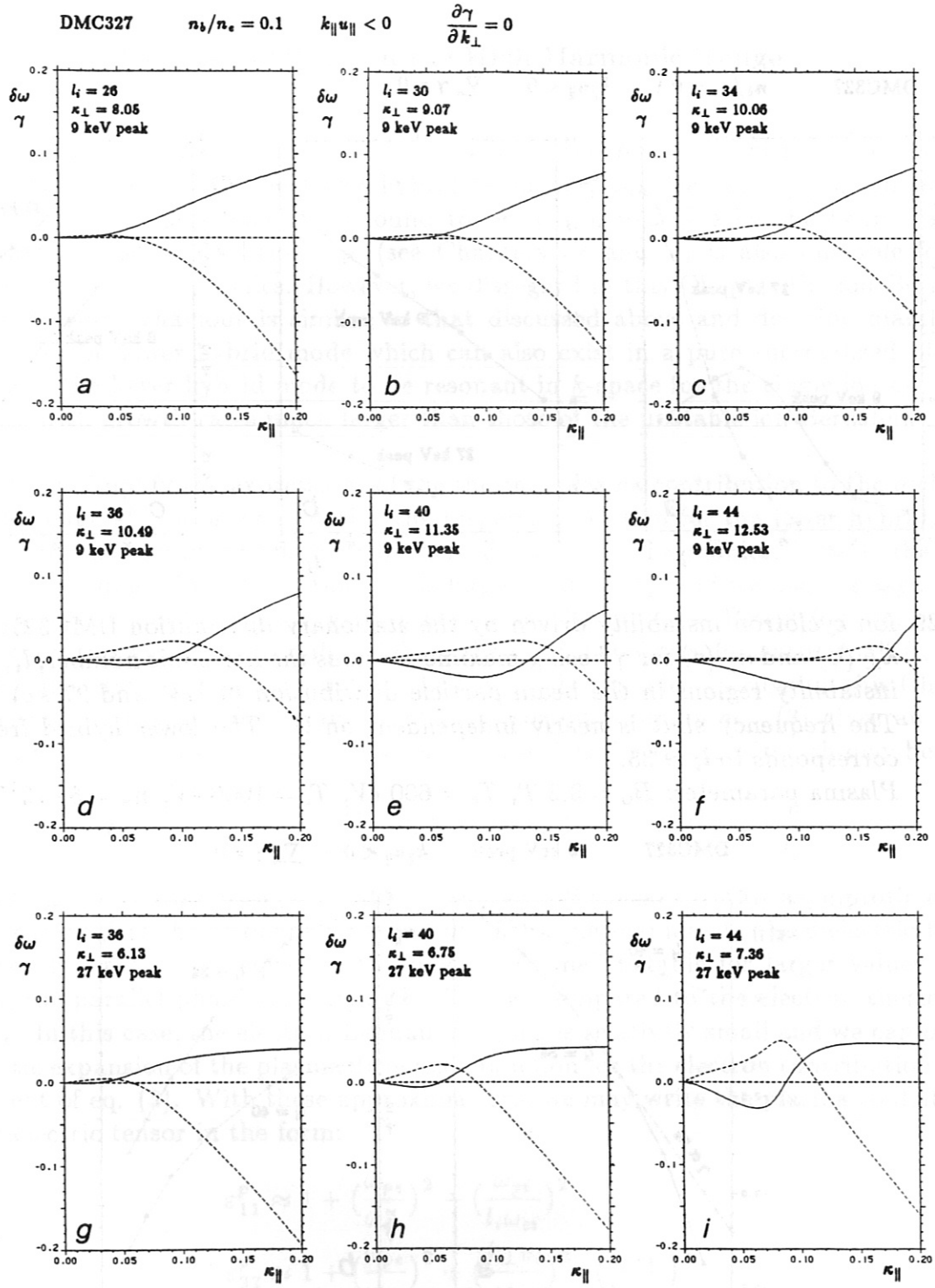

Fig. 28 *Ion cyclotron instabilities driven by the stationary distribution* DMC327: $\delta\omega$ *(solid lines) and* γ *(broken lines) versus* $\kappa_\parallel$ *with* $\kappa_\perp$ *estimated to get maximum growth rates,* γ*, for the different harmonics,* l_i *(comp. Fig. 29). The instability in the plots* **a** *to* **f** *is mainly driven by the* 9 *keV injection peak, in the plots* **g** *to* **i** *only by the* 27 *keV peak.*
Plasma parameter: $B_0 = 3.2\ T$, $T_e = 600\ eV$, $T_i = 1000\ eV$, $n_e = 5 \cdot 10^{13}\ cm^{-3}$

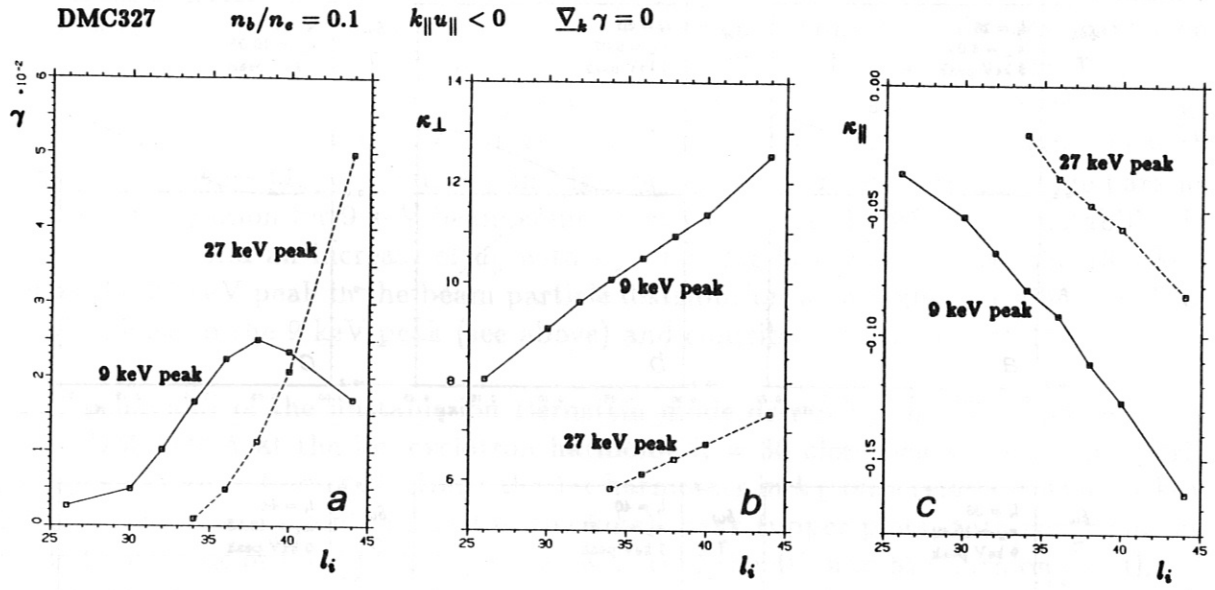

Fig. 29 *Ion cyclotron instability driven by the stationary distribution* DMC327: γ (a), $\kappa_\perp$ (b) *and* $\kappa_\parallel$ (c) *for* γ *beeing maximum versus the harmonic number,* l_i, *for two instability regions in the beam particle distribution (9 keV and 27 keV peak). The frequency shift is nearly independent on* l_i. *The lower hybrid frequency corresponds to* $l_i \simeq 35$.
Plasma parameter: $B_0 = 3.2\ T$, $T_e = 600\ eV$, $T_i = 1000\ eV$, $n_e = 5 \cdot 10^{13}\ cm^{-3}$

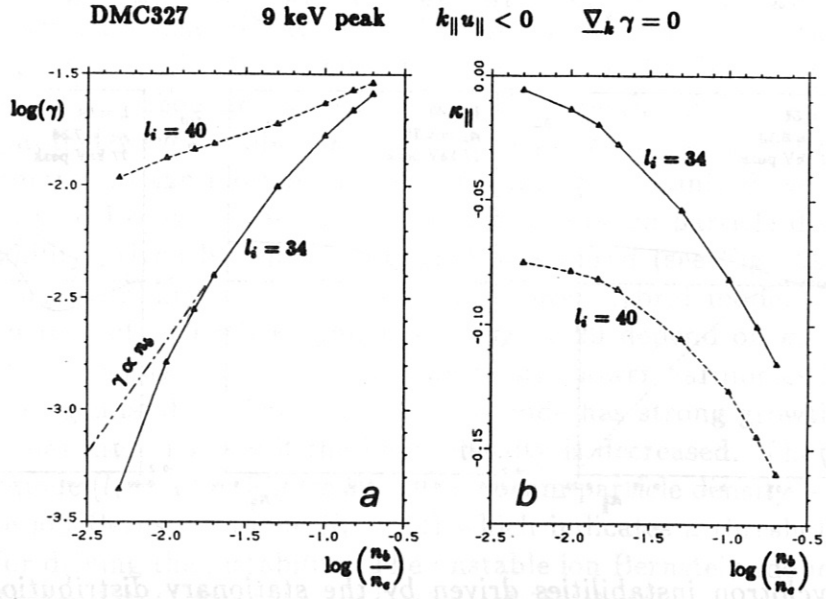

Fig. 30 *Ion cyclotron instability driven by the stationary distribution* DMC327: log(γ) (a) *and* $\kappa_\parallel$ (b) *for* γ *beeing maximum versus* $\log(n_b/n_e)$ *for the harmonics* $l_i = 34$ *and* $l_i = 40$. *Both* $\kappa_\perp$ *and the frequency shift are nearly independent on the beam density. The instability is mainly driven by the 9 keV peak.*
Plasma parameter: $B_0 = 3.2\ T$, $T_e = 600\ eV$, $T_i = 1000\ eV$, $n_e = 5 \cdot 10^{13}\ cm^{-3}$

VI. Instabilities in the High Harmonic Range

Finally, we describe the instabilities driven by the beam ion distributions for ion cyclotron harmonics above the lower hybrid frequency, ω_{lh} (see eq. (9) given below). The ion Bernstein mode which was found to be driven unstable by the beam particle distribution for frequenies below ω_{lh} (see Chapters IV and V) is also unstable for the higher ion cyclotron harmonics. However, we disregard in this Chapter the ion Bernstein mode since their behaviour is similar to that discussed above and describe mainly the behaviour of the lower hybrid mode which can also exist in a pure thermalized plasma. We will find the lower hybrid mode to be resonant in $\underline{k}$-space for the single ion cyclotron harmonics with growth rates much larger than those of the unstable ion Bernstein mode.

First, we simplify the expressions of the thermal plasma contribution to the dielectric tensor elements, ε^p_{ij}, in order to derive the dispersion relation for the lower hybrid mode influenced by the beam particle distribution. For the high harmonics, $l_i \gg 1$, the argument of the modified Bessel functions, b, is large ($k_\perp \rho_i \gg 1$), and we use the asymptotic expansion with respect to the large arguments for the modified Bessel functions in eq. (3), however, this expansion is only valid for the order l_i being sufficiently small ($l_i \ll b$). Generally, this restriction is not valid for the lower hybrid modes decribed in this Chapter, nevertheless, the asymptotic expansion of the resonant terms in eq. (3) gives an upper limit for the modified Bessel functions with larger orders the values of which may be much smaller:

$$e^{-b} \cdot I_{l_i}(b) \approx \frac{1}{\sqrt{\pi}} \frac{\omega_{ci}}{k_\perp v_i} \ll 1 \qquad \text{and} \qquad S_1(b) \approx -\frac{b}{l_i^2}$$

(for the Bessel sum expansion, Ref. /21/ was used). By means of this asymptotic expansion, we can neglect the resonant contribution of the thermal ions to the dielectric tensor. Above the lower hybrid frequency, the modes become unstable for larger values of $k_\parallel$, however, the parallel phase velocity, $\omega/k_\parallel$, is large compared to the electron thermal velocity, v_e. In this case, the electron Landau damping is relatively small and we can use the asymptotic expansion of the plasma dispersion function for the electron contribution in the ε^p_{33} element of eq. (3). With these approximations, we may write the plasma contribution to the dielectric tensor in the form:

$$\begin{aligned}
\varepsilon^p_{11} &\approx 1 + \left(\frac{\omega_{pe}}{\omega_{ce}}\right)^2 - \left(\frac{\omega_{pi}}{l_i \omega_{ci}}\right)^2 \\
\varepsilon^p_{22} &\approx 1 + \left(\frac{\omega_{pe}}{\omega_{ce}}\right)^2 + \left(\frac{k_\perp v_i}{\omega_{ci}}\right)^2 \cdot \left(\frac{\omega_{pi}}{l_i \omega_{ci}}\right)^2 \\
\varepsilon^p_{33} &\approx -\left(\frac{\omega_{pe}}{\omega}\right)^2 \\
\varepsilon^p_{12} &\approx -i \frac{\omega^2_{pe}}{\omega_{ce}\omega} \\
\varepsilon^p_{13} &\simeq \varepsilon^p_{23} \simeq 0 .
\end{aligned} \tag{8}$$

Now, we define the lower hybrid frequency, ω_{lh}, by the condition: $\varepsilon_{11}^p = 0$ where ε_{11}^p is given in eq. (8); in this expression, we replace $l_i\omega_{ci}$ by ω_{lh}:

$$\omega_{lh} = \frac{\omega_{pi}\,\omega_{ce}}{\sqrt{\omega_{pe}^2 + \omega_{ce}^2}}. \tag{9}$$

This definition is equivalent to the dispersion relation in the simplified form of eq. (7) with the dielectric tensor elements of eq. (8) for the limiting case $k_\parallel \to 0$.

As the phase velocity, ω/k, is very small compared to the speed of light, c, we can also use the simplified dispersion relation (7). Furthermore, the electron Landau damping is the dominant damping mechanism with respect to the wave propagation parallel to the magnetic field; consequently, we neglect the beam particle contribution to the ε_{33} element as we have done in the cases of lower ion cyclotron harmonics. Then, the dispersion relation may be written in the form:

$$D \approx \left(\varepsilon_{11}^b + 1 + \frac{\omega_{pe}^2}{\omega_{ce}^2} - \frac{\omega_{pi}^2}{l_i^2\omega_{ci}^2}\right)\cdot\left(1 + \frac{\omega_{pe}^2}{c^2k^2}\right) - \frac{k_\parallel^2}{k^2}\frac{\omega_{pe}^2}{\omega^2} = 0.$$

Since we have neglect the resonant ion cyclotron damping of the thermal ions, the frequency shift, $\delta\omega$, and the growth rate, γ, may be deduced from the ε_{11}^b element. However, the contribution of ε_{11}^b is too complicate for analytical considerations; furthermore, the real part of ε_{11}^b is only small for the cases of interest. Therefore, we only estimate the resonant $k_\parallel$ values of the lower hybrid mode and the growth rate by means of the simplified dispersion relation. The value of the $k_\parallel$ resonance is given by the real part of the dispersion relation:

$$\frac{k_\parallel^2}{k^2} \approx \left(1 + \frac{\omega_{pe}^2}{c^2k^2}\right)\left\{\left(1 + \Re\mathrm{e}\{\varepsilon_{11}^b\}\right)\cdot\left(\frac{l_i\omega_{ci}}{\omega_{pe}}\right)^2 + \left(\frac{l_i\omega_{ci}}{\omega_{ce}}\right)^2 - \left(\frac{\omega_{pi}}{\omega_{pe}}\right)^2\right\}. \tag{10a}$$

In this expression, $\Re\mathrm{e}\{\varepsilon_{11}^b\} \ll 1$ for the beam particle density being sufficiently small ($n_b/n_e < 0.2$, see Fig. 33d) and can be neglected for estimating the normalized growth rate, γ, by means of the imaginary part of the dispersion relation.

$$\gamma = \frac{\Im\mathrm{m}\{\omega\}}{\omega_{ci}} \approx -\frac{l_i}{2}\,\frac{\Im\mathrm{m}\{\varepsilon_{11}^b\}}{1 + \frac{\omega_{pe}^2}{\omega_{ce}^2} - \frac{\omega_{pi}^2}{l_i^2\omega_{ci}^2}}. \tag{10b}$$

Due to the strong γ-dependence of the ε_{11}^b term, the growth rate is not linear related to the beam particle density although ε_{11}^b is proportional to n_b. This effect is dominant in the calculations (see e.g. Fig. 33) for which the full dielectric tensor of the thermal plasma component and both the ε_{11}^b and ε_{22}^b elements of the beam particle contribution are used. Especially due to the ε_{11}^b term, also nonresonant effects of the full beam particle distribution function influence the behaviour of the lower hybrid modes for the different harmonics.

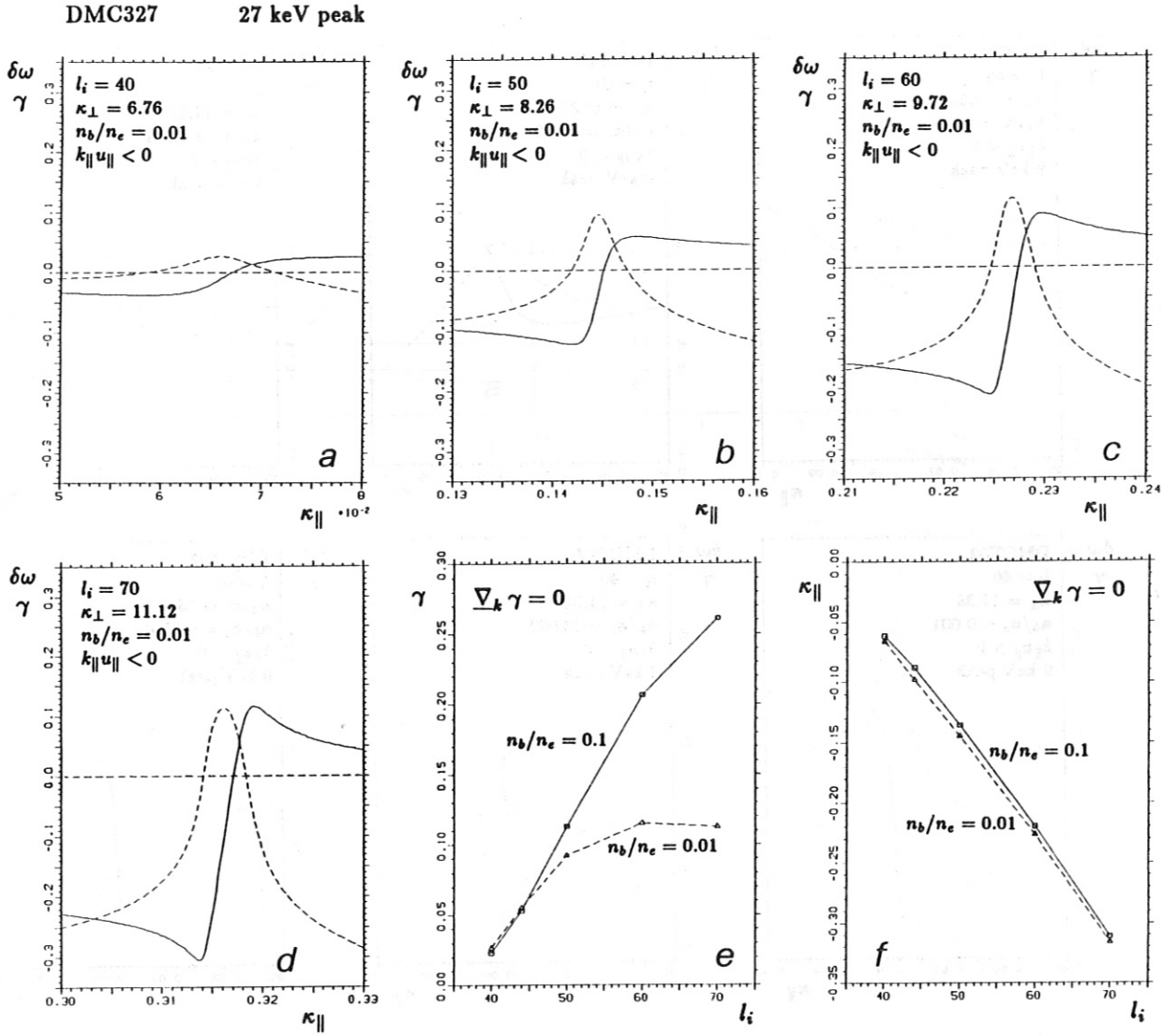

Fig. 31 *Ion cyclotron instabilities driven by the stationary distribution* DMC327: $\delta\omega$ *(solid lines) and* γ *(broken lines) versus* $\kappa_\parallel$ *with* $\kappa_\perp$ *estimated to get maximum growth rates,* γ*, for the different harmonics,* l_i*, in case of counter wave propagation* ($k_\parallel u_\parallel < 0$) *in the plots* **a** *to* **d**. *In the plots* **e** *and* **f**, *the growth rate,* γ*, being maximum with respect to both* $\kappa_\parallel$ *and* $\kappa_\perp$ *and the* $\kappa_\parallel$ *value, respectively, are shown versus the harmonic number,* l_i*, for two beam particle densities. The instability of the lower hybrid mode is only driven by the 27 keV injection peak (see also Fig. 29).*

Plasma parameter: $B_0 = 3.2\ T$, $T_e = 600\ eV$, $T_i = 1000\ eV$, $n_e = 5 \cdot 10^{13}\ cm^{-3}$

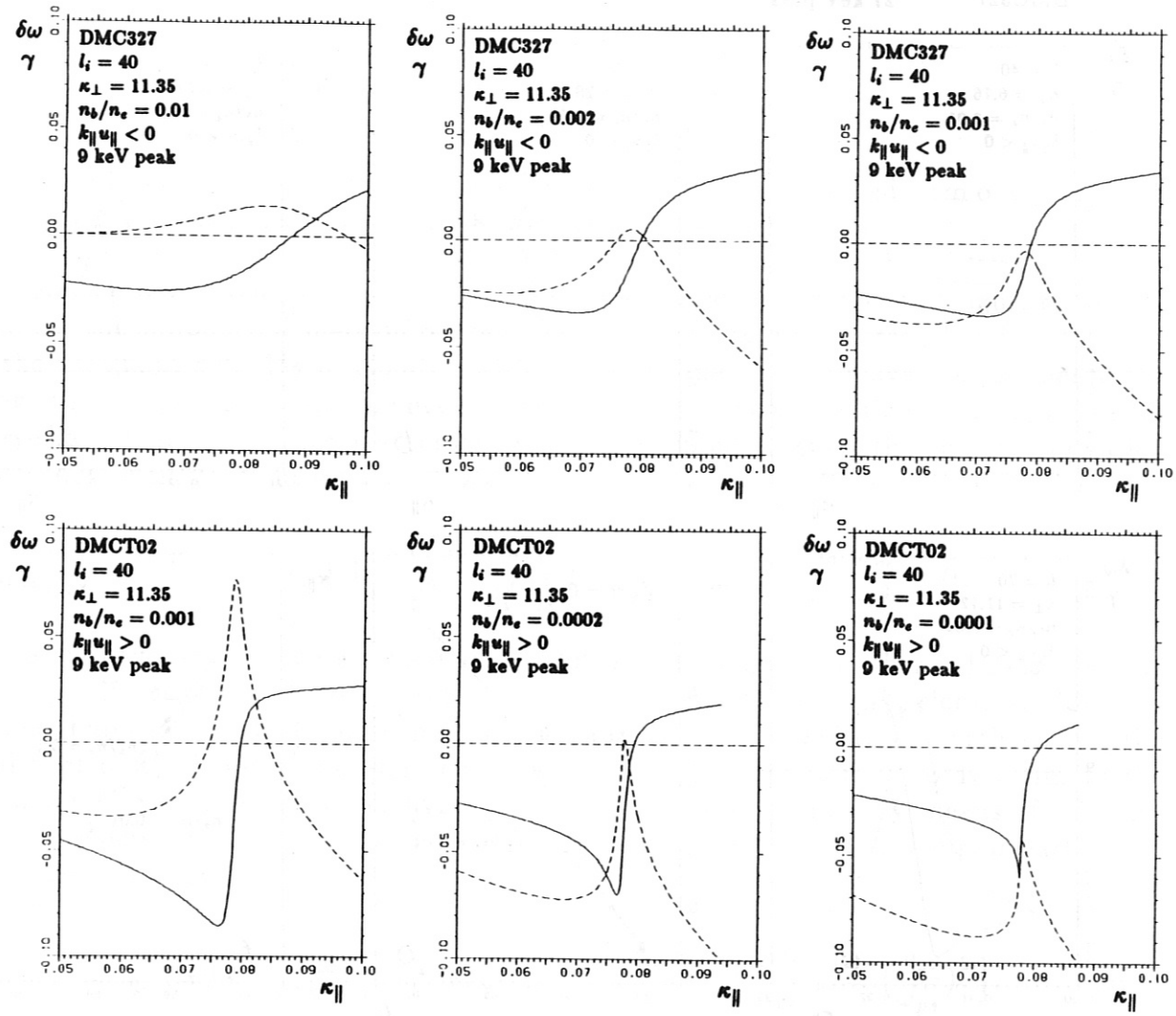

Fig. 32 *Ion cyclotron instabilities (harmonic $l_i = 40$) driven by the stationary distribution* DMC327 *(upper plots) and by the transient distribution* DMCT02 *(lower plots) in case of counter wave propagation ($k_\parallel u_\parallel < 0$): $\delta\omega$ (solid lines) and γ (broken lines) versus $\kappa_\parallel$ with $\kappa_\perp$ being fixed for different beam particle densities, n_b, much less than expected for the experimental conditions in* WVII-A. *Note the threshold of n_b/n_e of about 10^{-3} for the stationary distribution* DMC327 *and of about $2 \cdot 10^{-4}$ for the transient distribution* DMCT02. *The instability of the lower hybrid mode is mainly driven by the 9 keV injection peak. Compare also Figure D3 (Appendix D) with $n_b = 0$ and Figure F3 (Appendix F) with $l_i = 60$. Plasma parameter: $B_0 = 3.2\ T$, $T_e = 600\ eV$, $T_i = 1000\ eV$, $n_e = 5 \cdot 10^{13}\ cm^{-3}$*

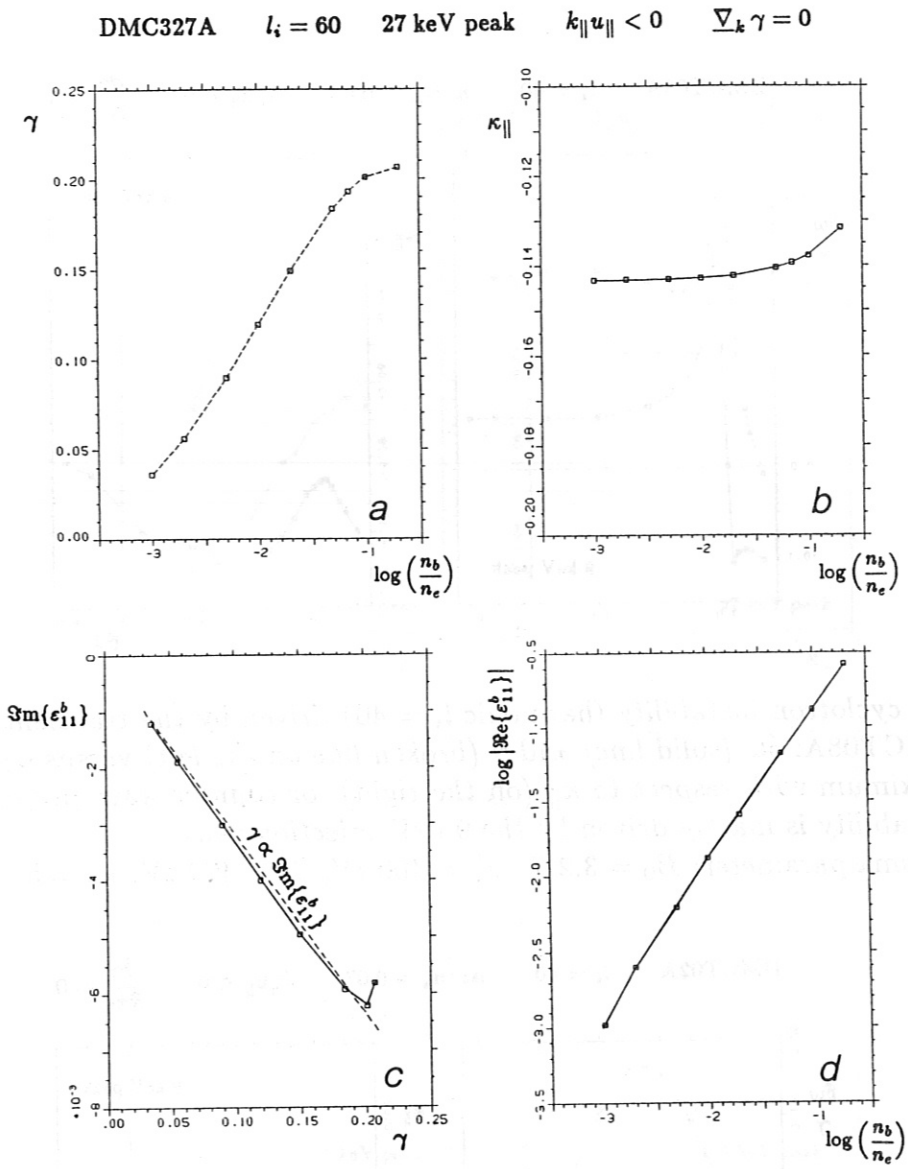

Fig. 33 *Ion cyclotron instability (harmonic $l_i = 60$) driven by the stationary distribution* DMC327A: *maximum normalized growth rate, γ,* (a) *and $\kappa_\parallel$* (b) *versus the beam density ratio, $\log(n_b/n_e)$, in case of counter wave propagation ($k_\parallel u_\parallel < 0$). For the variation of n_b shown, the perpendicular wave number for γ being maximum is nearly constant: $\kappa_\perp = 6.148 \pm 0.006$ (increasing with n_b). In the lower plots, the imaginary part of the beam particle contribution to the dielectric tensor, $\Im m\{\varepsilon^b_{11}\}$, versus γ* (c) *and the real part, $\Re e\{\varepsilon^b_{11}\}$, versus n_b/n_e* (d) *are shown. The broken line in plot* c *is calculated by means of eq. (10b), and from eq. (10a) we estimate $\kappa_\parallel \approx -1.46$ (with $n_b \simeq 0$, comp. plot* b*). The instability of the lower hybrid mode is only driven by the 27 keV injection peak (see also Fig. 39). Plasma parameter: $B_0 = 3.2\ T$, $T_e = 400\ eV$, $T_i = 400\ eV$, $n_e = 5 \cdot 10^{13}\ cm^{-3}$*

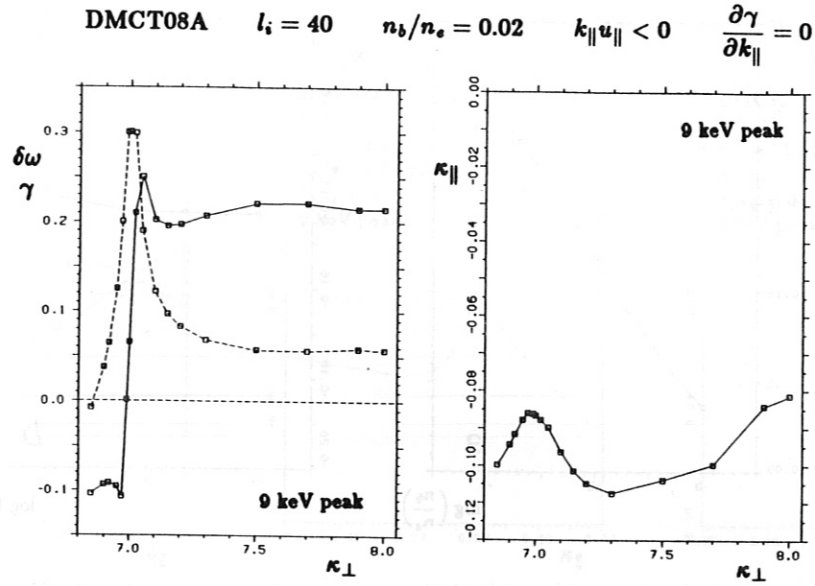

Fig. 34 *Ion cyclotron instability (harmonic $l_i = 40$) driven by the transient distribution* DMCT08A: *$\delta\omega$ (solid line) and γ (broken line on the left) versus $\kappa_\perp$ for γ being maximum with respect to $\kappa_\parallel$ (on the right) for counter wave propagation. The instability is mainly driven by the 9 keV injection peak.*
Plasma parameter: $B_0 = 3.2\ T$, $T_e = 400\ eV$, $T_i = 400\ eV$, $n_e = 5 \cdot 10^{13}\ cm^{-3}$

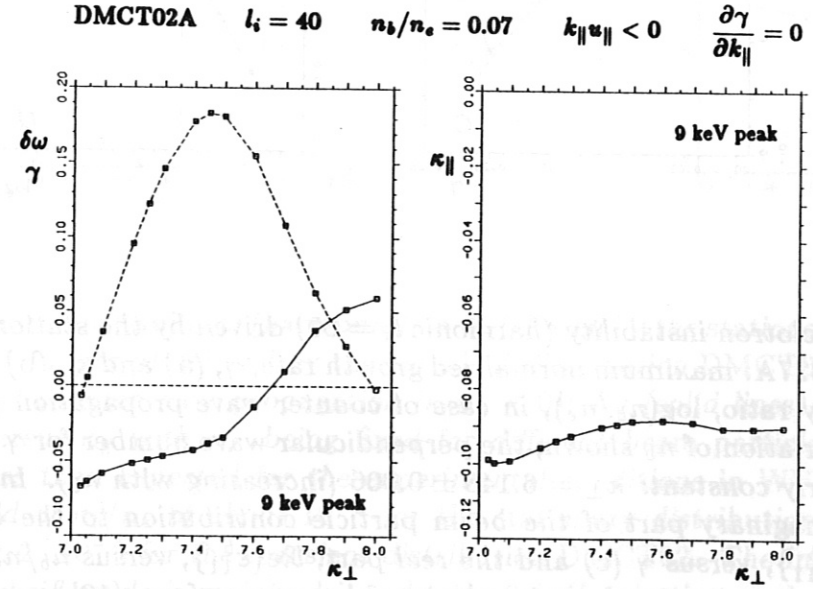

Fig. 35 *Ion cyclotron instability (harmonic $l_i = 40$) driven by the transient distribution* DMCT02A: *$\delta\omega$ (solid line) and γ (broken line on the left) versus $\kappa_\perp$ for γ being maximum with respect to $\kappa_\parallel$ (on the right) for counter wave propagation. The instability is mainly driven by the 9 keV injection peak.*
Plasma parameter: $B_0 = 3.2\ T$, $T_e = 400\ eV$, $T_i = 400\ eV$, $n_e = 5 \cdot 10^{13}\ cm^{-3}$

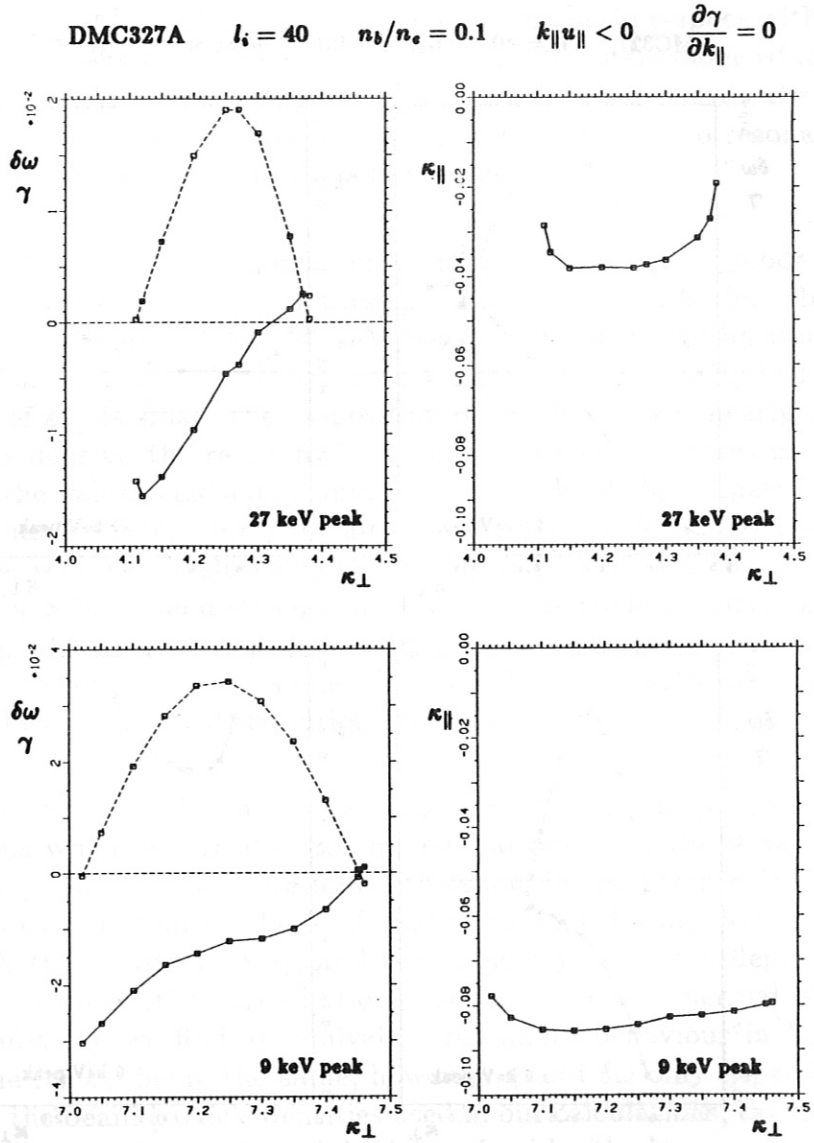

Fig. 36 *Ion cyclotron instability (harmonic $l_i = 40$) driven by the stationary distribution* DMC327A: *$\delta\omega$ (solid line) and γ (broken lines on the left) versus $\kappa_\perp$ for γ being maximum with respect to $\kappa_\parallel$ (on the right) for counter wave propagation. In the upper plots, the instability is is only driven by the 27 keV injection peak, and mainly driven by the 9 keV injection peak in the lower plots.*
Plasma parameter: $B_0 = 3.2\ T$, $T_e = 400\ eV$, $T_i = 400\ eV$, $n_e = 5 \cdot 10^{13}\ cm^{-3}$

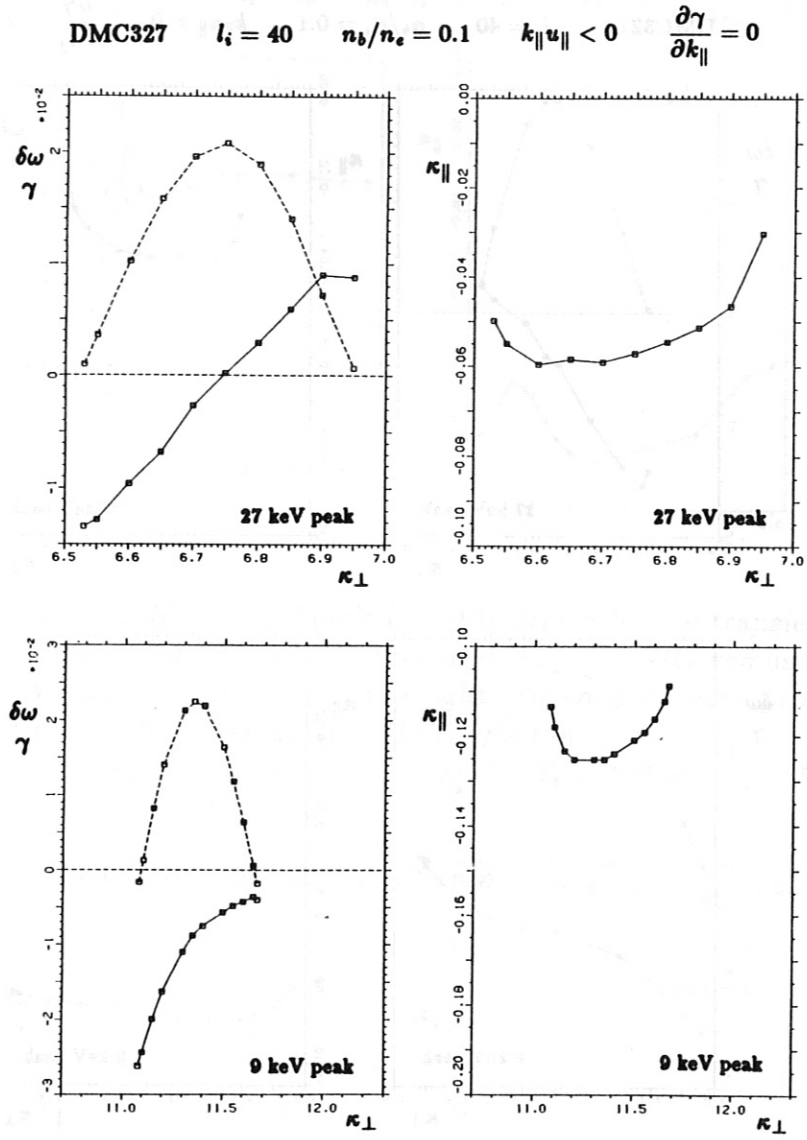

Fig. 37 *Ion cyclotron instability (harmonic $l_i = 40$) driven by the stationary distribution* DMC327: *$\delta\omega$ (solid line) and γ (broken lines on the left) versus $\kappa_\perp$ for γ being maximum with respect to $\kappa_\parallel$ (on the right) for counter wave propagation. In the upper plots, the instability is is only driven by the 27 keV injection peak, and mainly driven by the 9 keV injection peak in the lower plots.*
Plasma parameter: $B_0 = 3.2\ T$, $T_e = 600\ eV$, $T_i = 1000\ eV$, $n_e = 5 \cdot 10^{13}\ cm^{-3}$

The lower hybrid mode is driven unstable by the beam particle distribution only for relative narrow ranges in $k_\perp$ which are related to the domains in $\underline{v}$-space with $\partial f_b / \partial v_\perp > 0$; this mechanism is equivalent to the behaviour of the ion Bernstein mode which we described in the Chapters IV and V. Especially for small beam densities, however, the unstable lower hybrid mode is also resonant with respect to $k_\parallel$ whereas for $k_\parallel$ no resonant effects were found in case of the beam driven ion Bernstein mode.

In Figure 31, the unstable regimes in $k_\parallel$ of the lower hybrid mode are shown for different ion cyclotron harmonics, l_i. In these plots, we estimated $k_\perp$ for γ being maximum related to the 1st harmonic of the 27 keV peak in the distribution function (the $k_\perp$-resonance behaviour is described below); note the small beam density in Fig. 31a to 31d. As the real part of ε_{11}^b is small, the $k_\parallel$-position of maximum γ is nearly independent on the beam particle density, the resonant $k_\parallel$ values estimated by means of eq. (10a) agree within 3% with the values calculated numerically for the different harmonics (see. Fig. 31f). The $k_\perp$ value for maximum γ remains also nearly unaffected by the beam particle density. Both the maximum value of γ (Fig. 31e) and the size of the domain in $\underline{k}$-space with instability ($\gamma > 0$) depend strongly on the beam particle density, n_b. For the lower harmonics in Fig. 31e, we even find the maximum γ decreased in the case of the higher n_b whereas the $k_\parallel$ range of instability is much broader. Here, the saturation effects related to damping by the beam particle distribution dominate.

The n_b-dependence is shown in Figure 32 for very low beam particle densities of both distributions which are related to the 1st harmomic of the 9 keV injection peak with respect to $k_\perp$. In both cases we find a threshold in the beam particle density much below the values expected on the basis of only collisional slowing down for experimental conditions. Both the growth rate, γ, and the frequency shift, $\delta\omega$, depend on n_b as well as on the whole beam particle distribution function. For the thermal plasma only (see Fig. D3, Appendix D), we find an equivalent resonance behaviour in $k_\parallel$ with the same resonant $k_\parallel$-value for $k_\perp$ being the same, however, γ and $\delta\omega$ only depend on the plasma parameters. For the beam particle densities used in our calculations, the imaginary part of the ε_{11} dielectric tensor element is mainly determined by the beam particle contribution, ε_{11}^b, which depends on the whole distribution function, f_b. As a consequence, the frequency shifts as well as the growth rates depend on the single beam particle distribution functions of Chapter III and are quite different to the case of pure thermal plasma. For these high frequencies, the behaviour of the lower hybrid mode is quite similar for co and counter wave propagation. As in the case of the ion Bernstein mode discussed in Chapter V, both the $\underline{k}$-space resonance and the growth rates are nearly unaffected; we only find an upshift of $\delta\omega$ in the case of co wave propagation which is related to the average parallel velocity of the beam particles close to the injection peak being resonant (comp. Figs. 18 and 25).

The dependence of the growth rate, γ, being maximum in $\underline{k}$-space on the beam density is shown in Figure 33a for the ion cyclotron harmonic $l_i = 60$ for counter wave propagation. For higher values of n_b, we get saturation effects for the growth rate, for smaller densities, however, γ is nearly linear related to $\log(n_b)$. In Figure 33b, the position of the $k_\parallel$-

resonance is constant for smaller n_b, the absolute value is slightly decreased with higher beam particle densities. This effect is quantitatively in very good agreement with the analytical approach of eq. (10a). In the lower part of Figure 33, we show the dependence of the beam particle contribution, ε_{11}^b to the dielectric tensor depending on the beam density. Whereas the real part is approximately proportional to n_b (Fig. 33 d), the imaginary part is nearly proportional to γ. The straight line in Fig. 33c is calculated by means of eq. (10b), only for higher densities the saturation effect of γ results in a deviation from the linear relation. Furthermore, the value of the $k_\perp$-resonance related to the 27 keV injection peak in the distribution function is nearly independent on the beam density (see also Fig. 39a).

This behaviour of the lower hybrid mode is typical for all resonances in $\underline{k}$-space for the different beam particle distributions, although the $\underline{k}$-space resonance is more pronounced for higher ion cyclotron harmonics and for smaller beam particle densities used for the numerical calculations discussed above. In the following, we describe the influence of the different beam particle distribution functions on the behaviour of the lower hybrid mode, especially on the growth rate and the frequency shift.

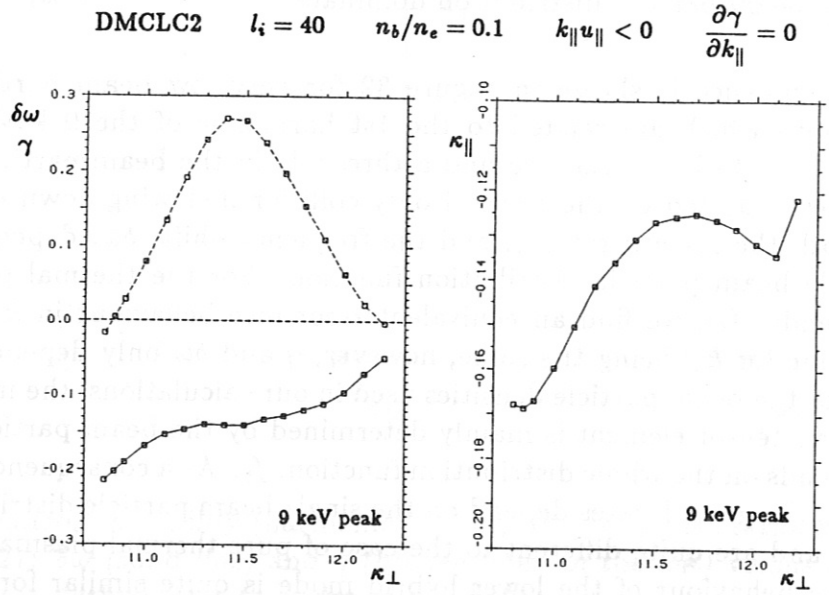

Fig. 38 *Ion cyclotron instability (harmonic $l_i = 40$) driven by the stationary distribution with loss cone* DMCLC2: *$\delta\omega$ (solid line) and γ (broken line on the left) versus $\kappa_\perp$ for γ being maximum with respect to $\kappa_\parallel$ (on the right) for counter wave propagation. The instability is mainly driven by the 9 keV injection peak (comp. the lower plots of Fig. 37).*
Plasma parameter: $B_0 = 3.2\ T$, $T_e = 600\ eV$, $T_i = 1000\ eV$, $n_e = 5 \cdot 10^{13}\ cm^{-3}$

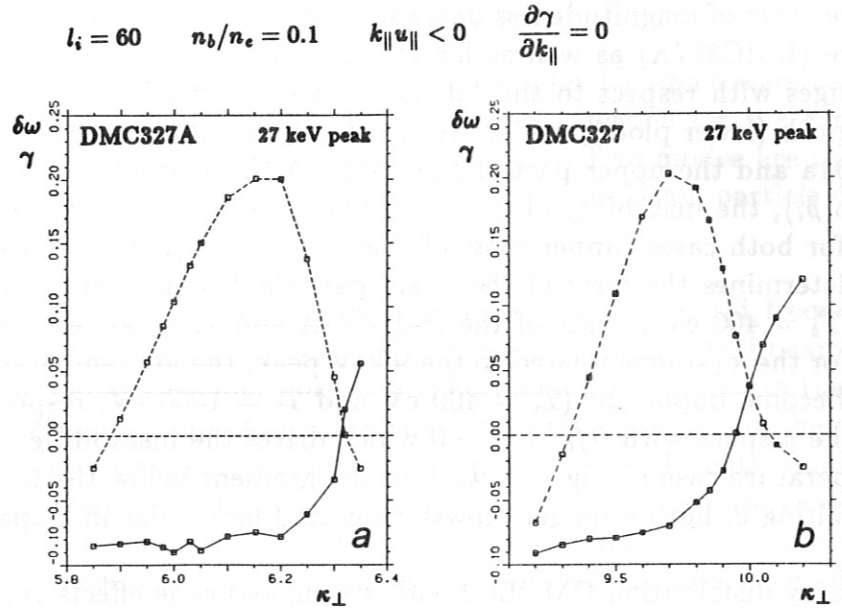

Fig. 39 *Ion cyclotron instabilities (harmonic $l_i = 60$) driven by the stationary distributions* DMC327A (a) *and* DMC327 (b): *$\delta\omega$ (solid lines) and γ (broken lines) versus $\kappa_\perp$ for γ being maximum with respect to $\kappa_\parallel$ for counter wave propagation which is nearly constant ($\kappa_\parallel = -0.137 \pm .003$ in case of* DMC327A *and $\kappa_\parallel = -0.215 \pm .003$ in case of* DMC327. *The instability is only driven by the 27 keV injection peak (comp. the upper plots in Figs. 36 and 37).*

In Figures 34 and 35, the instabilities of the lower hybrid mode for the ion cyclotron harmonic $l_i = 40$ related to the 1st harmonic in the $k_\perp$-resonance of the 9 keV peak in the beam particle distribution are shown for counter wave propagation. In the case of the transient distribution DMCT02A (Fig. 35), only the lower hybrid mode is driven unstable, whereas in the case of the distribution DMCT08A both modes are unstable. For lower perpendicular wave numbers ($\kappa_\perp < 7.0$), the unstable mode is the lower hybrid mode with mainly negative frequency shift; for larger $k_\perp$, however, the ion Bernstein mode becomes unstable with strong positive frequency shift and with a much broader range of instability with respect to $k_\parallel$. Within this $k_\perp$ range (at $\kappa_\perp \simeq 7.0$), we find a strong interaction of the two unstable modes leading to the very strong increase of the frequency shift and the narrow range for which γ being maximum. This behaviour is quite different to the case of the DMCT02A distribution (Fig. 35) with similar $k_\perp$-resonance with respect to the 9 keV injection peak. Both unstable modes depend strongly on the form of the beam particle distribution function. However, in case of the DMCT02A distribution, we find also mode interaction for the lower $k_\perp$-range which is resonant to the 27 keV injection peak, here, the growth rates are much smaller ($\gamma < 0.02$). The instabilities driven by these transient distributions are very strong, the group velocities relative small. Consequently, the mode increase distances, $\underline{v}^G/\Im\mathrm{m}\{\omega\}$, can be sufficiently small and we must expect that the instabilities strongly affect the beam particle distributions.

The stationary beam particle distributions without loss cone effects in Figures 36 and 37 are about one order of magnitude less unstable than the transient distributions. For the low temperature (DMC327A) as well as for the high temperature case (DMC327), both unstable $k_\perp$-ranges with respect to the 1st harmonics of the 27 keV peak (upper plots) and the 9 keV peak (lower plots), respectively, are only related to the lower hybrid mode (see also Fig. 31a and the upper part of Fig. 32). With regard to the scaling factor in κ (~ 1.6 due to ρ_i), the instability of the lower hybrid mode driven by the 27 keV peak is very similar for both cases (upper plots of Figs. 36 and 37); the electron temperature which mainly determines the form of the beam particle distribution for high energies is rather similar ($T_e = 400$ eV in case of the DMC327A and $T_e = 600$ eV for the DMC327 distribution). For the $k_\perp$-range related to the 9 keV peak, the ion temperatures which are more different become important ($T_i = 400$ eV and $T_i = 1000$ eV, respectively) for the shape of f_b in the $\underline{v}$-space with $\partial f_b / \partial v_\perp > 0$ which drives the instabilities. Consequently, in the low temperature case of Fig. 36, we find the gradient below the 9 keV peak more pronounced resulting in both stronger growth rates and larger size in $\underline{k}$-space with $\gamma > 0$.

The stationary distribution DMCLC2 with strong loss cone effects resulting in much more pronounced gradients below the injection energies is about one order of magnitude more unstable than the equivalent distribution without loss cone, DMC327, for the $k_\perp$-range related to the 9 keV peak (see Fig. 38). Furthermore, the size of the resonant region in $\underline{k}$-space for which the lower hybrid mode is driven unstable is significantly increased.

Finally, we shortly discuss the behaviour of the unstable lower hybrid mode driven by the 27 keV peaks in the stationary distributions DMC327A and DMC327 at the ion cyclotron harmonic $l_i = 60$ (see Figure 39). Similar to the $l_i = 40$ cases (Figs. 36 and 37), the mode behaviour in Fig. 39a and 39b is nearly independent on the plasma temperature since the beam particle distributions for the higher energies are rather similar and the simplified dispersion relation (eqs. 10a and 10b) do not dependent on the plasma temperatures. The growth rates, however, are strongly increased with l_i (comp. Fig. 31e). Analogous to the transient distributions at lower harmonics, l_i, we find sufficiently small mode increase distances to get large electric fields for the lower hybrid mode which will affect the domains in the beam particle distribution functions driving the instabilities.

VII. Conclusions and Experimental Results

All beam particle distribution functions of Chapter III which were calculated on the basis of only collisional slowing down with densities expected for the experimental conditions were found to drive ion cyclotron instabilities. Two modes are unstable: the ion Bernstein mode which is in general strongly affected by the beam particle distribution and the lower hybrid mode in the high frequency range.

In the ion cyclotron harmonic range below the lower hybrid frequency, we found that all transient distributions functions after switch on the neutral beam injection drive the ion Bernstein mode unstable. For the low harmonics, the modes in the colder plasma, especially with lower ion temperature, are more unstable. By means of the mode dispersion we found that the group velocity can be small enough to get sufficiently small mode increase distances so that absolute instablility must be expected. The ion Bernstein mode for the low and intermediate ion cyclotron harmonics, however, remains stable for the stationary beam particle distributions; only in the case of very strong loss cone effects where the fast particle confinement time is of the order of the average slowing down time the ion Bernstein mode becomes unstable in the intermediate harmonic range.

Close to and above the lower hybrid frequency, all beam particle distributions investigated in this report were found to be unstable. For these high ion cyclotron harmonics, the growth rates become large and strong absolute instability is expected for those values of the wave numbers for which the group velocity is sufficiently small. However, these unstable lower hybrid modes are strongly resonant in $\underline{k}$-space; the resonance in $k_\perp$ which is related to those domains of the beam particle distribution function with $\partial f_b/\partial v_\perp > 0$ is equivalent to the case of the unstable $k_\perp$-ranges of the ion Bernstein mode. The $k_\parallel$-resonance appears only in case of the lower hybrid mode and is more pronounced for higher harmonic numbers, l_i, and smaller beam particle densities.

The resonance condition in $k_\perp$ related to the domains of the beam particle distribution function with $\partial f_b/\partial v_\perp > 0$ depends also on the ion cyclotron harmonic number, l_i. In Appendix C, we have derived the conditions for which the modes may be driven unstable. From eq. (C4) we get the following two conditions which are equivalent:

$$\text{maximize } \Im\text{m}\{\omega\} \iff \text{minimize } \left\{ k_\perp \int_0^\infty J_{l_b}(a)\, J'_{l_b}(a) \int_{-\infty}^{\infty} f_b \, dv_\parallel \, dv_\perp \right\}$$

$$\iff \text{maximize } \left\{ \int_0^\infty J^2_{l_b}(a) \int_{-\infty}^{\infty} \frac{\partial f_b}{\partial v_\perp} \, dv_\parallel \, dv_\perp \right\}$$

with $a = k_\perp v_\perp/\omega_{cb}$ and $l_b \simeq l_i \omega_{ci}/\omega_{cb}$. However, these expressions must be sufficiently large to predominate the damping by both the thermal ions and the electrons. Furthermore, the contribution of the domains in f_b with $\partial f_b/\partial v_\perp > 0$ must also be larger than the contributions of the rest of f_b; instability driven by these beam particles can be damped by the remains. So, the expression must be sufficiently negative for the upper condition and positive for the lower condition, respectively.

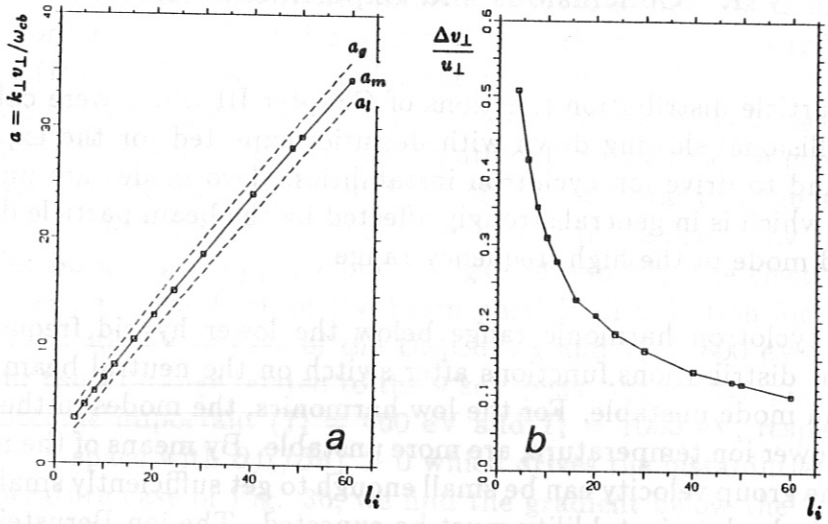

Fig. 40 *1st minimum, a_m (solid line), and the 1st two zeros, a_l and a_g (broken lines in* a*), of $J_{l_b}(a)\,J'_{l_b}(a)$ and the normalized resolution in velocity space, $\Delta v_\perp / u_\perp = (a_g - a_l)/a_m$ (in* b*), versus the ion cyclotron harmonic number, l_i $(= 2\,l_b)$.*

We found most of the unstable domains in $\underline{k}$-space being related to the single peaks in f_b close to the injection energies, especially to the 9 keV as well as to the 27 keV peak. By means of the upper minimisation condition, we can estimate the broadness of the resonance related to $v_\perp$. Let us assume f_b being a δ-δ function (see eq. 4) located at the injection energies. Then, we estimate $k_\perp$ from the argument, a_m, of the 1st minimum of $J_{l_b}(a)\,J'_{l_b}(a)$; the values of a_m are given in Fig. 40a (solid line) depending on l_i. Instability is driven if $J_{l_b}\,J'_{l_b} < 0$, leading to $a_l < a < a_g$ (broken lines in Fig. 40a). Then, we define the broadness of the $v_\perp$-resonance by the expression: $\Delta v_\perp = u_\perp\,(a_g - a_l)/a_m$ where $u_\perp$ being the perpendicular velocity related to the single injection peak; in Figure 40b, $\Delta v_\perp / u_\perp$ is plotted depending on l_i. Within this simple approach, all beam particles with $u_\perp - v_\perp < \Delta v_\perp$ contribute to the instability (the condition $v_\perp < u_\perp$ results from the equivalent maximisation condition). Furthermore, instability may also be driven by the higher periods of the Bessel function expression $J_{l_b}(a)\,J'_{l_b}(a)$. However, we have concentrate our analysis only to the 1st harmonics in $k_\perp$ for the single injection peaks since we expect for this the maximum contribution to the instability and, on the other hand, since we get numerical problems for very large arguments a due to the finite mesh size in $\underline{v}$-space we used in the Monte Carlo simulation of the beam particle distribution functions.

Consequently, small domains in the beam particle distribution with $\partial f_b / \partial v_\perp > 0$ will drive mainly the high ion cyclotron harmonics unstable. Furthermore, the Bessel functions, $J_{l_b}(a)$, are very small for a being significantly smaller than l_b; the instability driven by the highest energy peak in f_b is only weakly damped by the slowed down beam particles for higher harmonics, l_i. This is the reason that we found the stationary beam particle distributions to be stable in the lower and the intermediate frequency range, whereas the transient distributions after switch on the injection are also unstable in the low harmonic

range where the resonance in $k_\perp$ is nearly as broad as in the high harmonic range. Also for the transient distributions analyzed, the domains in $\underline{v}$-space which drive the instability are relative narrow and located close below the injection peaks. Especially for the 9 keV peak, however, the fraction of the beam particles which can compensate the driving of the instability is much less than for the stationary distributions. Nevertheless, the very low ion cyclotron harmonics with broad $\Delta v_\perp$ being resonant with respect to $k_\perp$ are driven by a much smaller domain with $\partial f_b / \partial v_\perp > 0$.

The electric fields, $\underline{E}$, of both the ion Bernstein and the lower hybrid mode are nearly parallel to $\underline{k}$: $E_1 \gg E_3 \gg E_2$ where the directions are defined by $k_1 = k_\perp, k_2 = 0$ and $k_3 = k_\parallel$. Due to the electron Landau damping, ϵ_{33} is very large compared to all other terms and electron heating must be taken into account although $E_3 \ll E_1$ was found for all cases investigated. Only for the very low harmonics with small $k_\parallel$, the unstable ion Bernstein mode driven by the transient beam particle distributions is mainly characterized by ion cyclotron damping due to the thermal ions. In case of the higher harmonics and especially for the lower hybrid mode, ion cyclotron damping by the thermal ions is small compared to the electron Landau damping as well as to the ion cyclotron damping by the slowed down beam particles. This later effect, however, cannot be estimated since we analyzed the beam particle distributions only in the whole velocity space not separated in domains driving and damping the instabilities.

The absolute instabilities found in the different frequency ranges result in strong electric fields which modify the beam particle distribution functions (quasi-linear effects). Those beam particles which drive the instabilities (domains with $\partial f_b / \partial v_\perp > 0$) are slowed down by these electric fields until they leave these domains. In case of the stationary beam particle distributions which are unstable only at high harmonics, the distribution functions close below the injection peaks are flattened: the values of the gradients are decreased but the sizes of the domains with $\partial f_b / \partial v_\perp > 0$ may be slightly increased. As the modes strongly depend on the form of f_b in these domains (not only on the contribution to n_b), the unstable ion cyclotron modes will be significantly modified by these quasi-linear effects. However, as the main part of the slowing down distribution function was found to be stable against all ion cyclotron modes, we will expect only a relative small effect of this slowing down by the unstable ion cyclotron modes to the average slowing down which is dominated by the Coulomb interaction of the beam particles with electrons and thermal ions. In case of stationary distributions with strong loss cone effects, the slowing down due the ion cyclotron modes may be increased. In this high harmonic range, we expect no direct heating of the thermal ions by these instabilities. Only the effect that slowed down beam particles are accelerated and transfer more energy to the thermal ions due to Coulomb interaction may slightly influence the heating balance between ions and electrons. Furthermore, the transient distributions after switch off the neutral beam injection are characterized by the braod slowing down spectrum which is equivalent to the case of the stationary distributions, domains with $\partial f_b / \partial v_\perp > 0$ will disappear. Consequently, we expect the switching off phase more stable against ion cyclotron instabilities than the stationary phase.

The situation in case after switch on the neutral beam injection, however, will be quite different. We found low harmonic ion Bernstein modes being unstable. As the beam particles close below the injection peaks are slowed down by the modes, the domains with $\partial f_b/\partial v_\perp > 0$ are significantly enlarged wheres the value of the gradient is decreased. Then, we expect that the very low ion Bernstein modes with resonance to the broader domain $\Delta v_\perp$ will become more unstable than in the case of the smaller domains with steeper gradients analyzed in Chapter IV. Even the fundamental of the beam particles ($l_i = 2$) which was found to be stable may become unstable due to the quasi-linear deformation of the beam particle distribution function. As the low harmonic ion Bernstein modes are mainly damped by the thermal ions, we expect much stronger ion heating in the switch on phase of the neutral beam injection. This increased ion heating (some times called *anomalous slowing down*) will be reduced due to the formation of the broader shape in the slowing down distribution maintained by the collisional interaction. Consequently, whithin a time of the order of the average slowing down time due to Coulomb friction we expect strong instability of the low harmonic ion Bernstein modes.

To sum up, we expect the beam particle distributions being stable against low harmonic ion Bernstein modes for the stationary phase as well as for the phase after switch off the neutral beam injection. The instabilities related to the higher ion cyclotron harmonics will only smooth the distribution functions in the vicinity of the injection energies. The average heating balance between ions and electrons is mainly determined by the collisional slowing down of the beam particles. After switch on the neutral beam injection, however, we expect strong instability of the ion Bernstein modes for low harmonics resulting in preferential ion heating lasting about an average slowing down time.

In the following part of this section, we will discuss results of W VII-A experiments which had been carried out to clarify the slowing down mechanism of the neutral beam injection. Most of these experiments are based on the time phases of both switch on and switch off the neutral beam injectors which have very short switching times ($\Delta t \sim 0.1$ ms). However, a relative shift up to 1 ms in the absolute time scales may exist with respect to the single diagnostics, especially to the switch on or switch off data of the injectors determined independently from the experimental time scale. Consequently, the switch on/off moments are determined from the diagnostic data. With regard to the evaluation, the time resolution achieved is mainly determined by the data sampling of the single experiments which was partially improved for the purpose of these experiments.

First, let us discuss the stationary slowing down distribution function of the beam particles measured by the charge exchange (CX) diagnostic which is shown in Figure 41. This H^0 spectrum (dots) in the high energy range was measured perpendicular to the magnetic field, the mean angle of the neutral beam injection is about 84^o to $\underline{B}$. The energy resolution of the CX analyzer is of the order of 20% leading to the smoothed energy spectrum which is directly derived from the count rates. The energy dependence of the CX-cross section which strongly decreases for $E > 10$ keV is not taken into account, with this correction, the high energetic H^0-distribution function will be slightly increased.

From Monte Carlo simulation of the slowing down of the H^0 beam particles based only on collisional interaction (see Ref. /17/), the perpendicular flux, $v_\perp \cdot f_b$, was estimated (solid

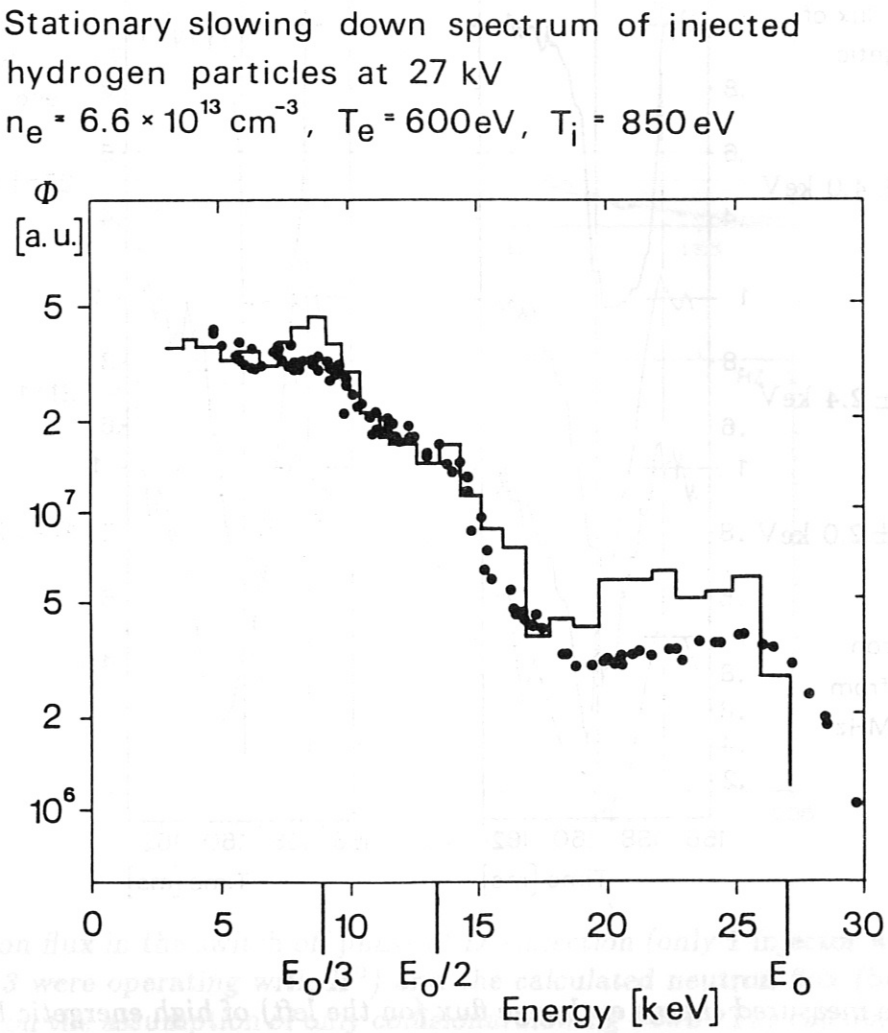

Fig. 41 *The perpendicular energy spectrum of the charge exchange H^0 neutrals (dots) and the perpendicular flux, $v_\perp \cdot f_b$, calculated by Monte Carlo simulation (see Ref. /17/). The measured energy spectrum is smoothed due to the energy resolution of the CX-analyser of about 20%.*

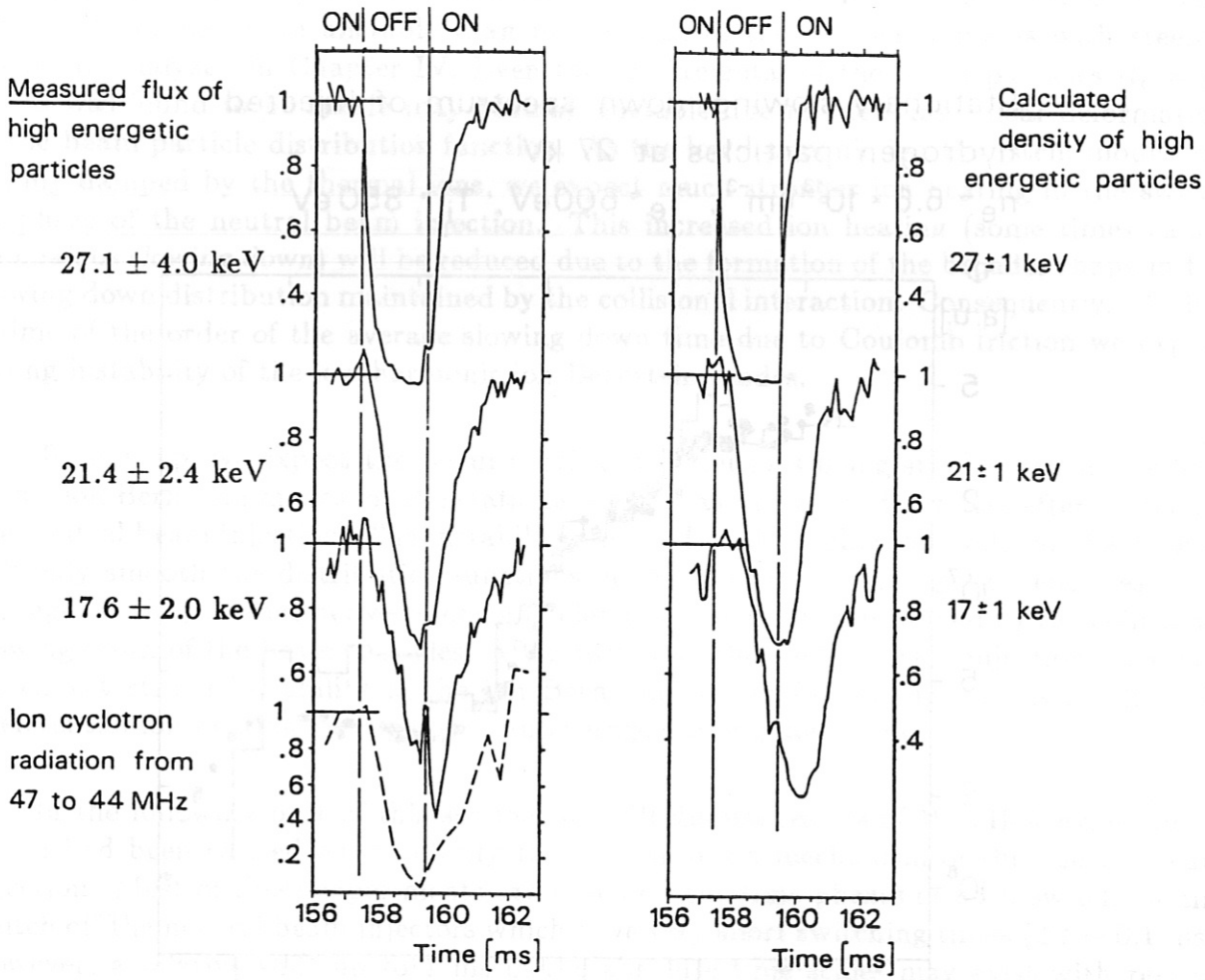

Fig. 42 *The measured charge exchange flux (on the left) of high energetic beam particles perpendicular to the magnetic field in 3 energy channels around 27.1, 21.4 and 17.6 keV and the ICE signal in the range between 44 and 47 MHz (broken line) and the calculated flux (on the right) by means of Monte Carlo simulation for equivalent energy channels in the phase of switch off the neutral beam injection for 2 ms. The time resolution of the CX measurements is of about 0.1 ms.*

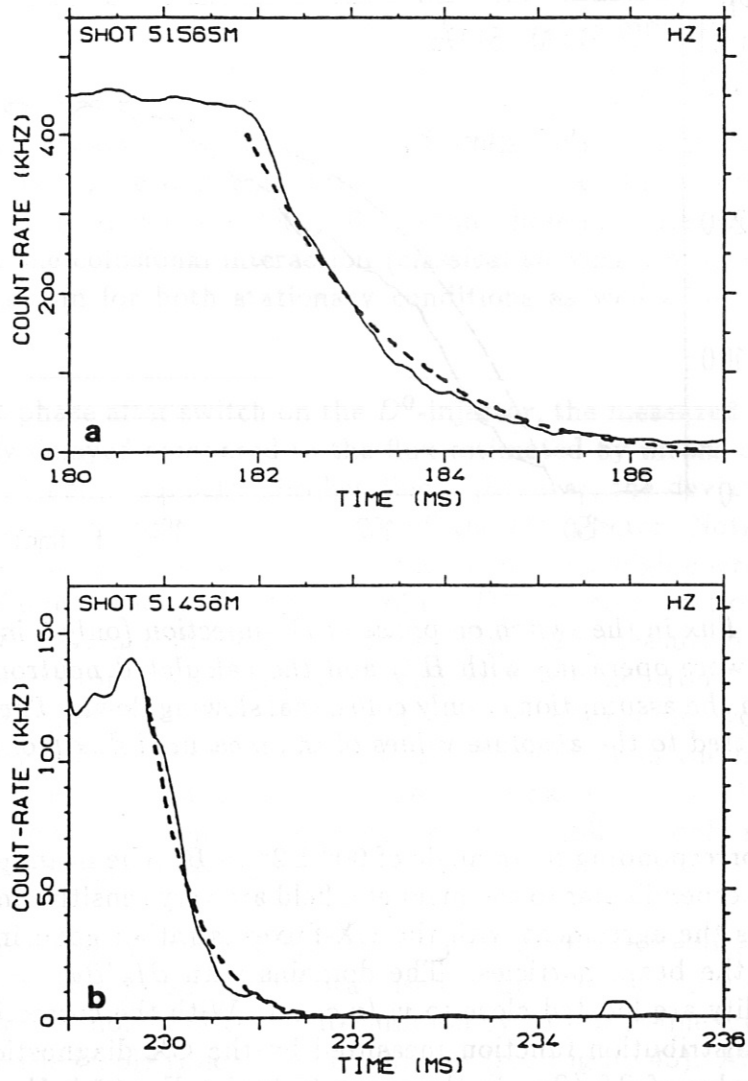

Fig. 43 *Neutron flux in the switch off phase of D^0-injection (only 1 injector with D^0, the other 3 were operating with H^0) and the calculated neutron flux (broken lines) based on the assumption of only collisional slowing down. The calculated neutron flux is fitted to the measured flux with respect to the absolute values as well as to the time of switch off the D^0-injector. For correlating the neutron flux measuements with calculations, the D^0-injection was shifted in time corresponding to changes of the plasma density and temperatures. The slowing down time (from 27 keV to 5 keV) is about 11 ms in case (a) and about 4 ms in case (b). Here, the decay time of the neutron flux is given by the slowing down time in the very high energy range from 27 keV to about 20 keV due to the energy dependence of the D^+-D^+ cross section.*

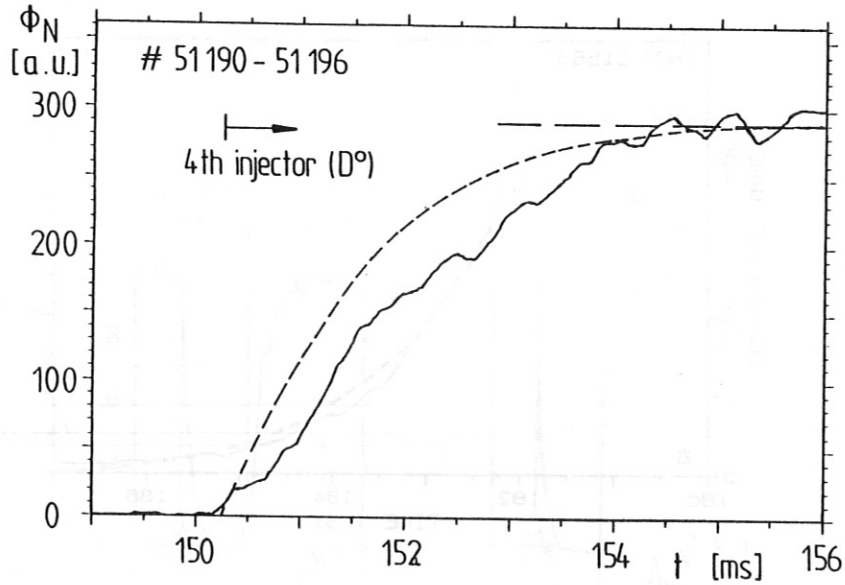

Fig. 44 *Neutron flux in the switch on phase of D^0-injection (only 1 injector with D^0, the other 3 were operating with H^0) and the calculated neutron flux (broken line) based on the assumption of only collisional slowing down. The calculated neutron flux is fitted to the absolute values of the measured flux (compare Fig. 43).*

line in Fig. 41) corresponding to an angle of $90^o \pm 2^o$ to $\underline{B}$. The beam particle distribution functions nearly perpendicular to the magnetic field are very sensitive in pitch, $v_{||}/v$ (comp. Chapter III), thus the agreement with the CX-fluxes is rather good indicating collisional slowing down of the beam particles. The domains with $\partial f_b/\partial v_\perp > 0$, which drive ion cyclotron instability are located close to $v_{||}/v \simeq 0.1$. With the correction of the CX-cross section, the H^0 distribution function measured by the CX diagnostic ($v_{||} \approx 0$) yields a slightly positive value of $\partial f_b/\partial v_\perp$ in the range 19 keV $< E <$ 25 keV.

In Figure 42, the normalized fluxes measured by the CX diagnostic and calculated by means of Monte Carlo simulation are shown for a short switch off phase (2 ms) of all neutral beam injectors. Only in the 17 keV energy channel, the time delay of the CX-flux decrease is significantly smaller than in the equivalent energy range of the simulation. However, the global comparison leads to the conclusion that the beam particle slowing down is dominated by collisions after switch off the neutral beam injection. The ion cyclotron emission (ICE) with frequencies around the H^0 cyclotron frequency ($= \omega_{cb}/2\pi$) measured by a Langmuir probe in the limiter shadow (broken line on the left of Fig. 42) has similar time dependence as the CX-flux in the 21 keV energy channel. The amplitude of the ion cyclotron emission, however, is much less than in the phase after switch on the injection (comp. Fig. 45).

The slowing down mechanism of the injected beam particles could be clarified by neutron flux measurements using an additional neutral beam injector operating with D^0

into a D^+ target plasma (for further detail see Ref. /10/). It was clearly shown, that the neutron flux originating from D^+-D^+ reactions is toroidally symmetric, no enhancement close to the injection port was found. Furthermore, the measured neutron flux is within a factor of 2 in agreement with calculations based only on Coulomb friction of the fast beam particles for stationary conditions. The measured neutron flux after switch off the D^0-injector is shown in Figure 43 in comparison to the calculated flux (broken lines) based only on collisional slowing down (see Ref. /10/). From these measurements we must draw the conclusion, that the collisional interaction (*classical slowing down*) is the dominating slowing down mechanism for both stationary conditions as well as after switch off the injection.

In the transient phase after switch on the D^0-injector, the measured neutron flux (see Figure 44) is slightly delayed compared to the flux estimated by means of only collisional interaction of the fast beam particles (broken line). However, the deviation is significant in comparison to the measurements after switch off the D^0-injector. Notice, that the time scale is only determined by the slowing down time in the very high energy range from 27 keV to about 20 keV due to the strong decrease of the D^+-D^+ cross section, these times are much smaller than the average slowing down times. For these measurements, the moment of switch on the D^0-injector was accurately determined by the neutron flux increase at the injection port for an equivalent shot whithout plasma where the neutron flux originates from D^0-D^0-reactions within the target plates. The time delay of the measured neutron flux indicates a much faster slowing down of the beam particles close below the 27 keV injection energy which may be related to ion cyclotron instabilities only in the phase after switch on the neutral beam injection.

The ion cyclotron emission was received with a Langmuir probe located in the limiter shadow outside of the edge plasma which was used as an antenna. In a narrow frequency band around the low harmonics of the deuterium ion cyclotron frequency, the ICE signals were measured over the whole time of the discharges (see Figure 45). After switch on the H^0-injectors (lower trace), strong ICE signals were received only for the harmonics of the hydrogen ion cyclotron frequeny ($= \omega_{cb}$). This situation is equivalent to the assumptions of our calculations in this report. After switch on of the D^0-injector, ICE was detected at those harmonics of deuterium which are not related to harmonics of hydrogen. This indicates that the ion Bernstein mode at low harmonics is driven unstable by the transient beam particle distribution as we found in Chapter IV. However, emission is found also for the fundamental ion cyclotron mode which may be an indication for quasi-linear effects we expect for the transient distributions after switch on the injection (see the first part of this Chapter). The ICE signals are strongly reduced as the injection conditions become stationary after some average slowing down times. This is consistent with our findings that the bulk part of the slowing down distribution functions is determined by collisional interactions being stable with respect to low ion cyclotron harmonics. The situation for the even harmonics of the deuterium ion cyclotron frequency after switch on the D^0-injector is more complicate: the domains in $\underline{v}$-space of the deuterium beam particle distribution driving the instability are analogous to the case of hydrogen.

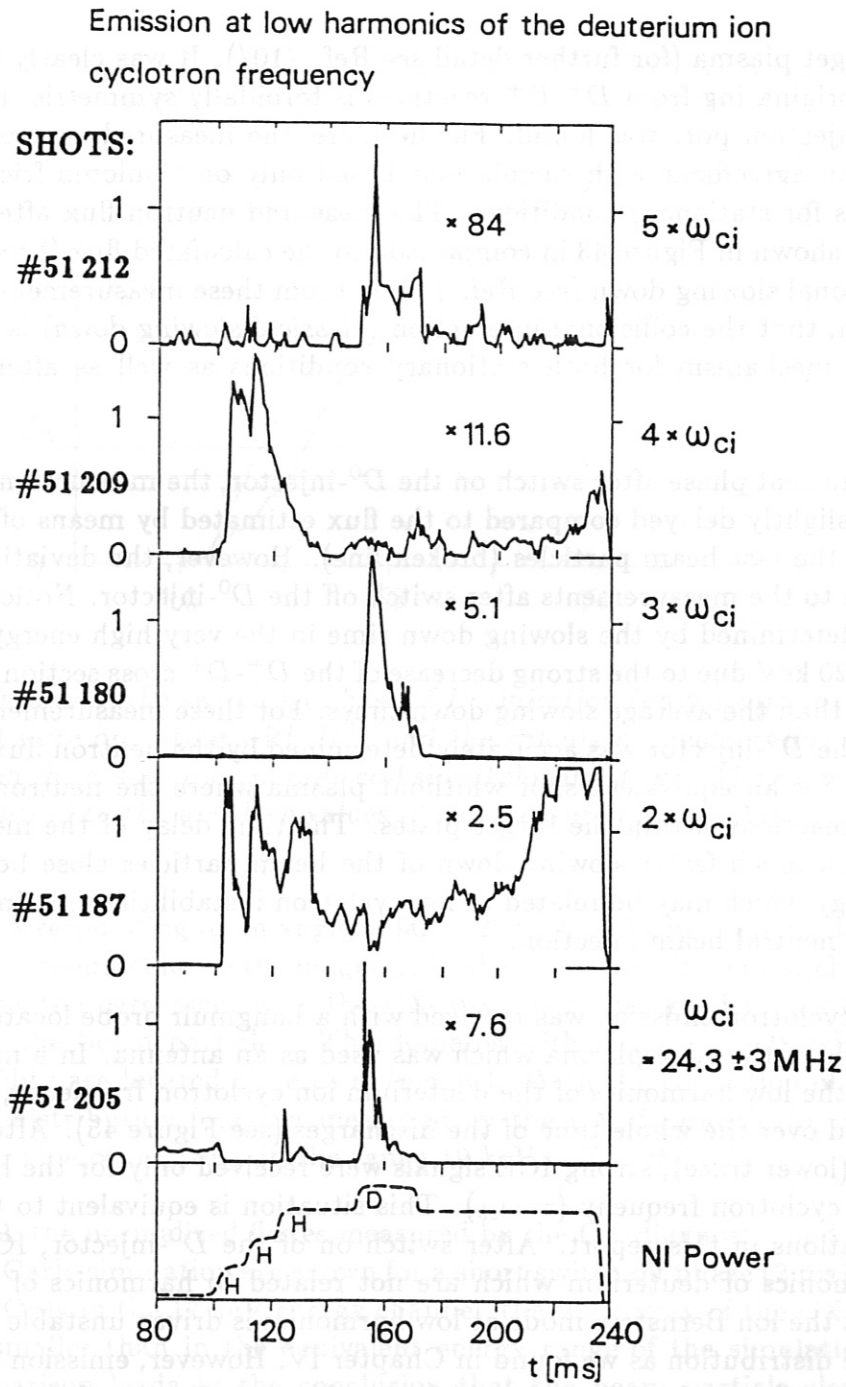

Fig. 45 *Ion cyclotron emission received by a Langmuir probe outside the plasma within a small frequency band around the low ion cyclotron harmonics. The probe located in the limiter shadow is used as an antenna. In this series of discharges maintained by 3 injectors operating with H^0, a 4th injector with D^0 is superposed (lower trace). The factors within the single plots represent the relative r.f. amplification factor.*

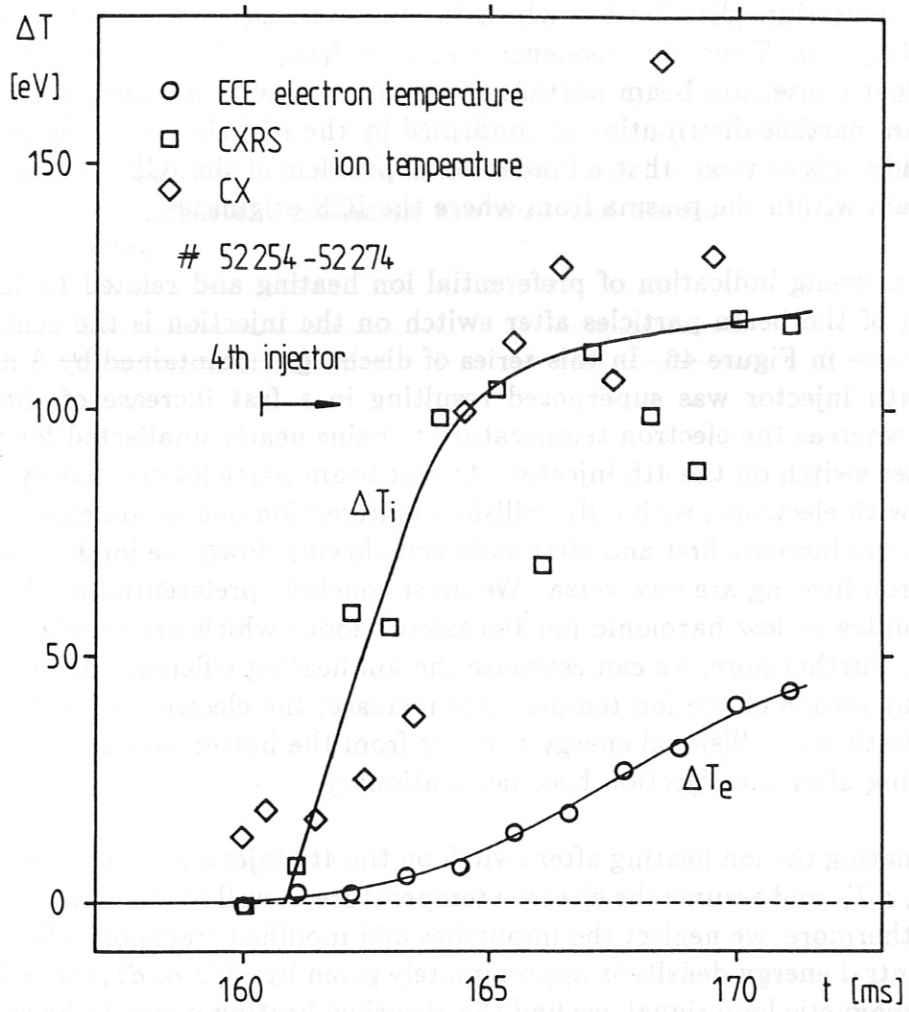

Fig. 46 *Ion temperature and electron temperature incresae, ΔT, versus time after switch on a 4th neutral beam injector in the central region. The electron temperature increase (○) is estimated from ECE measurements, the CXRS ion temperature (□) from Doppler broadening of oxygen impurity line (O VIII) and the CX ion temperature (◇) by means of energy analysis of the D^0 charge exchange flux. As the discharge was not stationary before the 4th injector was switched in, we linear extrapolated the temperatures to deduce the temperature increase shown; this ion temperature increase is about 2 eV/ms, the electron temperature was nearly constant. The ion temperature was between 650 eV (CXRS) and 700 eV (CX), the electron temperature about 500 eV (ECE) in rather good agreement with the values derived from the Thomson diagnostic. The central value of n_e was about $6 \cdot 10^{13}$ cm^{-3}.*

However, the broad slowing down distribution of the hydrogen beam particles which stabilizes the domains in the hydrogen distribution with $\partial f_{H+}/\partial v_\perp > 0$ may also stabilize the transient deuterium distribution which is characterized by the pronounced domains with $\partial f_{D+}/\partial v_\perp > 0$. Thus, for frequencies $\omega/2\pi \approx l_i\,\omega_{ci} = l_b\,\omega_{cb}$, the instability driven by the transient deuterium beam particle distribution may be strongly stabilized by the hydrogen beam particle distribution as confirmed by the ICE signals of Figure 45. It must be mentioned in this context, that a fundamental problem of the ICE measurements is the unkown domain within the plasma from where the ICE originates.

Finally, a strong indication of preferential ion heating and related to this enhanced slowing down of the beam particles after switch on the injection is the central ion temperature increase in Figure 46. In this series of discharges maintained by 3 neutral beam injectors, a 4th injector was superposed resulting in a fast increase of the central ion temperature whereas the electron temperature remains nearly unaffected for the time immediately after switch on the 4th injector. As fast beam particles are mainly slowed down by collisions with electrons, with only collisional interaction one would expect strong electron temperature increase first and after sufficient slowing down the ion heating. However, ion and electron heating are vice versa. We must conclude preferential ion heating due to strong instabilites of low harmonic ion Bernstein modes which are nearly undamped by the electrons. Furthermore, we can estimate the ion heating efficiency after switch on the 4th injector by means of the ion temperature increase; the electron temperature increase results from both the collisional energy transfer from the hotter ions as well as the direct electron heating after the injection becomes stationary.

For estimating the ion heating after switch on the 4th injector, we use the ion temperature increase, ΔT_i, and assume the electron temperature as well as the plasma density being constant, furthermore, we neglect the impurities and modified transport effects. Then, the increase of central energy density is approximately given by: $3/2\; n_e\, dT_i/dt \approx 0.45\; W/cm^3$. From the diamagnetic loop signal, we find the absorbed heating power to be approximately $35\; kW$. With an effective plasma radius of $5.5\; cm$, we get for the absorbed power assuming only perpendicular energy increase $0.3\; W/cm^3$ and assuming isotropic energy increase $0.45\; W/cm^3$, respectively. The beam power absorbed (from the beam line data and calorimetric estimation of the shine through) is of about $75\; kW$, with the same assumptions we get an absorbed power density of about $0.6\; W/cm^3$, this value gives an upper limit as the fast orbit losses are not taken into account. These estimates yield rather good agreement with the assumption of preferential ion heating leading to the strong temperature increase immediately after switch on the 4th injector. Within the accuracy of these estimates we cannot decide between isotropic or mainly perpendicular energy increase in the ion distribution. However, the ion temperature increase measured indicates that the internal energy increase is mainly isotropic. Consequently, the slowing down mechanism immediately after switch on the neutral beam injection is expected to be dominated by ion Bernstein mode instabilities connected with preferential heating of the thermal ions.

To sum up shortly the experimental results related to the slowing down mechanism of the neutral beam injection, we found mainly collisional slowing down for both the stationary phase as well as after switch off the injection with heating efficiencies for electrons and ions determined by the Coulomb interaction. For a short transient phase after switch on the neutral beam injection, we found mainly ion heating related to non-collisional slowing down of the fast beam particles. These results are in agreement with the theoretical predictions based on the stability analysis of the various ion cyclotron modes leading to instability of the ion Bernstein modes in the very low harmonic range connected with preferential ion heating.

Appendix

A. Contribution of the Beam Ion Distribution to ε_{ij}

The contribution of arbitrary distribution functions to the dielectric tensor cannot be given in a simple analytical form. The general formulation includes the Doppler shift resonances between the cyclotron harmonics and the parallel velocities of the particles ($\omega - l\omega_c - k_\parallel v_\parallel \approx 0$) in form of a singularity. Here, the $v_\parallel$-integration must be understood as a Hilbert integral transform (complex valued) with respect to this singularity. Consequently, a straight forward numerical evaluation of these integrals is unqualified for the stability analysis. In this appendix, we describe shortly a convolution formalism based on the contribution of a δ-δ distribution function to the dielectric tensor. This formalism is qualified to treat arbitrary distribution functions.

The distribution function of the slowed down beam particles, $f_b(v_\parallel, v_\perp)$, is given numerically (see Appendix B). Therefore, the beam contribution ε_{ij}^b to the dielectric tensor ε_{ij} is calculated by means of a convolution formalism. Let $f_{\delta\delta}$ be a normalized double δ-distribuition function

$$f_{\delta\delta}(v_\parallel, v_\perp) = \frac{1}{2\pi v_\perp} \cdot \delta(v_\perp - u_\perp) \cdot \delta(v_\parallel - u_\parallel) .$$

Then, $\varepsilon_{ij}^{\delta\delta}$ (s. eq. 5) is the contribution of $f_{\delta\delta}$ to the dielectric tensor. The convolution of the dielectric tensor elements $\varepsilon_{ij}^{\delta\delta}(u_\parallel, u_\perp)$ (normalized with regard to the beam ion density due to $f_{\delta\delta}$ defined above) with the beam particle distribution function $f_b(u_\parallel, u_\perp)$ yields the beam contribution

$$\varepsilon_{ij}^b = 2\pi \int_{-\infty}^{\infty} \int_{0}^{\infty} \varepsilon_{ij}^{\delta\delta} \cdot f_b \cdot u_\perp \, du_\perp \, du_\parallel . \qquad (A1)$$

In the ε_{ij}-tensor elements of eq. (5), the different terms with respect to the $u_\parallel$ dependence are combined. Then, in the velocity space mesh of the beam distribution function, f_b, the $u_\perp$-integration of these combined terms is numerically straight forward and yields terms $g^{(\nu)}(u_\parallel)$ where the index ν corresponds to terms related to $Y_{l_b}^\nu$ ($\nu = 0, 1, 2$). The $u_\parallel$-integration of the nonresonant terms ($\nu = 0$) is carried out directly. The remaining $u_\parallel$-integration in eq. (A1) of the terms with $\nu \geq 1$ connected with the Doppler shifted cyclotron resonance condition may be written in the form

$$G^{(\nu)} = \int_{-\infty}^{\infty} \frac{g^{(\nu)}(u_\parallel) \, du_\parallel}{(k_\parallel u_\parallel - \omega + l_i \omega_{ci})^\nu} \qquad \text{for} \quad \nu = 1, 2, 3 . \qquad (A2)$$

The terms $G^{(\nu)}$ with $\nu = 3$ are required for the Cauchy rootfinder routine with the derivative of the dielectric function $dD/d\omega$ included.

A coordinate transform $w_{\|} = (u_{\|} - u_{\|}^{*})/\sigma_{\|}$ is used where $u_{\|}^{*}$ and $\sigma_{\|}$ are the mean values and standard deviations, respectively, of the function $g^{(1)}(u_{\|})$ which is most important for the beam ion contribution ε_{ij}^{b}. By means of this transform, Hermite polynomial expansion is applied to the functions $g^{(\nu)}$:

$$g^{(\nu)}(w_{\|}) = \sum_{n=0}^{N} g_n^{(\nu)} \cdot H_n(w_{\|})\, e^{-w_{\|}^2} . \qquad (A3)$$

Using the recurrence relation for Hermite polynomials, coefficient sorting in equation (A3) leads to

$$g^{(\nu)}(w_{\|}) = \sum_{n=0}^{N} \hat{g}_n^{(\nu)} \cdot w_{\|}^{n} \cdot e^{-w_{\|}^2} . \qquad (A4)$$

With this power expansion with respect to $w_{\|}$, equation (A2) can be expressed in the following form:

$$G^{(\nu)}(\alpha) = \frac{\sigma_{\|}}{(k_{\|}\sigma_{\|})^{\nu}} \sum_{n=0}^{N} \hat{g}_n^{(\nu)} \cdot G_n^{(\nu)}(\alpha) , \qquad (A5)$$

$$\text{with} \qquad G_n^{(\nu)} = \int_{-\infty}^{\infty} \frac{w_{\|}^{n} \cdot e^{-w_{\|}^2}\, dw_{\|}}{(w_{\|} - \alpha)^{\nu}}$$

$$\text{and} \qquad \alpha = \frac{\omega - l_i \omega_{ci} - k_{\|} u_{\|}^{*}}{k_{\|}\sigma_{\|}} .$$

The Hilbert integral transformed moments of the Gaussian, $G_n^{(\nu)}(\alpha)$, are calculated by means of the recurrence relation

$$G_n^{(\nu)}(\alpha) = G_{n-1}^{(\nu-1)}(\alpha) + \alpha \cdot G_{n-1}^{(\nu)}(\alpha) , \qquad (A6)$$

$$\text{with} \qquad G_{2m}^{(0)} = \Gamma(2m + \frac{1}{2}) ; \qquad G_{2m+1}^{(0)} = 0$$

$$\text{and} \qquad G_0^{(1)} = \sqrt{\pi}\, Z(\alpha) ; \qquad G_0^{(\nu)} = \frac{\sqrt{\pi}}{\nu - 1} \frac{d^{\nu-1}}{d\alpha^{\nu-1}} Z(\alpha) ;$$

where $Z(\alpha)$ is the plasma dispersion function which is the Hilbert transform of the Gaussian /22/. For large complex arguments α, however, an asymptotic expansion may be used instead of equation (A6):

$$G_n^{(1)}(\alpha) = -\sum_{m=0}^{\infty} \frac{1}{\alpha^{m+1}} \cdot G_{n+m}^{(0)}(\alpha) \; + \; i\pi\, \delta_{\alpha}\, \alpha^{n}\, e^{-\alpha^2} \qquad (A7)$$

$$\text{with} \qquad \delta_{\alpha} = \left\{ \begin{array}{lll} 0 & \text{for} & \Im\mathrm{m}(\alpha) > 0 \\ 1 & \text{for} & \Im\mathrm{m}(\alpha) = 0 \\ 2 & \text{for} & \Im\mathrm{m}(\alpha) < 0 \end{array} \right\}$$

and for the higher order moments

$$G_n^{(\nu)}(\alpha) = \frac{1}{\nu - 1} \frac{d}{d\alpha} G_n^{(\nu-1)}(\alpha) \,. \qquad (A8)$$

In the case of nearly perpendicular neutral beam injection, the ε_{11}^b-tensor element is the most important term in the dielectric function with respect to instabilities driven by the beam. In the calculations described in this report, we included only the ε_{11}^b and ε_{22}^b tensor elements of the slowing down distribution function estimated by Monte Carlo simulation. In the numerical computations, a maximum order of $N = 50$ was used in the Hermite expansion of equation (A5).

B. Monte Carlo Calculation of the Beam Ion Distribution

For the linear stability analysis of the nearly perpendicular neutral beam injection (NBI), we estimate the slowing down distribution function of the beam ions, f_b, using a simplified model. We neglect both the configuation space dependence and the transport. However, orbit losses of fast particles trapped in a magnetic ripple can be included. Furthermore, for low beam densities, n_b, the direct interaction of the high energetic beam particles can be neglected and the slowing down of the beam particles due to the friction with the background plasma is described in a test particle picture (see /17/ for further details).

Based on the Fokker-Planck equation for axisymmetric distribution functions in case of Coulomb collisions (see Ref. /23/), the collision term in the Fokker-Planck equation for isotropic distributions of the background plasma is given in the simplified form:

$$\frac{\partial f_b}{\partial t} = \frac{\Gamma_b}{v^2} \cdot \left[\frac{\partial}{\partial v} \left(A_1^M f_b \right) + \frac{1}{2} \frac{\partial^2}{\partial v^2} \left(A_2^M f_b \right) + B^M \frac{\partial}{\partial p} \left(1 - p^2 \right) \frac{\partial}{\partial p} f_b \right] + S_b \,. \qquad (B1)$$

Here, f_b is the distribution function of the slowed down beam ions, v the absolute value of the velocity, p the pitch, $v_\parallel / v$, and S_b the particle source and loss term,

$$\Gamma_b = \frac{\ln \Lambda}{4\pi} \cdot \left(\frac{Z_b e^2}{\epsilon_0 m_b} \right)^2 ,$$

with $\ln \Lambda$ being the Coulomb logarithm, Z_b the charge number, and m_b the mass of the beam ions. The coefficient functions A_1^M, A_2^M and B^M in eq. (B1) are defined by deriva-

tives of the Rosenbluth potentials h_b^M and g^M which depend only on v for isotropic background distributions:

$$A_1^M = -v^2 \frac{d}{dv} h_b^M - \frac{d}{dv} g^M$$
$$A_2^M = v^2 \frac{d^2}{dv^2} g^M$$
$$B^M = \frac{1}{2v} \frac{d}{dv} g^M. \qquad (B2)$$

For the distribution functions of all plasma species being isotropic Maxwellians, the Rosenbluth potentials can be calculated analytically:

$$h_b^M = \frac{1}{v} \sum_\beta n_\beta Z_\beta^2 \, (1 + \frac{m_b}{m_\beta}) \, \mathrm{erf}(v_\beta)$$
$$g^M = \sum_\beta n_\beta Z_\beta^2 \, \{(1 + \frac{1}{2v_\beta^2}) \, \mathrm{erf}(v_\beta) + \frac{v_{th_\beta}}{\sqrt{\pi}} \exp(-v_\beta^2)\}$$

with $v_\beta = v/v_{th_\beta}$ where v_{th_β} is the thermal velocity of the particle species β. Then, the coefficient functions of the Fokker-Planck equation defined in equation (B2) are given by

$$A_1^M = \sum_\beta n_\beta Z_\beta^2 \, \{(1 + \frac{m_b}{m_\beta}) \, \eta(v_\beta) - \overline{\eta}(v_\beta)\}$$
$$A_2^M = \sum_\beta n_\beta Z_\beta^2 \, \frac{v_{th_\beta}}{v_\beta} \, \eta(v_\beta)$$
$$B^M = \frac{1}{2v} \sum_\beta n_\beta Z_\beta^2 \, \overline{\eta}(v_\beta) \qquad (B3)$$

with
$$\eta(x) = \mathrm{erf}(x) - \frac{2}{\sqrt{\pi}} x \, \mathrm{e}^{-x^2}$$
$$\overline{\eta}(x) = \mathrm{erf}(x) - \frac{1}{2x^2} \eta(x).$$

For the Monte Carlo collision operator, the Fokker-Planck equation (B1) is interpreted as an initial value problem for the probability distribution, f_b, of the test (or simulation) particles. At $t = 0$, the distribution function, f_b, is a δ-function in velocity space and for small time increments, Δt, the probability distribution, f_b, remains highly localized. Then, the collision operator is approximated by a Gaussian random process for which the mean value and the standard deviation is defined by the moment equations resulting from the Fokker-Planck equation (B1). However, the particle source and loss term, S_b, is disregarded in this context. The corresponding expectation values up to second order are defined by the moment equations:

$$\frac{d}{d\tau} \langle v \rangle_b = - \left\langle \frac{A_1^M}{v^2} \right\rangle_b$$

$$\frac{d}{d\tau}\langle p\rangle_b = -\left\langle p\frac{B^M}{v^2}\right\rangle_b$$
$$\frac{d}{d\tau}\left\{\langle v^2\rangle_b - \langle v\rangle_b{}^2\right\} = \left\langle \frac{A_2^M}{v^2}\right\rangle_b$$
$$\frac{d}{d\tau}\left\{\langle p^2\rangle_b - \langle p\rangle_b{}^2\right\} = \left\langle (1-p^2)\frac{B^M}{v^2}\right\rangle_b , \qquad (B4)$$

with the abbreviation $\tau = \Gamma_b \cdot \Delta t$. Here, the moments $\langle v^l p^k\rangle_b$ are defined by

$$\langle v^l p^k\rangle_b = \frac{2\pi}{n_b}\int_0^\infty\int_{-1}^{1} v^l p^k\, f_b\, v^2\, dp\, dv.$$

Since the distribution f_b is highly localized for small time increments Δt, the moments on the right hand side of equations (B4) can be replaced by use of the initial values v_i, p_i of the simulation particle i. With the initial values of all simulation particles, the moment equations are integrated for the small time step Δt. The mean values, $\langle v\rangle_b$ and $\langle p\rangle_b$, and the square of the standard deviations, $\langle v^2\rangle_b - \langle v\rangle_b{}^2$ and $\langle p^2\rangle_b - \langle p\rangle_b{}^2$, define the Gaussian random processes (in v and p) used for the simulation.

The random change in velocity and pitch of the simulation particles by the Monte Carlo collision operator describes the diffusive nature of the slowing down process. Repeating this collision process, the distribution of the simulation particles will develop into an isotropic Maxwellian for an isothermal background plasma without source and loss terms.

The generation of the simulation (beam) particles is approximated to the neutral beam injection conditions in the W VII-A stellarator with mainly 3 energy components:

$$S_b = \frac{1}{\sqrt{2\pi}\,\sigma_b}\exp\left(-\frac{(p-p_b)^2}{2\,\sigma_b^2}\right)\cdot\sum_\nu w_\nu\cdot\frac{1}{v_\nu^2}\,\delta(v-v_\nu) \qquad (B5)$$

with the mean pitch of the NBI, p_b (= 0.1, corresponding to 84° injection angle), and the standard deviation, σ_b (= 0.035, corresonding to the divergence of the beam lines of $\pm 2^\circ$). v_ν are the velocities corresponding to the different injection energies with source strengths w_ν. For 27 kV voltage in W VII-A, the beam composition is assumed to be 21% : 32% : 47% for particles with 27, 13.5 and 9 keV energy.

For simulating the switch on phase of the neutral beam injection, simulation particles are generated corresponding to the source term (eq. B5) for each time step. The simulation particles are distributed in velocity space due to the Monte Carlo collision operator and the distribution function is evaluated by means of the number of simulation particles in the velocity space mesh. The transient distribution functions are estimated using up to 50,000 simulation particles.

For estimating the slowing down distribution function for stationary conditions, thermalized simulation particles with an energy less than T_i are replaced corresponding to the source term S_b of eq. (B5). Time averaging within the stationary phase of the simulation improves the statistical accuracy significantly, so that only several thousend simulation particles are used for the calculation of the stationary beam ion distribution functions. Furthermore, the thermal loss region in the distribution function is filled up by means of a simple fit formalism in order to avoid additional gradients in the distribution function which also may drive instabilities (see Chapter III, Figures 5 to 8).

The loss of helically trapped particles drifting out of the plasma can be included in the Monte Carlo simulation in a simplified model. Let p_{LC} be the average pitch of the loss cone. Then, simulation particles with $|p| < p_{LC}$ repesent helically trapped particles and the loss term, S_b, which acts on these particles is simulated by a random process corresponding to the ratio of the Monte Carlo time step to the average drift time which is related to the energy of the simulation particles (due to the ∇B-drift). For stationary conditions, the particle confinement time can be estimated within the simulation. If this particle confinement time is of the order of the average slowing down time, the distribution function of the beam particles is strongly influenced by the loss cone effect (see Chapter III, Figures 7 and 8).

C. Estimation of $k_\perp$ for Maximum Instability $\Im\mathrm{m}\{\omega\}$

The analyzed beam distribution functions have only small domains in the velocity space which can drive ion cyclotron instabilities. These domains in $\underline{v}$-space, generally with $\partial f_b/\partial v_\perp > 0$, are related to domains in $\underline{k}$-space for which the instability, $\Im\mathrm{m}\{\omega\}$, becomes maximum. As the domains with $\partial f_b/\partial v_\perp > 0$ may be small, especially for the stationary slowing down distributions, the domains in $\underline{k}$-space are also small. For the nearly perpendicular neutral beam injection, the gradients with respect to $v_\perp$ are of most interest; these gradients are related to a relative narrow range in $k_\perp$. In the extreme case of a beam distribution modeled by a $\delta\delta$-function, the relation of $v_\perp$ and $k_\perp$ is very similar to a resonance condition for the different cyclotron harmonics.

However, it is not practical to find all roots of the dispersion relation $D(\omega, k_\parallel, k_\perp)$ in the whole $\underline{k}$-space numerically in order to estimate the different ranges in $k_\perp$ with $\Im\mathrm{m}\{\omega\}$ being maximum. A relative accurate estimation of the $k_\perp$-resonances for the different cyclotron harmonics was deduced directly from the simplified dispersion relation of equation (7), where the contribution of the beam ion distribution function to the ε_{11} dielectric tensor element may cause instability. From this simplified form of the dispersion

relation (eq. 7), the imaginary part of ε_{11} is estimated:

$$\Im\mathrm{m}\{\varepsilon_{11}\} + \frac{k_\parallel^2}{k_\perp^2} \cdot \frac{\Im\mathrm{m}\{\varepsilon_{33}\}}{\left|1 - \frac{\omega^2}{c^2 k^2}\,\varepsilon_{33}\right|^2} = 0\,. \qquad (C1)$$

$$\text{with} \qquad \varepsilon_{33} \simeq -\Big(\frac{\omega_{pe}}{\omega}\, x_0^e\Big)^2 \cdot Z'(x_0^e)\;; \qquad x_0^e = \frac{\omega}{k_\parallel v_e}\,.$$

Since $\Im\mathrm{m}\{x_0^e\} \approx 0$, the imaginary part of ε_{33} is positive ($\Im\mathrm{m}\{Z'(x_0^e)\} > 0$). The imaginary part of the thermal plasma contribution to ε_{11} is determined by the ions (see eq. 3):

$$\Im\mathrm{m}\{\varepsilon_{11}^p\} \simeq \Big(\frac{\omega_{pi}}{\omega_{ci}}\Big)^2 \frac{1}{b}\, e^{-b}\, I_{l_i}(b)\, \Re\mathrm{e}\{x_0^i\} \cdot \Im\mathrm{m}\{Z(x_l^i)\}\;; \qquad x_l^i = \frac{\omega - l_i\omega_{ci}}{k_\parallel v_i}\,.$$

For $\Im\mathrm{m}\{\omega\}$ not too negative, the imaginary part of the thermal plasma contribution to ε_{11} is also positve ($\Im\mathrm{m}\{Z(x_l^i)\} > 0$). Consequently, the beam contribution $\Im\mathrm{m}\{\varepsilon_{11}^b\}$ must be negative to result in nearly undamped modes or instability. Then, our problem is to minimize $\Im\mathrm{m}\{\varepsilon_{11}^b\}$ with respect to $k_\perp$.

The contribution of a normalized δ-δ distribution function, $\varepsilon_{11}^{\delta\delta}$, to the dielectric tensor is basis of the convolution formalism (see Appendix A) for estimating the ε_{11}^b-element. From eq. (5), the imaginary part of $\varepsilon_{11}^{\delta\delta}$ is given by

$$\Im\mathrm{m}\{\varepsilon_{11}^{\delta\delta}\} \simeq -4l^2\Big(\frac{\omega_{pb}}{\omega_{cb}}\Big)^2 \Big\{\frac{1}{a}\, J_{l_b}(a)\, J'_{l_b}(a) + 2\Big(\frac{k_\parallel}{k_\perp}\Big)^2 J_{l_b}^2(a)\, \Re\mathrm{e}\{Y_{l_b}\}\Big\} \cdot \Im\mathrm{m}\{Y_{l_b}\} \qquad (C2)$$

$$\text{with} \qquad l_b \approx \frac{\Re\mathrm{e}\{\omega\}}{\omega_{cb}}; \qquad a = \frac{k_\perp u_\perp}{\omega_{cb}}; \qquad Y_{l_b} = \frac{1}{2l_b}\,\frac{\omega_{cb}}{\omega - k_\parallel u_\parallel - l_b\omega_{cb}}\,.$$

For nearly perpendicular wave propagation ($k_\parallel \ll k_\perp$), we can neglect the second order Y_{l_b}-term in eq. (C2). We get

$$\Im\mathrm{m}\{\varepsilon_{11}^{\delta\delta}\} \simeq a_{11} \cdot \frac{\omega_{cb} \cdot \Im\mathrm{m}\{\omega\}}{\left|\omega - k_\parallel u_\parallel - l_b\omega_{cb}\right|^2} \qquad \text{with} \qquad a_{11} = \frac{2l_b}{a}\Big(\frac{\omega_{pb}}{\omega_{cb}}\Big)^2 J_{l_b}(a)\, J'_{l_b}(a)\,. \qquad (C3)$$

For the estimation of the $k_\perp$ resonance conditions, we can neglect the $u_\parallel$-dependence in eq. (C3). Then, in connection with the convolution integral (Appendix A, eq. A1), the minimization of $\Im\mathrm{m}\{\varepsilon_{11}^b\}$ is equivalent to the minimization of the term:

$$A_{11}(k_\perp) = 2\pi \int_{-\infty}^{\infty}\int_{0}^{\infty} a_{11}(k_\perp, u_\perp) \cdot f_b \cdot u_\perp\, du_\perp\, du_\parallel\,. \qquad (C4)$$

This integration is carried out numerically in the velocity space mesh of the beam ion distribution function and the minima of A_{11} are calculated. Generally, the $k_\perp$ values of these minima A_{11} argee very well with those found for the maximum growth rates, $\Im\mathrm{m}\{\omega\}$,

based on the roots of the dispersion relation; the $k_{\|}$-dependence of these $k_{\perp}$ values was but small.

Due to the periodicity of $J_{l_b}(a)\,J'_{l_b}(a)$ in eq. (C4), we get also harmonics of ion cyclotron instability with respect to $k_{\perp}$ for $A_{11}(k_{\perp})$ being sufficiently negative. However, the higher harmonics in $k_{\perp}$ result in much less instability, $|A_{11}|$ decreases strongly for $k_{\perp}$ being large. Furthermore, the 3 peaks in the slowing down distribution function corresponding to the 3 injection energies of the beam can be in phase in $k_{\perp}$ (or out of phase) for the different ion cyclotron harmonics l_i.

D. Examples of Plasma Modes

In this part, ion cyclotron modes in a pure Maxwellian plasma without any beam contribution will be shortly discussed. Here, the plasma modes are defined by the roots of the dispersion relation $D(\omega, k_{\|}, k_{\perp}) = 0$ (see eqs. 1 and 2) based on the full dielectric tensor ε^p_{ij} given by eq. (3) which is estimated numerically. However, the simplified form of the dispersion relation (eq. 7) may be used to classify the ion cyclotron modes. Furthermore, we restrict the classification to small values of $k_{\|}$ for which the electron Landau damping becomes comparable with the ion cyclotron damping; this leads to $|\omega| \gg k_{\|} v_e$. The asymptotic expansion of the plasma dispersion function in the ε^p_{33} tensor element, which describes the electron Landau damping, leads to $\varepsilon^p_{33} \simeq -\omega^2_{pe}/\omega^2$. Then, the simplified dispersion relation is given by

$$D \;\simeq\; \varepsilon_{11}\Big(1 + \frac{\omega^2_{pe}}{c^2 k^2}\Big) - \frac{k^2_{\|}}{k^2}\,\frac{\omega^2_{pe}}{\omega^2} \;=\; 0. \qquad (D1)$$

This form of dispersion relation is basis of the mode classification for the different ion cyclotron harmonics.

Low and intermediate hamonics:

For low and intermediate ion cyclotron harmonics l_i, the ε^p_{11} tensor element cannot be expanded with respect to the arguments of the Bessel functions, $b = k^2_{\perp} v^2_i / 2\omega^2_{ci}$. Therefore, ε^p_{11} must be used in the form

$$\varepsilon^p_{11} \simeq \Big(\frac{\omega_{pi}}{\omega_{ci}}\Big)^2 \frac{1}{b}\Big\{S_1(b) + e^{-b}\, I_{l_i}(b)\;\frac{\omega}{k_{\|} v_i}\, Z\Big(\frac{\omega - l_i\omega_{ci}}{k_{\|} v_i}\Big)\Big\}. \qquad (D2)$$

where $S_1(b)$ is defined in eq. (3). For sufficiently small values of $k_{\|}$, we can neglect the electron Landau damping. Then, the dispersion relation (D1) becomes $\varepsilon^p_{11} \simeq 0$. Two

different type of roots can exist: (i) a class of strongly damped modes defined by the bounded different roots of the plasma dispersion function

$$\lim_{k_\parallel \to 0} Z\left(\frac{\omega - l_i \omega_{ci}}{k_\parallel v_i}\right) = 0 \qquad (D3)$$

and (ii) a weakly damped mode, the ion Bernstein mode, which is related to the asymptotic expansion of the plasma dispersion function. The strongly damped modes related to the infinte number of roots of the plasma dispersion function are characterized by strong ion cyclotron damping since the imaginary part of ε_{11}^p is mainly given by the plasma dispersion function which describes the resonant contribution of the cyclotron harmonics. Due to the symmetry relation $Z(\overline{z}) = -\overline{Z(-z)}$, a pair of modes exists with the same damping but with positive and negative frequency shift (see the modes (2) and (3) in Fig. D1). For small $k_\parallel$, these modes are nearly independent on $k_\perp$ and the harmonic number l_i; they are nearly undisturbed by a small beam contribution to the ion distribution function. Consequently, this class of strongly damped modes is unimportant for the stability analysis of the neutral beam injection. However, similar modes only related to the beam contribution may appear for simple models of the beam particle distribution function.

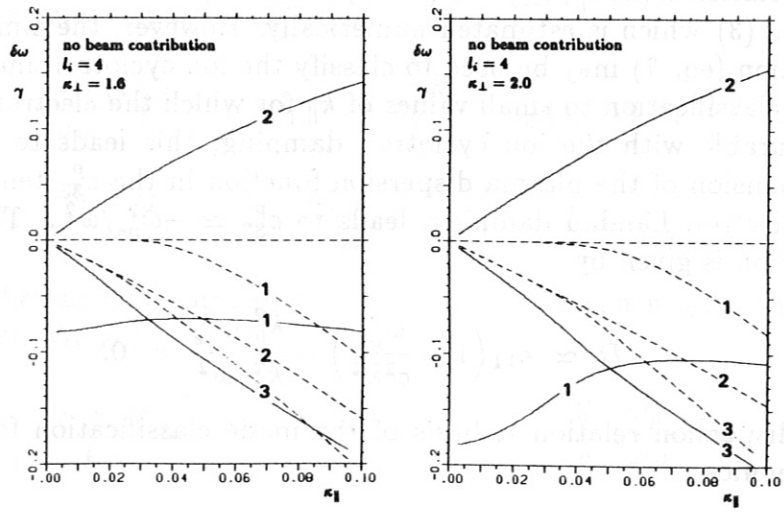

Fig. D1 *Ion cyclotron modes (4th harmonic l_i) in a pure Maxwellian plasma: the normalized frequency shift $\delta\omega = \Re\mathrm{e}\{\omega\}/\omega_{ci} - l_i$ (solid lines) and the normalized damping $\gamma = \Im\mathrm{m}\{\omega\}/\omega_{ci}$ (broken lines) vs. the normalized parallel wave number $\kappa_\parallel = k_\parallel v_i/\omega_{ci}$ for fixed perpendicular wave number $\kappa_\perp$. The mode (1) is a nearly undamped ion Bernstein mode (eq. D4), the modes (2) and (3) are strongly damped and related to the roots of the plasma dispersion function (eq. D3). Plasma parameters: $B = 3.2\ T$; $n_e = 5 \cdot 10^{13}\ cm^{-3}$; $T_e = 600\ eV$; $T_i = 1\ keV$.*

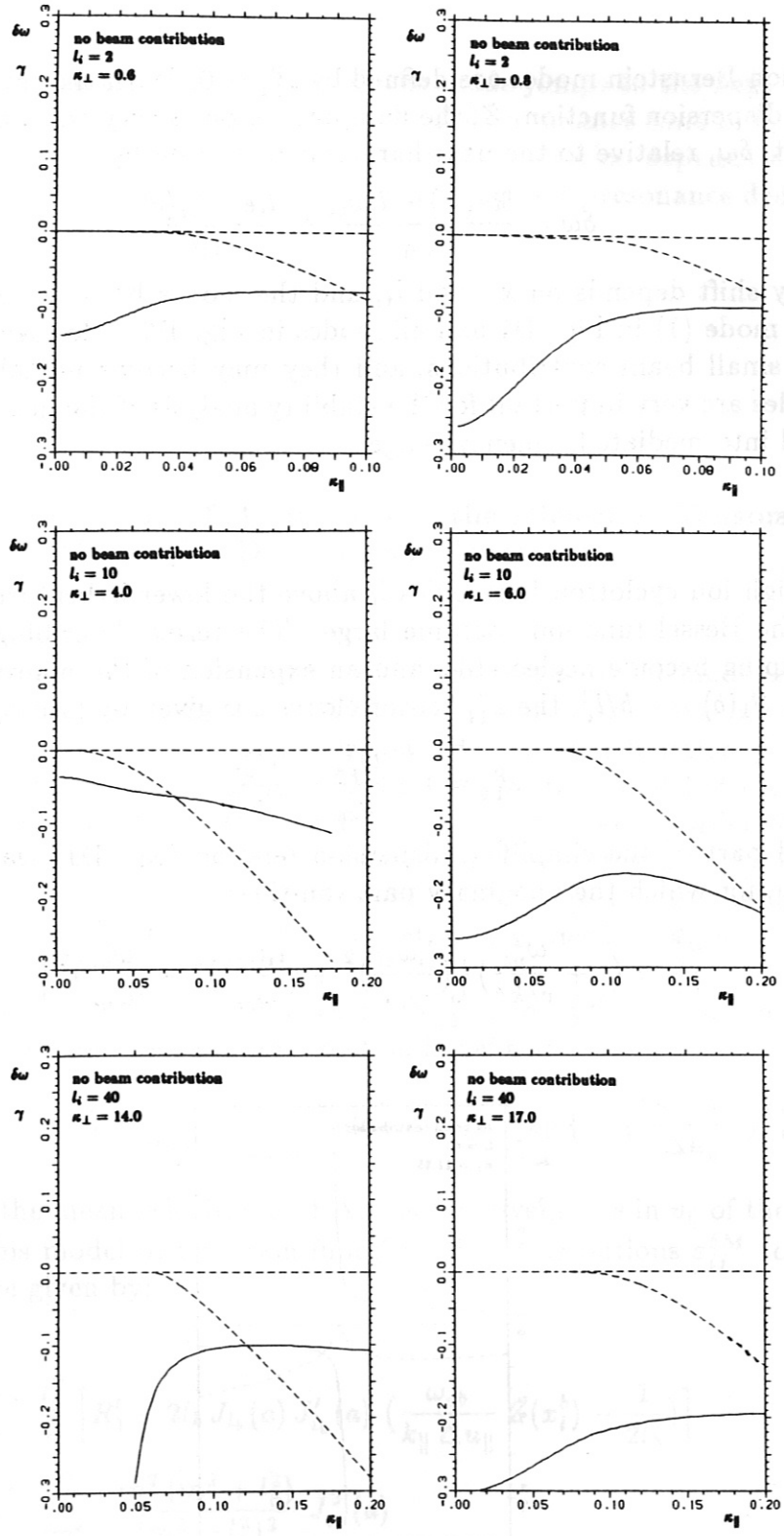

Fig. D2 *Ion Bernstein modes in a pure Maxwellian plasma: the normalized frequency shift $\delta\omega$ (solid line) and the normalized damping γ (broken line) vs. normalized parallel wave number $\kappa_{\|}$ for fixed $k_\perp$ (plasma parameters see Fig. D1).*

Also the ion Bernstein modes are defined by $\varepsilon_{11}^p \simeq 0$. With the asymptotic expansion of the plasma dispersion function, Z, the damping becomes very small and the normalized frequency shift, $\delta\omega$, relative to the next harmonic l_i is given by

$$\delta\omega = \frac{\Re e\{\omega\} - l_i\omega_{ci}}{\omega_{ci}} \simeq \frac{l_i e^{-b} I_{l_i}(b)}{S_1(b)}. \qquad (D4)$$

This frequency shift depends on $k_\perp$ and l_i, and the modes become strongly damped for larger $k_\parallel$ (the mode (1) in Fig. D1 and all modes in Fig. D2). However, these modes are influenced by small beam contributions, and they may become unstable. Thus, the ion Bernstein modes are very important for the stability analysis of the neutral beam injection in the low and intermediate frequency range.

High hamonics:

For the high ion cyclotron harmonics l_i above the lower hybrid frequency, the arguments, b, of the Bessel functions become large. The terms describing the resonant ion cyclotron damping become neglectable, and an expansion of the nonresonant terms may be used. With $S_1(b) \approx -b/l_i^2$, the ε_{11}^p tensor element is given by (see eq. 8)

$$\varepsilon_{11}^p \approx 1 + \frac{\omega_{pe}^2}{\omega_{ce}^2} - \frac{\omega_{pi}^2}{l_i^2\omega_{ci}^2}.$$

Then, the real part of the simplified dispersion relation (eq. D1) leads to a resonance condition in $k_\parallel$, for which the imaginary part vanishes:

$$\frac{k_\parallel^2}{k^2} \simeq \left(1 + \frac{\omega_{pe}^2}{c^2k^2}\right)\left\{\left(\frac{l_i\omega_{ci}}{\omega_{pe}}\right)^2 + \left(\frac{l_i\omega_{ci}}{\omega_{ce}}\right)^2 - \left(\frac{\omega_{pi}}{\omega_{pe}}\right)^2\right\}. \qquad (D5)$$

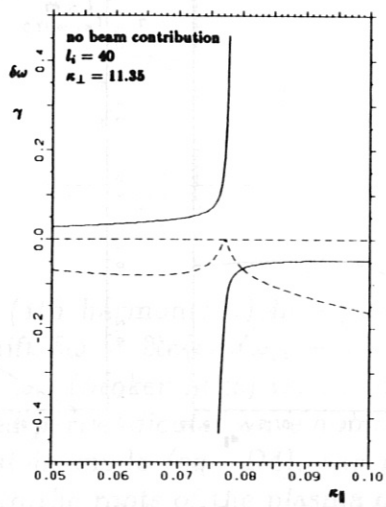

Fig. D3 *The resonance in $k_\parallel$ for a pure Maxwellian plasma: the normalized frequency shift $\delta\omega$ (solid line) and the normalized damping γ (broken line) vs. normalized parallel wave number $\kappa_\parallel$ for fixed $k_\perp$ (plasma parameters see Fig. D1).*

At this resonance in $k_{\|}$, the frequency of the mode jumps to the next harmonic (see Fig. D3), whereas the modes become undamped. This resonance zone in $k_{\|}$ becomes very narrow for the higher harmonics, however, the mode behavior depends on small beam contributions. Very strong instability may appear near the $k_{\|}$-resonance dedending on the values of $k_{\perp}$ (see Appendix C and F).

E. Contribution of Beam Ions to the Dielectric Tensor ε_{ij} for *δ-Maxwellian* Distribution Functions

The contribution of beam particles to the dielectric tensor ε_{ij} modeled by a δ-δ distribution function is given in Chapter II. These $\varepsilon_{ij}^{\delta\delta}$ elements are basis of the convolution formalism (s. Appendix A) of the slowing down distribution function f_b calculated by means of Monte Carlo simulation (Appendix B). As a further model of the slowing down distribution function, a *δ-Maxwellian* function, $f_{\delta M}$, was used in order to compare the instabilities and the influence on the ion cyclotron modes, especially the $k_{\|}$ dependence due to the Doppler shift of the resonance condition. In Appendic F, the influence of the form of the distribution functions on the ion cyclotron modes is analyzed.

For these investigations, we disregard the $\varepsilon_{22}^{\delta M}$ and $\varepsilon_{23}^{\delta M}$ elements of the dielectric tensor. The *δ-Maxwellian* distribution function is defined by

$$f_{\delta M}(v_{\|}, v_{\perp}) = \frac{n_b}{2\pi^{\frac{3}{2}}\, v_{\perp}\, \Delta u_{\|}} \cdot \delta(v_{\perp} - u_{\perp}) \cdot \exp\Big\{ - \Big(\frac{v_{\|} - u_{\|}}{\Delta u_{\|}}\Big)^2 \Big\} \qquad (E1)$$

where $u_{\perp}$, $u_{\|}$ are the mean velocities and $\Delta u_{\|}$ is the divergence in $v_{\|}$ of the neutral beam injection. With this model distribution function, the contributions $\varepsilon_{ij}^{\delta M}$ to the dielectric tensor elements are given by:

$$\begin{aligned}
\varepsilon_{11}^{\delta M} = & -\Big(\frac{\omega_{pb}}{\omega}\Big)^2 \Bigg\{ -\frac{l_b^2}{a}\Big[R_1' + 2l_b\, J_{l_b}(a)\, J_{l_b}'(a)\, \Big(\frac{\omega_{cb}}{k_{\|}\, \Delta u_{\|}}\, Z(x_l^b) - \frac{1}{2l_b}\Big)\Big] \\
& + 2\Big(\frac{k_{\|}}{k_{\perp}}\Big)^2 \sum_{m=1,\neq l_b}^{\infty} \frac{m^2\,(m^2 + l_b^2)}{(m^2 - l_b^2)^2}\, J_m^2(a) \\
& + \Big(\frac{k_{\|}}{k_{\perp}}\Big)^2 l_b^2 J_{l_b}(a) \Big[J_{l_b}(a) + \Big(\frac{\Delta u_{\|}}{u_{\perp}}\Big)^2 a\, J_{l_b}'(a)\Big] \Big(\Big(\frac{\omega_{cb}}{k_{\|}\, \Delta u_{\|}}\Big)^2 Z'(x_l^b) + \frac{1}{4l_b^2}\Big) \Bigg\} \\
\varepsilon_{33}^{\delta M} = & -\Big(\frac{\omega_{pb}}{\omega}\Big)^2 \Bigg\{ 1 + 2\frac{k_{\|}\, u_{\|}}{l_b \omega_{cb}}\Big(1 - R_1 - \frac{3}{2} J_{l_b}^2(a)\Big) + J_{l_b}^2(a) \Big(\Big(\frac{\omega - l_b \omega_{cb}}{k_{\|}\, \Delta u_{\|}}\Big)^2 Z'(x_l^b) - 1\Big) \Bigg\}
\end{aligned}$$

$$\varepsilon_{12}^{\delta M} = i\,(\frac{\omega_{pb}}{\omega})^2 \Big\{ 2l_b \sum_{m=1,\neq l_b}^{\infty} \frac{m^2}{m^2-l_b^2} \Big[J'_m(a)\,(J'_m(a) + \frac{1}{a} J_m(a)) + J_m(a)\,J''_m(a) \Big]$$

$$- 4l_b\,(\frac{k_\parallel}{k_\perp})^2\, a \sum_{m=1,\neq l_b}^{\infty} \frac{m^2}{(m^2-l_b^2)^2}\, J_m(a)\,J'_m(a)$$

$$+ l_b^2 \Big[J'_{l_b}(a)\,(J'_{l_b}(a) + \frac{1}{a} J_{l_b}(a)) + J_{l_b}(a)\,J''_{l_b}(a) \Big] \Big(\frac{\omega_{cb}}{k_\parallel \Delta u_\parallel} Z(x_l^b) + \frac{1}{2l_b} \Big)$$

$$+ \frac{l_b}{2} (\frac{k_\parallel \Delta u_\parallel}{\omega_{cb}})^2 \Big[-\frac{2}{a} (\frac{u_\perp}{\Delta u_\parallel})^2 J_{l_b}(a) J'_{l_b}(a) + J'^{\,2}_{l_b}(a) + J_{l_b}(a) J''_{l_b}(a) \Big]$$

$$\cdot \Big((\frac{\omega_{cb}}{k_\parallel \Delta u_\parallel})^2 Z'(x_l^b) - \frac{1}{4l_b^2} \Big) \Big\}$$

$$\varepsilon_{13}^{\delta M} = (\frac{\omega_{pb}}{\omega})^2 \Big\{ l_b \frac{u_\parallel}{u_\perp} \Big[R'_1 + 2l_b\, J_{l_b}(a)\, J'_{l_b}(a) \Big(\frac{\omega_{cb}}{k_\parallel \Delta u_\parallel} Z(x_l^b) + \frac{1}{2l_b} \Big) \Big]$$

$$- l_b^2 \frac{\Delta u_\parallel}{u_\perp} \frac{k_\parallel \Delta u_\parallel}{\omega_{cb}} J_{l_b}(a)\, J'_{l_b}(a) \Big((\frac{\omega_{cb}}{k_\parallel \Delta u_\parallel})^2 Z'(x_l^b) - \frac{1}{4l_b^2} \Big)$$

$$- l_b \frac{k_\parallel}{k_\perp} \Big[\frac{R_1}{l_b} - 4 \frac{k_\parallel u_\parallel}{\omega_{cb}} \sum_{m=1,\neq l_b}^{\infty} \frac{m^2 J_m^2(a)}{(m^2-l_b^2)^2} - J_{l_b}^2(a) \Big(\frac{\omega_{cb}(\omega - l_b\omega_{cb})}{(k_\parallel \Delta u_\parallel)^2} Z'(x_l^b) - \frac{1}{2l_b} \Big) \Big] \Big\} \qquad (E2)$$

with the abbreviations

$$a = \frac{k_\perp u_\perp}{\omega_{cb}}; \qquad x_l^b = \frac{\omega - k_\parallel u_\parallel - l_b\omega_{cb}}{k_\parallel \Delta u_\parallel}; \qquad R_1 = 2 \sum_{m=1,\neq l_b}^{\infty} \frac{m^2}{m^2-l_b^2} J_m^2(a).$$

Notice, that the harmonic number, l_b, is defined by the condition: $l_b\omega_{cb} \approx l_i\omega_{ci} \approx \Re\mathrm{e}\{\omega\}$.

F. Examples of Beam Driven Modes

In this section of the appendix, the influence of the beam particle distribution on the plasma modes and the appearance of new modes only driven by the beam particles will be shortly discussed. The problem of beam driven ion cyclotron modes is rather complex due to the great number of parameters which enters in the dispersion relation. On the other hand, the complicate form of the dispersion relation with beam contribution included prohibits a simple classification of the modes as in the pure Maxwellian case (Appendix D). Thus, we restrict our discussion in this section to a few examples which show the typical

effects of beam driven instabilities depending on the model used for the beam particle distribution function. Further details are discussed in the main part of the report.

As pointed out in section D, the ion Bernstein mode is weekly damped for very small $k_{\|}$. Resonant beam contributions to the ε_{ij} tensor, especially to the ε_{11} element, will only occur if the following condition on the frequency holds: $\Re e\{\omega\} \approx l_b\omega_{cb} + k_{\|}u_{\|}$. Furthermore, the resonance condition for cyclotron modes of the Maxwellian part must be fulfilled: $\Re e\{\omega\} \approx l_i\omega_{ci}$. This leads to the combined condition for which beam driven instability may be expected:

$$\Re e\{\omega\} \approx l_b\omega_{cb} + k_{\|}u_{\|} \approx l_i\omega_{ci}. \qquad (F1)$$

In this report, we investigate only the case of neutral beam injection at the WVII-A stellarator, here, hydrogen was injected into a deuterium target plasma in allmost all cases. Consequently, we carried out the stability analysis for the harmonics of hydrogen modes which are related to the even harmonics of deuterium ($l_b = 2\,l_i$ in the formulas).

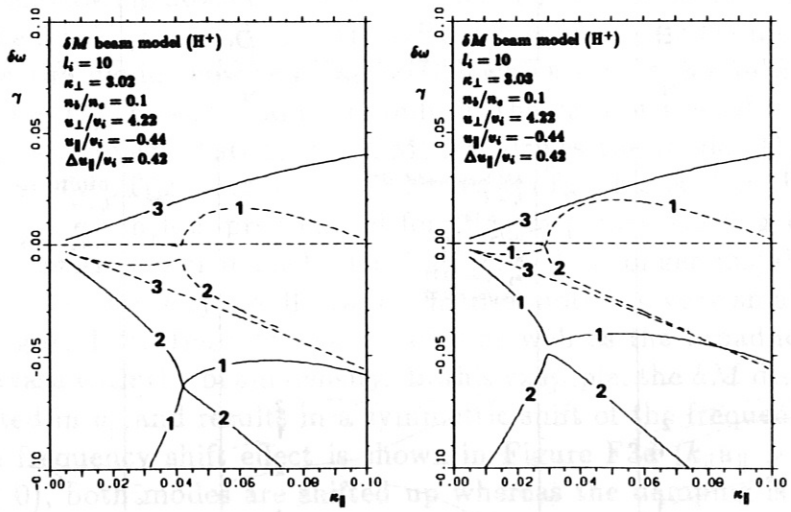

Fig. F1 *Beam driven ion cyclotron modes ($l_i = 10$): the frequency shift $\delta\omega$ (solid lines) and the damping γ (broken lines) versus $\kappa_{\|}$ (for the plasma parameter see Fig. D1). The normalized wave number $\kappa_{\perp}$ was change from 3.02 (on the left) to 3.03 (on the right). Note the great effect on the coupling of mode 1 and 2.*

In the first example (Fig. F1), mode coupling with respect to beam driven modes appears. The unstable mode (1) in Figure F1 couples for smaller $k_{\|}$ to a beam mode (2) which is stronger damped if $k_{\perp}$ is modified. Outside of this very narrow range in $k_{\perp}$, the frequency shift of mode (2) is nearly linear related to $k_{\|}$, the damping is the same as the damping of mode (3). These two modes (2 and 3) are beam driven modes and related to the roots of the plasma dispersion function in the $\varepsilon_{11}^{\delta M}$ element (see eq. E2) analogous to the strongly damped modes discussed in appendix D (eq. D3). The mode (1), however, is a ion Bernstein mode which is strongly modified by the beam contribution.

This effect of mode coupling (mode conversion) also appears for other cyclotron harmonics (see e.g. Fig. F3a and F3f) and depends very sensitively on $k_{||}$ and $k_{\perp}$ as well as on the parameters describing the beam particle distribution function. Furthermore, this example may demonstrate the importance of finding the roots of the dispersion relation accurately in the numerical calculations.

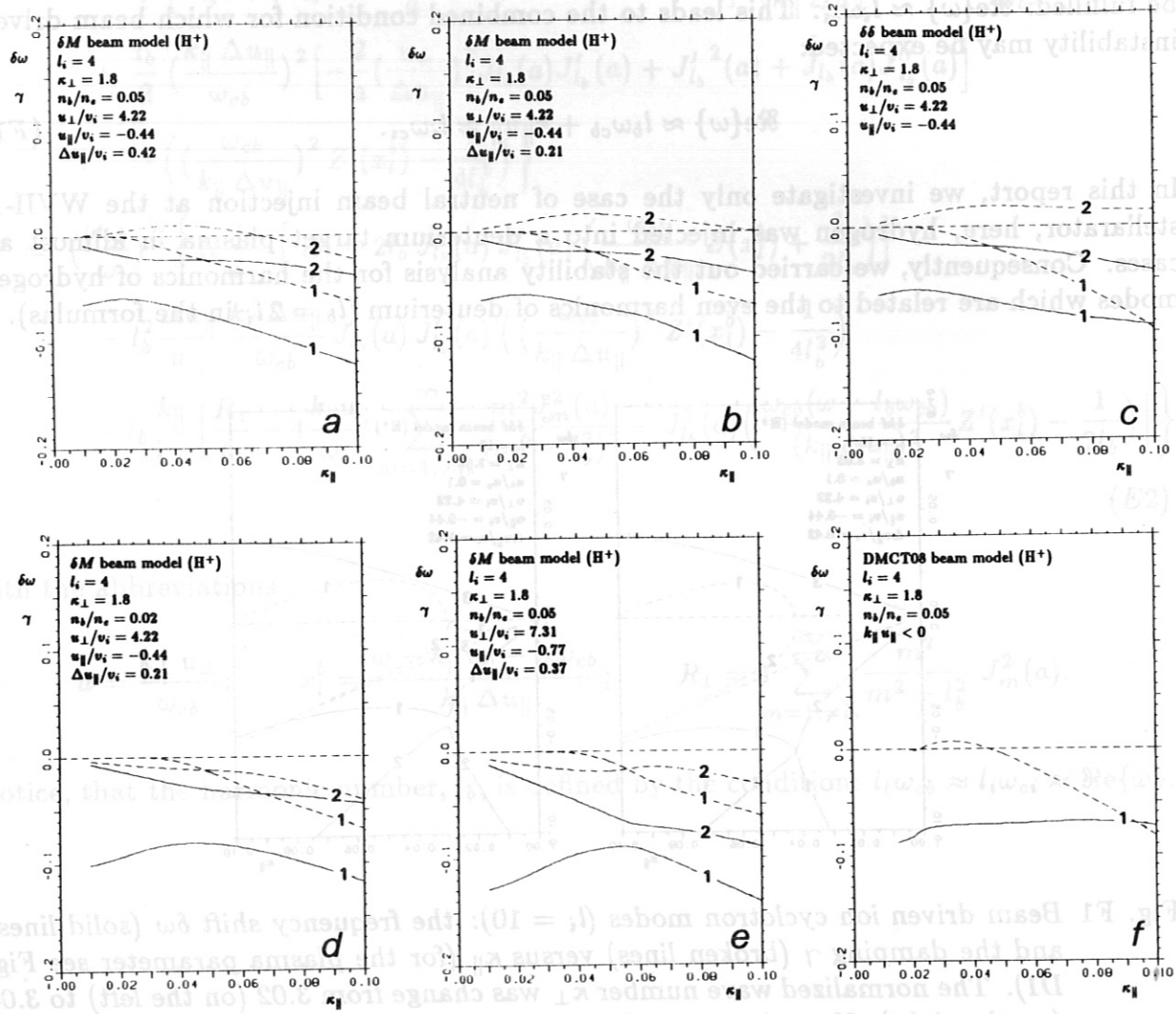

Fig. F2 *Beam driven ion cyclotron modes ($l_i = 4$): the frequency shift $\delta\omega$ (solid lines) and the damping γ (broken lines) versus $\kappa_{||}$ (for the plasma parameter see Fig. D1). A δ-Maxwellian distribution function (see eq. E1) was used to model the beam contribution (except the $\delta\delta$ function in F2c and the transient slowing down distribution* DMCT08 *in F2f). In the Figures F2a to F2c, the divergence in $v_{||}$, $\Delta u_{||}$, is reduced showing only small influence on the modes. The instability of mode (2) disappears for smaller beam density (F2d) and greater $u_{\perp}$ (F2e). In contrast to this, mode (2) disappears and the modified ion Bernstein mode (1) is unstable for the distribution function* DMCT08 *in Fig. F2f.*

In the next example, the influence of the beam particle distribution function, f_b, is investigated. The mode (1) in Figure F2 is the ion Bernstein mode of Figure D1 modified by the different beam contributions, the mode (2) is a beam driven mode and depends strongly on the form of the beam particle distribution function. As demonstrated by the Figures F2a to F2c, the parallel velocity divergence of f_b, $\Delta u_{||}$, has only small influence on the damping, the mode behaviour is nearly unaffected. The instability disappears with smaller beam density (Fig. F2d) as well as for higher injection energies (27 keV in Fig. F2e in comparison to 9 keV), $k_\perp$ is not resonant for this energy (see Appendix C). The transient slowing down distribution function DMCT08, however, drives the ion Bernstein mode unstable which is stable in the other cases. Furthermore, the beam mode (2) does not exist (Fig. F2f). This example demonstrates that the mode behaviour may significantly depend on the special model of the beam particle distribution function, especially on the shape in $v_\perp$.

The last example shows the mode behaviour near the $k_{||}$-resonance for a high harmonic ion cyclotron mode above the lower hybrid frequency ($l_i = 60$). Basis of the comparison of the modes in Figure F3 is the transient slowing down distribution function DMCT02 after a half of an average slowing down time (see Chapter III). The beam contribution, especially the vicinity of the 9 keV energy peak of the NBI, drives the mode (1) unstable. This mode is comparable to the mode shown in Figure D3, which was stable in a pure Maxwellian plasma. The mode (2), however, appears only in the case of the DMCT02 distribution. In Fig. F3b, the stationary distribution DMC327 drives the mode (1) unstable but less unstable than the DMCT02 distribution. The reason for this is that the environment of the 27 keV peak is much less pronounced for the stationary slowing down distribution functions for analogous beam particle densities. Much stronger instabilities appear for δ-functions in $v_\perp$ even for very small beam densities; note the very small beam density of $10^{10}\ cm^{-3}$ in Figure F3c. Here, the values of γ as well as the broadness of the instable region in $k_{||}$ increase with the beam density. In this example, the δM distribution function is nearly unshifted in $v_{||}$ and results in a symmetric shift of the frequency $\delta\omega$ near the $k_{||}$ resonance. The frequency shift effect is shown in Figure F3d ($k_{||}u_{||} > 0$) in comparison to F3a ($k_{||}u_{||} < 0$), both modes are shifted up whereas the damping is nearly unaffected (comp. the argument of the Z function in the $\varepsilon_{11}^{\delta M}$ tensor element of eq. (E2)). In Figure F3e is shown, that the broadness of the $k_{||}$ resonance and the maximum growth rate increase with the beam density, this effect is discussed in more detail in Chapter VI. The last example (Fig. F3f) shows mode coupling (mode conversion) between the two modes for a slightly increased value of $k_\perp$ in comparison to Fig. F3a. In all examples of Figure f3, the parallel group velocity of the modes (1) is strongly increased within the domain of instability; this behaviour is typical for the very strong instabilities above the lower hybrid frequency.

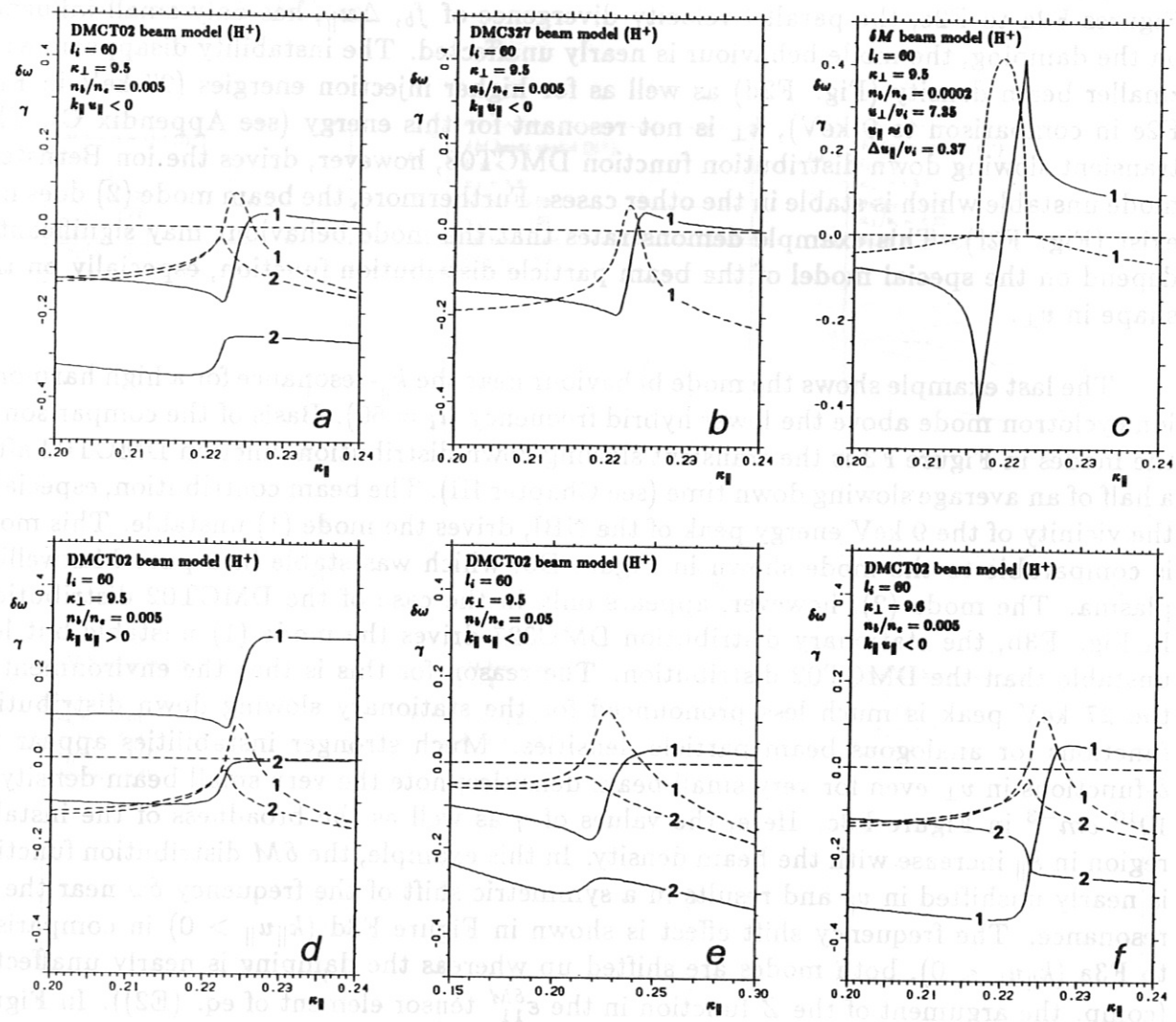

Fig. F3 *Beam driven ion cyclotron modes ($l_i = 60$): the frequency shift $\delta\omega$ (solid lines) and the damping γ (broken lines) versus $\kappa_\parallel$ (for the plasma parameter see Fig. D1). The strong instability in the $k_\parallel$ resonance and the frequency shift of ion cyclotron modes with frequencies above the lower hybrid frequency depend on the model of the beam distribution function. Three models are used in this Figure: the transient slowing down distribution function* DMCT02, *the stationary distribution* DMC327 *and a δ-Maxwellian distribution function. Note the different $\kappa_\parallel$-scale in plot* e.

G. Cauchy Rootfinder

Mathematical Formulation:

A Cauchy rootfinder was developed in order to find all roots of the complex function $D(\omega) = 0$ within a specified simply connected domain Ω of the complex ω-plane which is bounded by the closed path Ω_C. We make the following assumptions: (i) $D(\omega)$ is analytic in Ω, (ii) no poles of $D(\omega)$ exist in Ω ($D(\omega)$ is bounded in Ω). We calculate the following set of Cauchy integrals for the values $0 \leq \nu \leq n_1$ (with $n_1 \geq n = S_0$):

$$S_\nu = \frac{1}{2\pi i} \oint_{\Omega_C} \omega^\nu \cdot \frac{D'(\omega)}{D(\omega)} \, d\omega \,,$$

where D' is the derivative of D. Since we have only simple poles in the Cauchy integrand, the S_ν are given by the simple residues in the Ω domain:

$$S_\nu = \sum_{\mu=1}^{n} \left(\omega_\mu\right)^\nu ,$$

with the roots ω_μ of $D(\omega) = 0$ and with $n = S_0$ being the number of roots in Ω. The solution of this system of n non-linear equations for the n roots ω_μ may be reduced to the well-known problem of finding all roots of a complex polynomial of order n

$$\sum_{\nu=0}^{n} \alpha_\nu \omega^\nu = 0; \qquad (\alpha_n = 1)$$

by means of the following descending recurrence relation for the complex coefficients:

$$\alpha_\nu = -\frac{1}{n-\nu} \sum_{\mu=\nu+1}^{n} \alpha_\mu \cdot S_{\mu-\nu} \,.$$

With the solution of the polynomial problem, all roots of $D(\omega) = 0$ within the domain Ω are found.

Numerical Aspects:

Because of the numerical effort involved, the use of the Cauchy rootfinder should be restricted to cases with $D(\omega)$ not well-behaved in the neighbourhood of the domain Ω (e.g. functions involving the plasma dispersion function Z). Standard methods (e.g. the routine ZANLYT from the IMSL FORTRAN library) give rise to problems if the radius of convergence with respect to a root ω_ν is smaller than the domain Ω and the

methods (gradient methods in most cases) become strongly divergent in the neighbourhood of Ω. The Cauchy rootfinder is not dependent on the behaviour of $D(\omega)$ in Ω or in the neighbourhood; only the behaviour of the ratio $D'(\omega)/D(\omega)$ along the closed path Ω_C determines the numerical effort to find immediately all roots of $D(\omega) = 0$ in Ω.

In the Cauchy rootfinder routine COCAU, a rectangular path Ω_C with variable lengths parallel and perpendicular to the real ω-axis bounds the simply connected domain Ω for which the roots of $D(\omega)$ are calculated. These rectangular domains for the Cauchy integration have been found to be very usefull in connection with the stability analysis of plasma modes determined by the roots of the dielectric function. The Cauchy integral vector S_ν with dimension n_1 sufficiently large ($n_1 \leq 20$) is evaluated numerically by use of the extended Simpson's rule (Abramowitz, Stegun; eq. 25.4.5). The integrals parallel and perpendicular to the real axis are evaluated independently, the single number of internal bisections being automatically adjusted to the convergence of the single integrations. For the global convergence control, the 0th order moment S_0 is used:

$$|\Im\mathrm{m}\{S_0\}| \to 0 \quad \text{and} \quad |\Re\mathrm{e}\{\mathrm{S_0}\} - \mathrm{n}| \to 0.$$

If these convergence conditions are not fulfilled, the number of bisections is increased. If a root is very close to the integration path Ω_C, the Cauchy integration stops with an approximated value of this root. In this case, the Cauchy rootfinder routine is restarted with a new adjusted integration path Ω_C. Furthermore, if the number of the roots n is larger than the initial guess n_1, the routine COCAU may be restarted with respect to a smaller domain Ω or with an increased initial guess n_1.

For more than 3 roots of $D(\omega)$ in Ω, the polynomial coefficients α_ν are calculated by means of the recurrence relation using the moment vector S_μ, for $n \leq 2$ the roots are estimated directly. The roots ω_ν of the equivalent complex polynomial may be calculated using standard techniques (e.g. the routine C02ADF from NAG FORTRAN library). For a large number of roots or insufficient accuracy of the Cauchy integration (due to computing time problems because of the complexity of $D(\omega)$ and $D'(\omega)$), the accuracy of the roots found with the Cauchy formalism may be easily improved by gradient methods using the ω_ν of the Cauchy rootfinder as a start guess. No divergence problems will then appear.

Example: Roots of the Plasma Dispersion Function, Z

The simple use of the Cauchy rootfinder routine COCAU is demonstated with respect to the plasma dispersion function $Z(\omega)$ (see Ref. /22/), which is not well-behaved in the ω-plane for $\Im\mathrm{m}(\omega) < 0$. In this example, the Cauchy integration path Ω_C is quadratic with length $\delta_\omega = 4$, the lower left point is $\omega = 1.5 - 5\,i$. On the integration path between $\omega = 1.5 - 5\,i$ and $\omega = 5.5 - 5\,i$, the fast oscillating values of $Z(\omega)$ and of $Z'(\omega)$, respectively, change by more than 10 orders of magnitude. Consequently, convergence problems arise using rootfinders based on gradient methods. However, the ratio $Z'(\omega)/Z(\omega)$ is much more well-behaved on this part of Ω_C.

The 8 roots $Z(\omega) = 0$ in the rectangular domain Ω estimated by the Cauchy rootfinder routine C0CAU are improved using a simple gradient method routine (2nd order expansion). The relative accuracy of the plasma dispersion function routine used was better than 10^{-5}. All computations were carried out in single precision version.

C0CAU: roots of the plasma dispersion function $Z(\omega)$

number of roots $Z(\omega) = 0$ in Ω:	8
total number of function evaluations:	256
achieved accuracy $max\{\|\Re e(S_0 - n)\|, \|\Im m(S_0)\|\}$:	$6.3 \cdot 10^{-4}$

	C0CAU	improved accuracy
ω_1 :	$1.99147 - 1.35482 \cdot i$	$1.99147 - 1.35481 \cdot i$
ω_2 :	$2.69113 - 2.17703 \cdot i$	$2.69115 - 2.17704 \cdot i$
ω_3 :	$3.23555 - 2.78451 \cdot i$	$3.23533 - 2.78439 \cdot i$
ω_4 :	$3.69613 - 3.28665 \cdot i$	$3.69731 - 3.28741 \cdot i$
ω_5 :	$4.10747 - 3.72680 \cdot i$	$4.10611 - 3.72595 \cdot i$
ω_6 :	$4.47463 - 4.11830 \cdot i$	$4.47682 - 4.11963 \cdot i$
ω_7 :	$4.81953 - 4.48047 \cdot i$	$4.81849 - 4.47983 \cdot i$
ω_8 :	$5.13630 - 4.81334 \cdot i$	$5.13707 - 4.81381 \cdot i$

References

/ 1/ Cordey J.G. and M.J. Houghton; Nucl. Fusion, **13**, 215 (1973).

/ 2/ Mai L.P. and W. Horton, Jr.; Phys. Fluids, **19**, 1242 (1976).

/ 3/ TFR Group; Nucl. Fusion, **23**, 425 (1983).

/ 4/ Sbitnikova I.S. and A.V. Chudoleev; 3rd All-Union Conference on Hot Plasma Diagnostics, R.3.4.15, Dubna/USSR (1983).

/ 5/ W VII-A Team et al.; Plasma Phys. and Contr. Fusion, **26**, 183 (1984).

/ 6/ Maaßberg H. and M.A. Hellberg; Proceedings of the Int. Conf. on Plasma Phys., Lausanne 1984, Vol. 1, 55 (1984).

/ 7/ W VII-A Team and NI Group; Plasma Physics and Controlled Nuclear Fusion Research, (Proc. 10th Int. Conf. London 1984), Vol. 2, 371 (1984).

/ 8/ G. Grieger et al.; Plasma Phys. and Contr. Fusion, **28**, 43 (1986).

/ 9/ W VII-A Team and NI Group; 5th Int. Workshop on Stellarators, Schloß Ringberg 1984, Proc. IAEA Techn. Comm. Meet. on Plasma Conf. and Heating in Stellarators, EUR 9618 EN, Vol. 1, 219 (1984).

/10/ A. Weller and H. Maaßberg; Neutron Flux Measurements at the Wendelstein VII-A Stellarator, Report IPP 2/278, (1985).

/11/ Bhadra D.K., S.C. Chiu and R.W. Harvey; Nucl. Fusion, **22**, 763 (1982).

/12/ Mikhailovskij, A.B. and E.A. Pashitskij; Sov. Phys. - Tech. Phys., **10**, 1507 (1966).

/13/ Lee J.L. and C.K. Birdsall; Phys. Fluids, **22**, 1306 and 1315 (1979).

/14/ Bhadra D.K., S.C. Chiu, D. Buchenauer and D. Hwang; Nucl. Fusion, **26**, 201 (1986).

/15/ Berk L.H., W. Horton, Jr., M.N. Rosenbluth and P.H. Rutherford; Nucl. Fusion, **15**, 819 (1975).

/16/ Brecht S.H., D.A. Hitchcock and W. Horton, Jr.; Phys. Fluids, **21**, 447 (1978).

/17/ Maaßberg H.; Monte Carlo Simulation of Neutral Beam Injection in the Wendelstein VII-A Stellarator, Report IPP 2/281, (1986).

/18/ Callen J.D.; Absolute and Convective Microinstabilities of a Magnetized Plasma, Thesis, CSR T-68-3, (1968).

/19/ Akhiezer A.I., I.A. Akhiezer, R.V. Polovin, A.G. Sitenko and K.N. Stepanov; Collective Oscillations in a Plasma, Pergamon Press, Oxford, Vol. 7, (1967).

/20/ Penningfeld F.P., W. Ott and E. Speth; 12th Europ. Conf. on Contr. Fusion and Plasma Phys., Budapest 1985, ECA, Vol. 9F Part I, 397 (1985).

/21/ Hanson E.R.; A Table of Series and Products, Prendice-Hall, Inc., (1975).

/22/ Fried B.D. and S.D. Conte; The Plasma Dispersion Function, Academic Press, New York and London, (1961).

/23/ Rosenbluth M.N., W.M. MacDonald and D.L. Judd; Phys. Rev., **107**, 1 (1957).

Acknowledgements

The main part of this work was already performed in 1983 when one of the authors (M.A. Hellberg) was for about one year guest at the *Max-Planck Institut für Plasmaphysik* with financial support by the *Humboldt Stiftung*.

The experimental investigations referenced in this report were a common effort of the *W VII-A Team*. Particularly, we would like to thank Dr. H.J. Hartfuß (ECE electron temperature), Dr. J. Junker and Dr. M. Kick (CX neutral flux and ion temperature), Dr. G. Müller (ICE), Dr. W. Ohlendorf (CXRS ion temperature) and Dr. A. Weller (neutron flux) for placing the data at our disposal as well as for helpfull discussions. Furthermore, we are grateful to Dr. H. Renner and Dr. H. Wobig for stimulating this work.